Technische Universtät Dortmund
Fakultät für Chemie

Dissertation
zur Erlangung des akademischen Grades eines
Doktors der Naturwissenschaften

TIRF-anisotropy microscopy: homo-FRET and single molecule measurements

vorgelegt von
Márton Gelléri

September 2013

Erstgutachter:	Prof. Dr. Philippe Bastiaens
Zweitgutachter:	Prof. Dr. Roland Winter

Erklärung/Declaration

Die vorliegende Arbeit wurde in der Zeit von November 2008 bis September 2013 am Max-Planck-Institut für molekulare Physiologie in Dortmund unter der Anleitung von Prof. Dr. Philippe I. H. Bastiaens durchgefuhrt.

Hiermit versichere ich an Eides statt, dass ich die vorliegende Arbeit selbständig und nur mit den angegebenen Hilfsmitteln angefertigt habe.

The present work was accomplished from November 2008 to September 2013 at Max-Planck-Institute for molecular physiology in Dortmund under the guidance of Prof. Dr. Philippe I. H. Bastiaens.

I hereby declare that I performed the work presented independently and did not use any other but the indicated aids.

Dortmund, September 2013

Márton Gelléri

Abstract

Optical microscopy is limited by diffraction to a resolution of approximately half the wavelength of the light used. Recent fluorescence microscopy methods increase the optical resolution by localizing single molecules with a precision exceeding the diffraction limit. Sequential imaging of all fluorescent proteins in such an approach allows the reconstruction of a super-resolution image. The gain in resolution can be used to investigate the organization of proteins within cells on a sub-micrometer scale.

In this thesis, we combined localization microscopy with polarization measurements and total internal reflection fluorescence (TIRF) microscopy to investigate the spatial organization of plasma membrane proteins. The developed microscope was used in ensemble measurements to probe protein organization at a nanometer scale via Förster Resonance Energy Transfer (FRET) and to investigate molecular orientations on a single molecule level.

TIRF microscopy was combined with fluorescence anisotropy measurements to investigate the spatial organization of the small GTPase Ras and its active mutants. In ensemble measurements the presence of FRET leads to depolarization of the emitted fluorescence signal, and probing distances on the nanometer scale is possible. It was shown that anisotropy measurements with conventional wide field excitation as well as with TIRF excitation are hampered by high noise levels making it difficult to draw clear conclusions.

Anisotropy measurements were also carried out on a single molecule level. On a single molecule level polarization becomes a measure of the two-dimensional orientation of molecules. Stepwise bleaching experiments showed that polarization measurements allow the detection of homo-FRET on a single molecule level.

Photoactivated localization microscopy (PALM) was combined with orientation measurements. The effect of photoselection by the excitation light on a common PALM sample was investigated by rotating the polarization of the excitation light and measuring the distribution of molecular orientations. It was shown that the polarization of the excitation light can bias single molecule measurements. For a non-random distribution of the fluorophores this

bias can result in misleading conclusions.

Zusammenfassung

Lichtmikroskopie wird durch die Beugung von Licht auf eine Auflösung von etwa der halben Wellenlänge des Lichtes begrenzt. Neuere Methoden der Fluoreszenzmikroskopie umgehen diese Beugungsgrenze, indem die Position einzelner fluoreszierender Moleküle mit einer Genauigkeit bestimmt wird, die weit über der Auflösungsgrenze konventioneller Lichtmikroskopie liegt. Um diese Auflösung zu erreichen, wird eine Bildfolge von fluoreszierenden Molekülen aufgenommen, die zu einem hochauflösenden Mikroskopiebild rekonstruiert wird. Die erhöhte Auflösung kann dann benutzt werden um die räumliche Verteilung von Proteinen in Zellen auf einer Submikrometerskala zu untersuchen.

Um die räumliche Organisation von Plasmamembranproteinen zu untersuchen, wurden in der vorliegenden Arbeit Lokalisationsmikroskopie mit Polarisationsmessungen und interner Totalreflexionsmikroskopie (englisch: total internal reflection fluorescence microscopy, TIRF microscopy) kombiniert. Das entwickelte Mikroskop wurde sowohl in Ensemble-Messungen eingesetzt um die Proteinorganisation mittels Förster Resonanz Energietransfer (FRET) auf der Nanometerebene zu untersuchen, als auch in Einzelmolekülmessungen um molekulare Orientierungen zu betrachten.

TIRF Mikroskopie wurde mit Fluoreszenzanisotropiemessungen kombiniert um die räumliche Verteilung der kleinen GTPase Ras und ihren aktiven Mutanten zu untersuchen. In Ensemble-Messungen führt FRET zu einer Depolarisation des emittierten Fluoreszenzsignals, so dass Distanzen auf der Nanometerskala untersucht werden können. Es konnte gezeigt werden, dass Anisotropiemessungen sowohl in konventioneller Weitfeldanregung als auch in TIRF-Anregung durch den hohen Hintergrund beeinträchtigt und dadurch Rückschlüsse auf die Proteinorganisation erschwert werden.

Anisotropiemessungen wurden auch auf Einzelmolekülebene durchgeführt. Auf Einzelmolekülebene entspricht die Messung der Polarisation einer Messung der zweidimensionalen Orientierung der Moleküle. Stufenweises Bleichen von Molekülen zeigte, dass Polarisationsmessungen die Detektion von homo-FRET in Einzelmolekülmessungen erlauben.

Photoaktivierte Lokalisationsmikroskopie (PALM) wurde mit Polarisationsessungen kombiniert. Der Einfluss der Photoselektion wurde für eine typische Probe untersucht, indem die Polarisation des Anregungslichtes gedreht wurde und die Verteilung der Orientierungen der Moleküle bestimmt wurde. Es konnte gezeigt werden, dass die Polarisation des Anregungslichtes einen Einfluss auf Einzelmolekülmessungen hat. Für eine nichtzufällige Verteilung der Fluorophore kann dieser Einfluss zu falschen Rückschlüssen führen.

Hofstadter's Law:
It always takes longer than you expect, even when you take into account Hofstadter's Law

---

Douglas R. Hofstadter

Contents

1

Introduction

Multicellular systems form complex structures of highly differentiated cells. The cells drive a highly complex system of dynamic processes and communicate with their neighboring cells, even without direct contact. In both cases the information generated within the cells has to pass the cell membrane. The information can be an electrical or a metabolic signal, where the latter requires receptor molecules in the cell membrane. At the same time a single cell itself is a highly complex system. Driven by a dynamic network of interacting proteins it forms temporal and spatial patterns that are important for cell signaling.

The function of these receptors and proteins can be investigated by applying biochemical or physiological methods. However, to investigate their spatial organization, imaging techniques such as microscopy have to be applied. Microscopy enables the user to observe structures and processes in cells on a sub-micrometer scale. A commonly used technique in the biological sciences is fluorescence microscopy. In fluorescence microscopy, the molecules of interest are tagged with fluorescent markers. These markers emit light upon excitation and can be detected within the cell. However, any optical microscope is fundamentally limited by the diffraction of light to a resolution of roughly 200 nm laterally and 600 nm axially. Nevertheless, the specific tagging of proteins allows the detection and imaging on a single molecule level, making it possible to record the movement of single molecules

in living cells. A wide variety of available microscopy techniques allows for addressing specific biological problems, but at the same time makes it necessary to thoroughly think about the imaging methods and techniques used to determine the measurement parameters of interest.

Investigation of the nanoscale organization of plasma membrane proteins requires a microscope capable of probing distances well below the diffraction limit of light. This can be achieved using two different techniques: FRET microscopy, which uses the dipole-dipole coupling of two molecules in resonance to measure distances in the range of 5 to 10 nm, and single molecule localization microscopy, which accesses spatial scales of around 20 nm. These microscope techniques, being complementary on the length scale, are both fluorescence microscopy methods, thus allowing the specific tagging of the proteins of interest and the imaging of living cells. At the same time these two techniques are fundamentally different: whereas FRET measures the interaction of two molecules being close together, single molecule localization techniques image single molecules and determine their positions with a high accuracy. Single molecule methods require a sparsely fluorescent sample with only one molecule fluorescing in a diffraction limited region, whereas FRET measurements require at least two molecules being not further apart than 10 nm and are usually done in an ensemble measurement - multiple molecules are imaged at the same time residing in the same diffraction limited volume.

To investigate homo-dimerization and homo-oligomerization of proteins FRET can be used by measuring the fluorescence anisotropy of the sample. Fluorescence anisotropy is a measure of the depolarization of the emitted fluorescence. As the energy transfer between two molecules leads to a depolarization of the fluorescence signal, FRET leads to a depolarization of the emitted fluorescence and thus can be measured by fluorescence anisotropy.

These microscopy methods do not increase the axial resolution in fluorescence microscopy. The axial resolution can be increased by using total internal reflection fluorescence microscopy. In total internal reflection fluorescence microscopy the evanescent field of a totally reflected light beam is used to excite fluorescence. This is of special interest when investigating

plasma membrane proteins. These proteins reside in the plasma membrane of cells, a thin lipid bilayer of roughly 5 nanometers in thickness and are crucial for the signal transduction in cells.

This thesis aims to develop a microscopy method suitable for investigating the nanoscale organization of plasma membrane proteins, by combining total internal reflection fluorescence microscopy with fluorescence anisotropy microscopy in ensemble as well as single molecule measurements.

2

Theoretical background

This chapter provides the theoretical foundations for the experimental work presented in this thesis. The photophysics and photochemistry of fluorescence as well as microscopy, both being fundamental to this work, will be discussed briefly. A more in-depth review of the process of total internal reflection and evanescent waves as well as their application to microscopy will be given. The polarization properties of fluorescence light and the possibility to deduce molecular orientations from polarization microscopy data will be presented.

2.1 Photophysics of fluorescent probes

The theory and experiments presented in this thesis are based on fluorescence microscopy techniques. Since the first observations by Sir John Frederick William Herschel in 1845 [59], fluorescence techniques have evolved to a dominant imaging methodology in the biological sciences. Fluorescence is a form of luminescence, which is the emission of light by an atom or molecule in an excited state. The interaction of light with matter on a molecular level can be described by taking into account the electronic states of a molecule.

2.1.1 Fluorescence

Light emission by an atom or a molecule upon relaxation to an energetically lower state is called luminescence. This process is further divided into phosphorescence and fluorescence, which differ in the spin states of the excited electrons. According to the Pauli exclusion rule, the total wave function of two fermions has to be antisymmetric, meaning that two electrons in the same orbital must have different spins. The relaxation from an excited state in which the electron has the same spin as the ground-state electron (triplet state) is therefore spin-forbidden. This process takes place on relatively long time scales ranging from milliseconds up to a few hours and is called *phosphorescence*. Fluorescence on the other hand is a spin-allowed process, where the electron in the excited state has the opposite spin of the ground state electron. The relaxation takes place on a time scale in the order of nanoseconds.

In an atom or a molecule, the electronic transition usually takes place between the highest occupied molecular orbital (HOMO) and the lowest unoccupied molecular orbital (LUMO). Molecules, due to the fact that they are multi-atomic, have vibrational degrees of freedom which result in various vibrational states (see Figure 2.1). At ambient temperatures the separation energy between these vibrational states is large compared to the energy of the molecule and fluorescent molecules usually reside in their ground state. The molecule is excited by absorption of a photon, and an electron is promoted from the ground state to an excited state. This state can be any vibrational

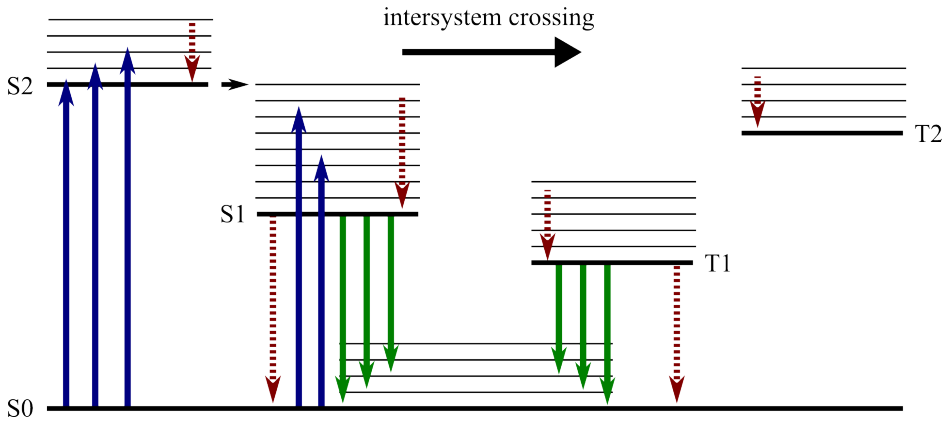

Figure 2.1: Schematic representation of fluorescence in a Jablonski diagram. Electrons residing in the singlet ground state S_0 can be excited to the excited singlet states S_1 and S_2. Intersystem crossing can lead to a triplet state. Excitation is represented by blue arrows, green arrows show radiative decay, dashed red arrows represent non-radiative decay.

state of the LUMO or the ground state of the LUMO. The strength of the transition between the HOMO and LUMO depends on the absorption dipole moment of the molecule [91]. A fast deactivation cascade then leads to a relaxation of the electron to the vibrational ground state of the LUMO, from where it relaxes by emitting a photon to the ground state or a higher vibrational state of the HOMO. This radiative relaxation is called fluorescence. The fluorescence lifetime, defined as the average time a molecule stays in its excited state, usually lies within a range of 1 to 10 ns.

It is important to note that the spin of an electron in an excited state can flip, due to spin-orbit coupling in molecules, which can result in a torque acting on the spin of the electron. The spin flip leads to a change of the spin of the molecule to $S = 1$. In an external magnetic field this spin has three possible orientations, hence the term *triplet state*. The process of spin flipping is called *intersystem crossing* and is a relatively rare event in commonly used fluorophores. However, the lifetime of a triplet state is extremely long compared to singlet state lifetimes as the transition to the ground state is spin forbidden. Experimentally, the triplet state can be observed on a single molecule level: A fluorescent molecule which is excited continuously over a short timespan will show fluctuations in its emitted intensity. In particular,

there will be dark periods of up to a few milliseconds where the molecule will not emit any light, a phenomenon called *blinking* [38, 24].

The ability of a molecule to fluoresce will vanish after a certain timespan by *photobleaching*. This process occurs most often due to chemical reactions with singlet oxygen. A fluorescent molecule in its triplet state can create singlet oxygen by triplet-triplet annihilation, which then interrupts the aromatic system of the fluorescent molecule.

2.1.2 Fluorescence anisotropy

A single fluorescent molecule can be regarded, in good approximation, as an oscillating dipole with an oriented absorption and emission transition dipole moment. Light is preferentially absorbed by a molecule if its absorption transition dipole moment is oriented along the electric field vector of the incident light, a process called *photoselection* [4]. For polarized excitation light the probability of exciting a molecule is maximal if its transition dipole moment is parallel to the excitation light polarization and vanishes for absorption transition dipole moments oriented perpendicular to the incident light polarization. Thus, in an ensemble measurement with randomly oriented molecules only a subset of molecules will be excited and each molecule will contribute to the total emitted intensity according to its absorption probability, which depends on its orientation relative to the electric field of the incident light. At the same time, the emission of a single molecule is polarized along its

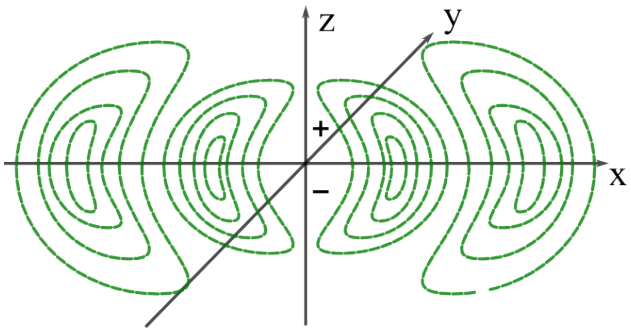

Figure 2.2: Schematic representation of the electric field of a radiating dipole. The dipole is oriented along the z-axis. The electric field is symmetric around the z-axis, but vanishes along the z-axis.

emission transition dipole moment. The intensity of the light emitted by the molecule decomposed in the polarization directions shows a cosine squared dependency on the angle between the emission transition dipole moment and the emitted electric field. The light is mostly polarized along the emission transition dipole moment and does not have any polarization components perpendicular to the transition dipole moment (Figure 2.2).

An ensemble of randomly oriented excited molecules will emit unpolarized light. However, if an ensemble of molecules is excited by polarized light, only a subset of these molecules will be excited due to photoselection. The light emitted by these fluorophores will be polarized, as the underlying distribution of excited molecules is non-random (Figure 2.3). The extent of polarization

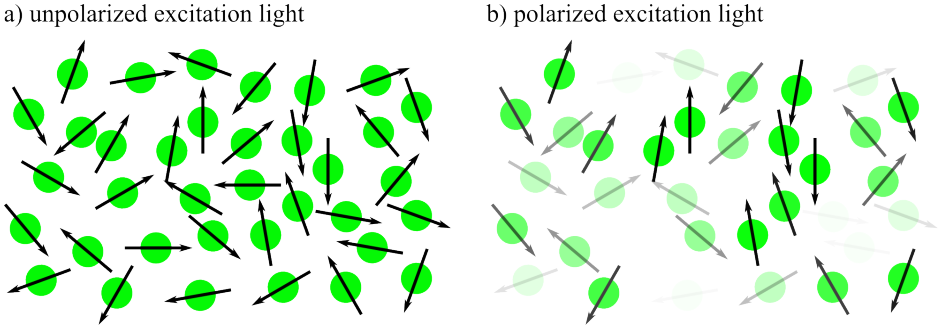

Figure 2.3: Schematic representation of photoselection using polarized excitation light. Randomly oriented fluorescent molecules are excited by (a) unpolarized light and (b) vertically polarized light. Absorption transition dipole moments of molecules are shown by arrows. The intensity of the green color represents the emitted intensity of the fluorescence of the molecules. For unpolarized excitation light the excitation probability is equal for all molecules. For vertically polarized light the excitation probability is maximal for molecules with transition dipole moments oriented parallel to the excitation polarization.

of the light emitted by such an ensemble of molecules is described by the fluorescence anisotropy [74]:

$$r^2 = \frac{(I_1 - I_2)^2 + (I_2 - I_3)^2 + (I_3 - I_1)^2}{2I^2}, \tag{2.1}$$

with I_1, I_2 and I_3 being relative intensities of the light components and $I = I_1 + I_2 + I_3$. The three electric field components are directed along

the three axes of the Cartesian system which is chosen such that $I_1 - I_3$ is maximal. Due to the axial symmetry this reduces with $I_2 = I_3$ to

$$r^2 = \left(\frac{I_1 - I_2}{I}\right)^2. \tag{2.2}$$

with $I = I_1 + 2I_2$.

Intensities I_1 and I_2 can experimentally be determined by placing a polarizer in front of the detector, and measuring the parallel ($I_{||}$) and perpendicular ($I_\perp$) components of the fluorescence emission (for a detailed description of such an experimental setup the reader is referred to section 2.2.4).

Sources of depolarization of the fluorescence signal

Fluorescence anisotropy is influenced by a number of processes that can lead to a depolarization of the light emitted by fluorophores. These processes can be intrinsic i.e. processes relying on the photophysical properties of the observed molecules or extrinsic, depending on the local environment (e.g. the rotational diffusion of the molecules or Förster resonance energy transfer (see Figure 2.5)). In anisotropy imaging optical components of the microscope can also lead to a depolarization of the fluorescence signal.

Intrinsic sources of depolarization

Intrinsic sources of depolarization that depend on photophysical processes like photoselection can be best understood by considering the fluorescence of a single molecule. Assuming, the excitation light is polarized along the x_3-axis and the dipole axis of the fluorescent molecule forms an angle Ψ with the x_3-axis and an angle Φ with the x_2-axis (see Figure 2.4), then the intensities I_1 and I_3 measured along the x_1 and x_3-axis are given by:

$$I_1 = \sin^2\Psi \sin^2\Phi, \tag{2.3}$$

$$I_3 = \cos^2\Psi. \tag{2.4}$$

However, in ensemble measurements multiple fluorophores contribute to

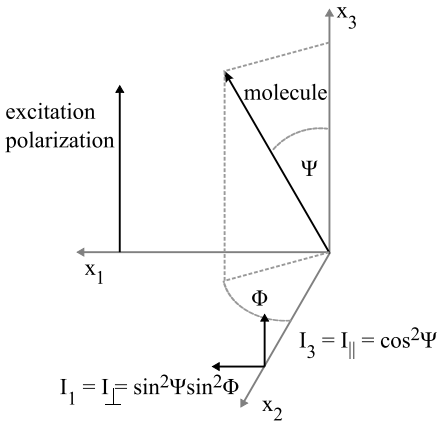

Figure 2.4: Schematic representation of an anisotropy measurement of a single molecule. The excitation polarization is parallel to the x_3-axis. Intensities are measured along the x_1- and x_3-axis by placing a polarizer before the detector oriented parallel and perpendicular with respect to the excitation beam. Note that $I_2 = I_3$.

the measured signal and the anisotropy will depend on the average orientation of the molecules. Therefore the average over the angles Ψ and Φ has to be calculated for randomly distributed fluorophores. This leads to:

$$r = \frac{3\left\langle \cos^2 \Psi \right\rangle - 1}{2}. \tag{2.5}$$

Therefore the anisotropy is limited only by the value of $\langle \cos^2 \Psi \rangle$ originating from the photoselection [74]:

$$\left\langle \cos^2 \Psi \right\rangle = \frac{\int_0^{\frac{\pi}{2}} \cos^2 \Psi f\left(\Psi\right) d\Psi}{\int_0^{\frac{\pi}{2}} f\left(\Psi\right) d\Psi}, \tag{2.6}$$

where $f\left(\Psi\right) = \cos^2 \Psi \sin^2 \Psi d\Psi$ is the photon absorption probability for a random distribution of molecules. This leads to a fundamental emission anisotropy for an ensemble of randomly distributed molecules of $r_0 = 0.4$.

Extrinsic sources of depolarization

So far we have discussed intrinsic sources of depolarization. These sources limit the fluorescence anisotropy fundamentally. Extrinsic factors can also

change the fluorescence signal, modifying the diffusion time, the fluorescence lifetime or the fluorescence polarization, thereby yielding information about the local environment of the fluorophore of interest.

One of the most important extrinsic sources of depolarization is the rotational diffusion of fluorophores. Molecules in a solution undergo Brownian motion, leading to translation and rotation of single fluorescent molecules. If

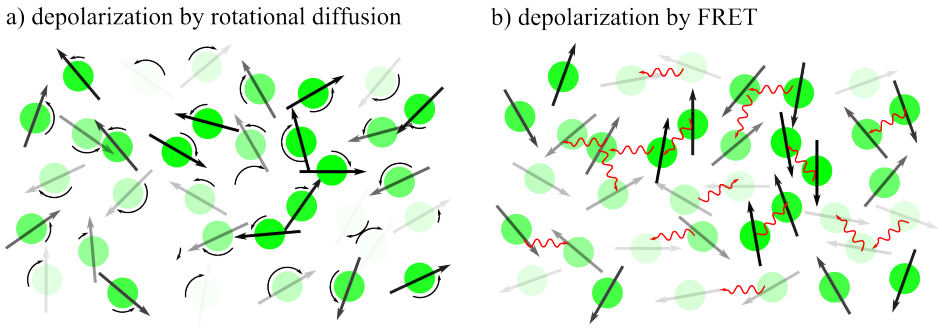

Figure 2.5: Schematic representation of depolarization by rotational diffusion and FRET. (a) Rotational diffusion leads to a depolarization of fluorescence light, if the fluorescent molecules are rotating within the time span of the fluorescence lifetime. (b) FRET between molecules leads to a depolarization of the emitted fluorescence.

a molecule rotates within the timespan of the fluorescence lifetime, the emission dipole moment can rotate significantly between absorbing and emitting a photon. A molecule with a transition dipole moment initially aligned with the polarization of the excitation beam is then no longer aligned with the excitation light when emitting light. In a measurement of an ensemble of molecules, this leads to a depolarization of the emitted light. The rotational correlation time τ_Θ of a molecule in a solution is defined as the time when the anisotropy has decayed to 1/e of its initial value [77]. The effect of rotational diffusion on the measured anisotropy is described by the Perrin equation [79]:

$$\frac{r_0}{r} = 1 + 6D_{\text{rot}}\tau = 1 + \frac{\tau}{\tau_\Theta}, \tag{2.7}$$

where r_0 is the fundamental emission anisotropy, D_{rot} the rotational diffusion coefficient and τ the fluorescence lifetime. In cases where the fluorescence lifetime is much shorter than the time scale on which rotational diffusion

takes place ($\tau << \tau_\Theta$) the fluorescence anisotropy is not altered by the rotational diffusion and the measured anisotropy is equal to the fundamental fluorescence anisotropy.

Another source of extrinsic depolarization of the fluorescence signal is Förster resonance energy transfer. In Förster resonance energy transfer energy is transferred from an excited donor fluorophore to an acceptor chromophore. If the acceptor chromophore is also a fluorophore the measured fluorescence will be depolarized if the emission dipoles of the donor and acceptor fluorophore are not parallel. Fluorescence energy transfer is discussed in more detail in section 2.1.3.

Optical sources of depolarization

In an objective type TIRF-setup high NA objectives are used to tilt the excitation beam such that the excitation light can undergo total internal reflection (see section 2.2.3). However, high NA lenses alter the polarization and thereby lead to an artificial decrease of the fluorescence anisotropy by mixing of the polarization components [96]. The emission fluorescence as well as the excitation beam are subject to this mixing [10]. The purity of the polarization state of each partial ray decreases with its distance from the optical axis, making rim beams less suitable for polarization measurements. However, these beams include information of molecule orientations along the optical axis and can be used to determine three-dimensional molecule orientations [61, 62]. High numerical aperture objectives lead to fluorescence anisotropy values that can be significantly lower than the actual value (see section 2.2.4).

2.1.3 Förster resonance energy transfer

Förster resonance energy transfer (FRET) is the non-radiative transfer of energy from a donor fluorophore to an acceptor molecule, another chromophore. Theodor Förster first proposed a comprehensive theory describing FRET [43, 44]. FRET is a dipole-dipole interaction, in which the donor and acceptor molecule have to be in resonance with each other, meaning that

the emission and absorption spectra of the donor molecule and the acceptor molecule have to overlap (Figure 2.6(a)). As a dipole-dipole interaction FRET varies inversely with the sixth power of the distance between donor and acceptor molecule. The rate k_T of energy transfer is given by:

$$k_T = \frac{1}{\tau_D}\left(\frac{R_0}{r}\right)^6. \tag{2.8}$$

τ_D is the fluorescence lifetime of the donor, R_0 is the *Förster radius* at which the transfer efficiency drops to 50% and r is the distance between donor and acceptor molecule. The distance dependency is also evident in the energy transfer efficiency E:

$$E = \frac{k_T(r)}{k_T(r) + k_D(r)} = \frac{R_0^6}{R_0^6 + r^6}, \tag{2.9}$$

which is defined as the transferred energy divided by the total energy absorbed by the donor. Figure 2.6(b) shows the transfer efficiency in dependence of the normalized distance. For commonly used fluorophores the Förster radius lies within 5 nm to 10 nm, well below the resolution limit of a light microscope.

FRET can be best understood by considering a single donor-acceptor pair. The donor and acceptor molecule are separated by the distance r, the donor quantum yield is given by Q_D and the extinction coefficient of the acceptor is $\epsilon(\lambda)$. Then the energy transfer rate can be written as [77]:

$$k_T(r) = \frac{Q_D\kappa^2}{\tau_D r^6}\left(\frac{9000\,(ln10)}{128\pi^5 N n^4}\right)\int_0^\infty F_D(\lambda)\,\epsilon_A(\lambda)\,\lambda^4 d\lambda, \tag{2.10}$$

where n is index of refraction of the medium and N is Avogadro's number. $F_D(\lambda)$ is the fluorescence intensity of the donor in a range λ to $\Delta\lambda$. The area under $F_D(\lambda)$ is normalized to unity. κ describes the relative orientation of the transition dipoles of the donor and acceptor molecule. The integral in equation (2.10) is called the overlap integral $J(\lambda)$. The overlap integral depends only on the total intensity of the transition dipole moments and does not include the orientation factor κ^2, which is present in the transfer

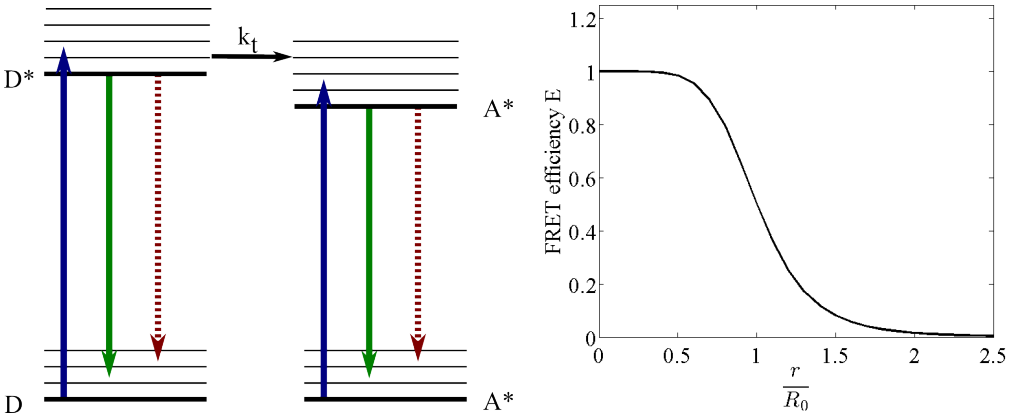

Figure 2.6: (a) Principle of Förster resonance energy transfer. The donor fluorophore in the excited state may relax to its ground state by emission of a photon. If an acceptor molecule is in close proximity the energy of the donor can be transferred to the acceptor molecule by a dipole-dipole interaction. For this to happen the donor and acceptor molecule have to be in resonance meaning the emission spectrum of the donor must overlap with the excitation spectrum of the acceptor molecule. (b) Energy transfer efficiency E as a function of $\frac{r}{R_0}$. At the Förster radius R_0 the efficiency drops to 50%

rate. κ^2 is given by:

$$\kappa^2 = \left(\sin\Theta_D \sin\Theta_A \cos\Phi - 2\cos\Theta_D \cos\Theta_A\right)^2 . \tag{2.11}$$

The angle Θ_D is the angle of the emission transition dipole of the donor molecule and Θ_A is the angle of the absorption transition dipole of the acceptor molecule with the vector joining these two molecules. Φ is the angle between the planes in which the transition dipole moments of donor and acceptor lie (see Figure 2.7).

For a random distribution of transition dipoles the orientation factor is $\kappa^2 = \frac{2}{3}$, where it is assumed that the distance between the two dipoles is large compared to the charge separation. For perpendicular transition dipole moments κ^2 vanishes and no energy is transferred; for parallel dipoles $\kappa^2 = 4$.

FRET can be detected by several imaging techniques as it directly influences the photophysics of fluorophores. The energy transfer from the excited

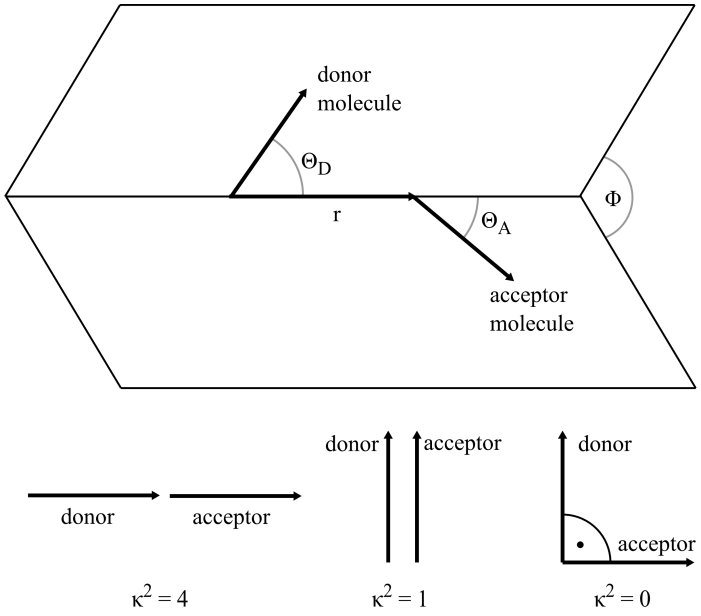

Figure 2.7: Schematic representation of the relative orientation of the donor and acceptor molecule. Donor and acceptor are separated by the distance r. The orientation factor κ^2 depends on the relative orientation of donor and acceptor molecule. κ^2 is maximal if the emission transition dipole of the donor molecule is parallel to the absorption dipole of the acceptor molecule and vanishes if they are oriented perpendicular.

state of the donor molecule to the excited state of the acceptor molecule leads to a decrease in the number of photons emitted by the donor. At the same time the acceptor molecule is excited and, in case the acceptor is another fluorophore, will fluoresce. FRET can therefore be detected by monitoring changes in the intensities of the donor and/or the acceptor by various methods [48].

As FRET influences the excited state lifetime, fluorescence lifetime measurements can also be used to detect FRET. Lifetime measurements are independent of the fluorophore concentration and are therefore often preferred over intensity based measurements. For an extended review of imaging techniques the reader is referred to [70]. In this thesis only anisotropy measurements will be reviewed in detail. FRET leads to a depolarization of the overall fluorescence, due to the relative orientation of the donor and acceptor molecule. The dipole-dipole interaction shows a cosine squared dependency

on the angle between acceptor and donor of the FRET-pair, thereby allowing a range of relative orientations for which FRET can occur. An acceptor molecule with an emission dipole moment which is not parallel to the emission dipole moment of the donor will lead to a depolarization of the fluorescence signal (Figure 2.5). Compared to other techniques, anisotropy measurements allow the detection of homo-FRET, the transfer of energy between identical fluorophores, providing a straightforward approach for measuring homo-dimerization and oligomerization of proteins [120, 18, 19, 17].

2.2 Microscopy

A microscope enables the user to observe objects and processes on submicrometer length scales. The first microscopes were built in the late 16^{th} and early 17^{th} century, and have been widely used in the biological sciences since then. Fluorescence microscopy is of major interest as it allows specific tagging of the molecules of interest. However, the limiting factor in microscopy is the optical resolution which restricts the size of resolvable objects to roughly 600 nm along the optical axis and 200 nm laterally [57].

2.2.1 Resolution limit

An object which is much smaller than the wavelength of light disturbs the wavefront of light incident on this particle. This object is, according to the Huygens-Fresnel principle, the source of a spherical wave. The intensity of this scattered wave is dependent on the size of the object. However, as long as the object is much smaller than the wavelength of light, the scattered wave will always be a spherical wave independent of the shape of the object. No information about the shape of the object is thus transported by the wave of light. Ernst Abbe first described when the shape of a microscopic object is resolvable [1] and thereby determined the *resolving power* of optical microscopes. In his work Abbe considered a grating imaged by a lens (Figure 2.8). The grating, illuminated by a light source, forms a diffraction pattern with a central intensity maximum of zeroth order, and higher order maxima next

to it. The angle of diffraction of these higher order maxima depends on the separation of the grating elements and becomes greater with smaller separation of the elements. To gain information about the distance of the grating

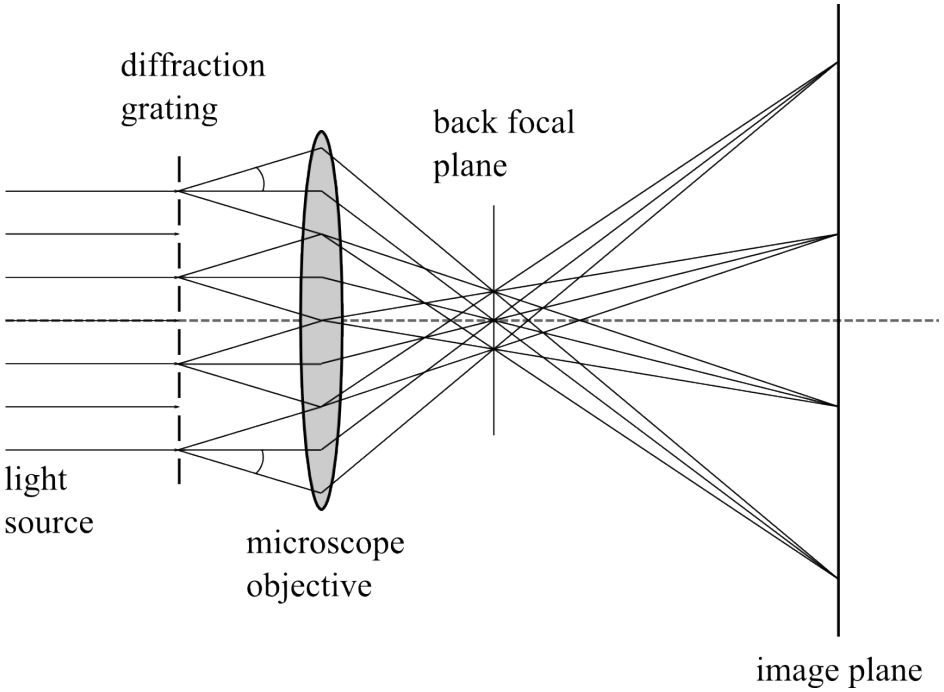

Figure 2.8: Abbe diffraction limit. A grating is imaged on screen by a microscope objective. Light incident on a grating will be diffracted and form a central maximum. A first order maximum will occur at an angle Θ, which depends on the distance of the grating elements d. To resolve the grating the microscope objective has to capture at least the first order maximum of the diffracted beam. The resolution of an optical microscope therefore depends on the range of angles which are accepted by the objective.

elements the lens must capture at least the first order maximum. Abbe found that the minimal distance $d_{\min}$ between the grating elements, such that they could be distinguished from one another, is

$$d_{\min} = \frac{\lambda}{2n \sin \Theta}, \tag{2.12}$$

the *resolution limit* according to Abbe. Herein, n is the index of refraction of the surrounding medium and Θ is the half-angle of the cone of light which can enter the lens. $\mathrm{NA} = n \sin \Theta$ is called *numerical aperture* and is a measure

for the range of angles of light that can be captured by a lens.

Shortly after Abbe, Lord Rayleigh described the interference patterns of two point sources of light separated by a distance d and imaged by a lens [84]. The light emitted by each point source will be diffracted by the aperture of the lens according to the Huygens-Fresnel principle, forming a diffraction pattern on a screen. The image of a single point source is forming a maximum of zeroth order at the center and concentric rings of higher orders around this central maximum: the *Airy diffraction pattern*. According to the Rayleigh-Criterion the two points can be distinguished if the zeroth order maximum of one light source just overlaps with the first minimum of the second point source. For any distance smaller than this the two point sources are not

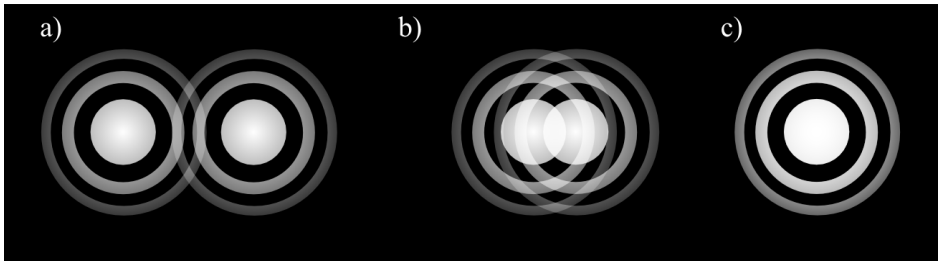

Figure 2.9: Rayleigh criterion. a) The diffraction patterns of two resolved point sources of light. b) If the maximum of zeroth order just overlaps with first minimum of the second diffraction pattern, the image is just resolved. c) If the diffraction patterns overlap completely, the image is not resolved.

resolved (Figure 2.9). The resolution limit given by the Rayleigh-limit is [26]:

$$d = 0.61 \cdot \frac{\lambda}{n \sin \Theta}. \tag{2.13}$$

It is worth noting, that λ is the emitted light wavelength and, unlike in Abbes description, not the illumination wavelength. The intensity distribution of a point source formed by a microscope in the image plane is called the *point spread function* (PSF). The image formation in a microscope can then be understood as a convolution of the PSF of the microscope with the object shape [71].

2.2.2 Localization based super-resolution techniques

The diffraction of light fundamentally limits the resolution in optical microscopy. In recent years several methods have been described to circumvent the lateral diffraction limit in microscopy. These techniques rely on the spatial patterning of the illumination light [50], the spatial patterning of the excitation light and the nonlinear response of fluorescent molecules [51, 114] or the temporal patterning of the emission of fluorophores upon a nonlinear switching behavior [23, 98, 60, 55, 35, 82]. The latter include also techniques known as *localization microscopy*.

Localization based microscopy techniques are capable of achieving optical resolution beyond the diffraction limit of light. These techniques rely on the sequential imaging of single molecules. Fluorescent molecules are switched between a non-fluorescent state and a fluorescent state. Instead of imaging all fluorescent molecules at once, a time series is recorded. In each image of the time series only a small subset of molecules is switched to the fluorescent state. Optimally each molecule is imaged once with no other molecule fluorescing at the same time in the same diffraction limited region. Thus, these techniques can be regarded as a time division multiplexed recording of an image: Multiple fluorescent molecules residing in the same diffraction limited spot emit fluorescence light at different time points and thus can be distinguished. However, compared to common time division multiplexing systems in telecommunication, multiplexing in localization microscopy is a stochastic process as the stochasticity of switching molecules from an non-fluorescent "off-state" to a fluorescent "on-state" is used to keep the density of fluorescent molecules low. Therefore localization based super-resolution microscopy techniques strongly depend on the photophysical and photochemical properties of fluorescent molecules and are often hampered by their non-ideal switching and blinking behavior [112, 7, 8, 27].

The image of a single molecule is the convolution of the object shape with the point spread function of the microscope. A single molecule imaged by an optical microscope can be regarded in good approximation as a point source of light as it is much smaller than the wavelength of the emitted fluorescence

light. The light emitted by this molecule will be diffracted by the microscope and form an Airy-diffraction pattern [26]. The diffraction pattern can be approximated by a two dimensional Gaussian distribution [121] with a width given by the point spread function of the microscope. The position of the centroid of the fluorescent molecule can be determined by fitting a Gaussian function to this intensity distribution. For a two dimensional Gaussian function centered at x_0, y_0 on a CCD camera the intensity I_r is given by:

$$I(r) = I_0 e^{-\left(\frac{(x-x_0)^2}{2s^2}+\frac{(y-y_0)^2}{2s^2}\right)}, \tag{2.14}$$

where I_0 is the amplitude and s is the standard deviation resulting from the point spread function. The standard error of determining the centroid is given by [109]:

$$\left\langle (\Delta x)^2 \right\rangle = \frac{s^2 + a^2/12}{N} + \frac{8\pi s^4 b^2}{a^2 N^2}, \tag{2.15}$$

where a is the size of a pixel measured in the sample plane, b is the background noise and N is the number of photons collected. The standard error is mainly limited by the number of photons collected. For a high enough number of photons $\left\langle (\Delta x)^2 \right\rangle$ can be approximated by $\left\langle (\Delta x)^2 \right\rangle \approx \frac{s^2}{\sqrt{N}}$. For $N = 500$, a wavelength of $\lambda = 590$ and an objective with $NA = 1.45$ this results in a standard error of $\left\langle (\Delta x)^2 \right\rangle \approx 4$nm, which is much smaller than the diffraction limit of light. Thus, the position of a single fluorescent molecule can be determined with a precision exceeding the optical resolution limit in microscopy by far.

Assuming two molecules which are separated by a distance smaller than the diffraction limit (Figure 2.10), one can see the benefits of sequentially localizing single point emitters. If the two molecules emit fluorescence light at the same time, the image will be the result of the convolution of the two points with the PSF of the microscope and it is not possible to resolve the two molecules. In a sequential imaging scheme only one molecule will fluoresce at a given time point and its position can be determined. The second molecule will be imaged at a later time point. As long as the distance between the two molecules is larger than the localization precision, the two molecules can

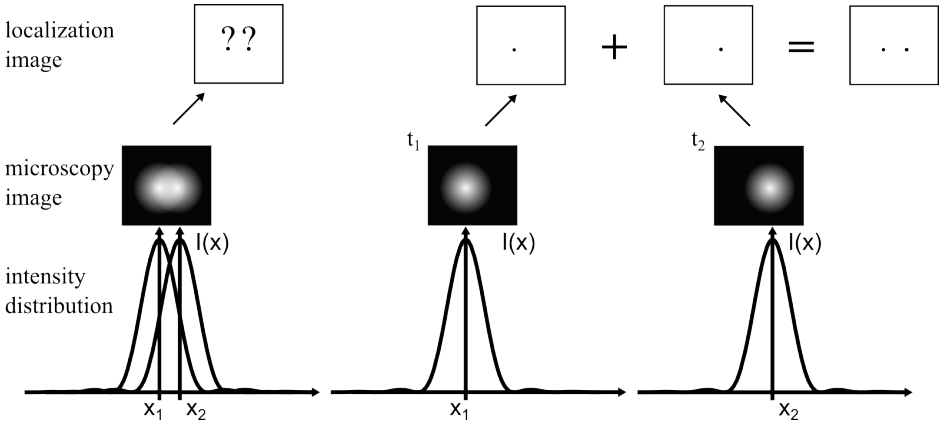

Figure 2.10: Localization of a single molecule by sequential imaging. Two fluorescent molecules and their intensity profiles. The two molecules are unresolved if the distance between their centers is less than the diffraction limit. If one of the molecules is imaged at a time point t_1 its position can be determined by localizing the center of its intensity profile. At a later time point t_2 only the second molecule emits fluorescence and can be localized. The localization precision exceeds the diffraction limit, thus a sum image of the positions will yield a super-resolution image.

be distinguished by their positions.

In a typical fluorescence microscopy measurement all fluorophores are in a fluorescent state. However, for localization microscopy based super-resolution techniques most of the fluorophores must be in a non-fluorescent dark state, such that the mean distance between two fluorescent molecules is greater than the diffraction limit of light [40]. If this holds true, the probability of finding two or more fluorescent molecules residing in the same diffraction limited region is small and single molecules can be imaged and localized. The imaging of a sparse subset of fluorescent molecules can be achieved by using photoactivatable fluorophores. These fluorophores are stochastically activated from an initially non-fluorescent state usually by illumination with light of a specific wavelength. Molecules in an active state show fluorescence upon excitation with light of a different spectral region. Sparse activation of the fluorophores allows for imaging of single fluorescent molecules. These molecules are then photobleached or deactivated by the readout light (Figure 2.11). To image a sufficient amount of molecules within the sample the mol-

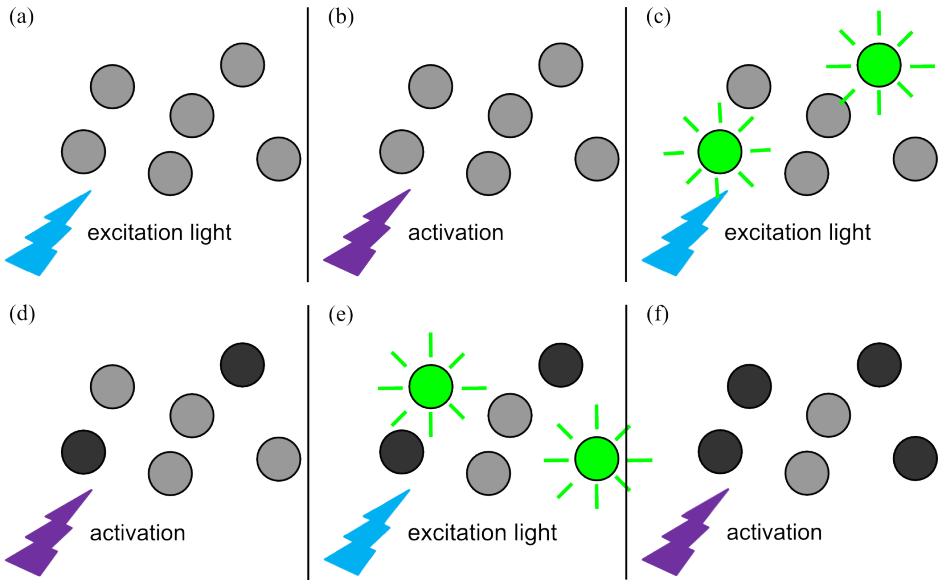

Figure 2.11: Principle of photo-activated localization microscopy. (a) Photoactivatable fluorescent molecules are in an non-fluorescent "off state". (b) Irradiation with light of a specific spectral range (in most cases UV-light) activates molecules. (c) Molecules now in an "on-state" will show fluorescence upon excitation. By activating only a small subset of molecules, the mean distance of fluorescent molecules will be much larger than the diffraction limit of light. (d) Molecules are imaged until they are bleached. A new subset of molecules is activated. (f) The cycle of activation and imaging is repeated until a sufficient number of molecules is localized.

ecules are usually continuously activated and read out at the same time. In a post-processing step the positions of the recorded single molecules are localized and an image of the molecule positions is reconstructed. The resolution of the reconstructed image is given by the localization accuracy of the single molecule positions as well as the density of the fluorophores. According to the Nyquist-Shannon sampling theorem [102] the distance between two neighboring molecules has to be at most half the distance of the desired resolution, otherwise structures on the length scale of the desired resolution will not be resolved [92]. For instance, to achieve 20 nm resolution, the structure has to be sampled at 10 nm in every direction.

2.2.3 Total internal reflection

So far we described methods to reduce the lateral resolution limit in optical microscopy. Localization based techniques can be extended to improve the resolution along the optical axis of the microscope [66, 65, 72, 103, 93]. However, these techniques require the use of additional optics in the emission pathway. In conventional wide-field setups the sample is excited outside the focal plane, thereby introducing background fluorescence to the measurement. The region which is excited can be reduced by using total internal reflection fluorescence microscopy [5]. In total internal reflection fluorescence microscopy the evanescent field of an electro-magnetic field is used to excite fluorescence. The word evanescent derives from the latin word "evanescere" which means vanishing. Therefore, in total internal reflection fluorescence microscopy (TIRF microscopy) "vanishing" waves of light are used to excite fluorescent molecules. Evanescent waves can be described by plane waves of the form:

$$\vec{E} = e^{i\left(\vec{k}\vec{r}-\omega t\right)}. \tag{2.16}$$

The main characteristic of an evanescent wave is the presence of at least one imaginary component of the wavevector $\vec{k}$. The wave along the direction of this imaginary component decays exponentially rather than propagating along this direction. Furthermore evanescent waves never occur in homogeneous media, their generation requires the interaction of light with inhomogeneities.

An evanescent wave is the result of light undergoing total internal reflection (Figure 2.12). Light being incident on an interface of two media with refractive indices n_1 and n_2 is partially reflected and refracted. Snell's law states:

$$n_1 \sin\left(\Theta_i\right) = n_2 \sin\left(\Theta_t\right), \tag{2.17}$$

where Θ_i and Θ_t are the angle of incidence and refraction, each measured from the normal of the interface. Light can be totally reflected if it propagates from an optically denser medium to an optically less dense medium, so that n_1 is greater than n_2. Light propagates tangential to the interface at an

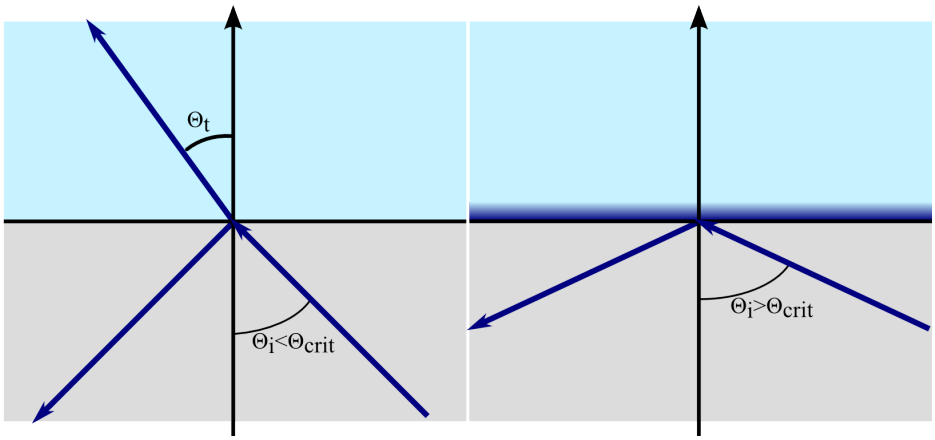

Figure 2.12: Light coming from a medium with an index of refraction n_1 and entering a medium with a refractive index n_2 with $n_2 > n_1$ undergoes total internal reflection if the incidence angle Θ is greater than the critical angle Θ_{crit}. At Θ_{crit} the angle of refraction is 90°, thus light is travelling parallel to the interface between the two media. For light undergoing total internal reflection an evanescent field is generated in the second medium. The evanescent wave vanishes exponentially with the distance from the interface where light is totally reflected.

incidence angle called the critical angle Θ_{crit} when Θ_t becomes 90°. The critical angle then can be derived from equation 2.17 and is given by:

$$\Theta_{\text{Crit}} = \arcsin \frac{n_2}{n_1}. \tag{2.18}$$

For any incidence angle Θ_i exceeding the critical angle no light will enter the optically less dense medium and but will be totally reflected. The net energy flow through the interface will vanish, however the electromagnetic field in the second medium will not disappear but decay exponentially in the direction normal to the interface. For light undergoing total internal reflection at an interface in the xy-plane and the plane of incidence in the xz-plane, the evanescent wave intensity is given by:

$$I(z) = I(0)\, e^{-z/d}, \tag{2.19}$$

where the penetration depth d is given by:

$$d = \frac{\lambda_0}{4\pi} \frac{1}{\sqrt{n_2^2 \sin^2 \Theta - n_1^2}}. \tag{2.20}$$

λ_0 is the wavelength of the incidence light [14].

In microscopy the evanescent wave is used to excite small regions just above the coverglass/sample interface. The penetration depth is greatly reduced due to the exponential decay of the evanescent wave. For green fluorescent protein excited at 476 nm and with a high NA-objective of 1.45 an incident angle of 72° is achievable. With an index of refraction of $n_{\text{coverglass}} = 1.52$ and $n_{\text{Water}} = 1.33$ the penetration depth is $d = 67$ nm. The plasma membrane of a cell has a thickness of roughly 5 nm [3] and is close to the coverglass (approximately 30 nm [73]). Fluorescently tagged proteins residing in the plasma membrane can thus be excited efficiently by an evanescent wave, whereas fluorescent background from cytosolic proteins is greatly reduced.

Experimentally TIR-illumination in fluorescence microscopy can be realized in several ways, the two most common schemes are through objective type illumination and prism-based illumination. In a prism-based setup a prism is used to couple light to the interface where total internal reflection takes place (Figure 2.13), fluorescence is then collected by microscope objective usually opposite to the prism. Prism type TIRF-setups offer better control over the incidence angle and thus over the penetration depth of the evanescent wave than objective type setups [101]. However, the sample accessibility is greatly reduced: The sample has to be kept between two coverslides allowing for excitation only in close proximity of the upper slide which is connected to the prism. The distance between the two cover glasses has to be reduced if an objective with a high numerical aperture and low working distance is used. Objective type TIRF setups use a high-NA objective which allows for angles of excitation above the critical angle. Light is focused to the back focal plane of the microscope objective. A translation of the beam in the back focal plane away from the lens center leads to tilting of the excitation beam, which can be used to achieve total internal reflection. For total internal reflection to occur on a glass/water interface with refractive

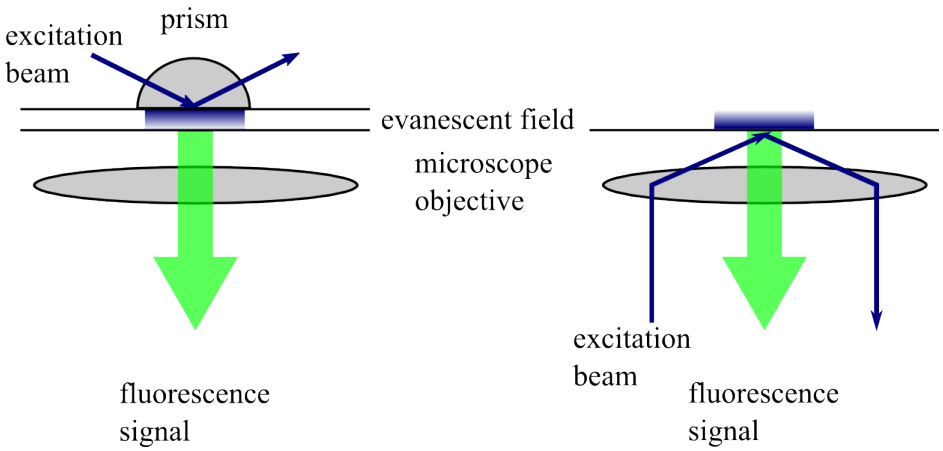

Figure 2.13: Experimental realization of TIR illumination in fluorescence microscopy. In a prism type TIRF setup (left) the light is coupled to the sample by a prism. The excitation beam undergoes total internal reflection at the coverglass. Light is collected by an objective which is positioned opposite to the prism. In an objective type TIRF setup (right), the excitation beam is focused off center to the back focal plane of a microscope objective. The objective tilts the excitation beam so it is incident on the cover glass with an angle exceeding the critical angle. Fluorescence light is collected by the same objective.

indices of $n_{\text{glass}} = 1.52$ and $n_{\text{Water}} = 1.33$ the critical angle is $\Theta_{\text{Crit}} = 61.0°$. For an immersion medium with a index of refraction of $n_{\text{immersion}} = 1.518$ this results in a minimal numerical aperture of $NA = 1.33$. TIRF-objectives must therefore have a numerical aperture which exceeds 1.33. Commercially available objectives have a numerical aperture ranging from 1.40 to 1.65. Objective based TIRF setups use the same objective for exciting the sample and collecting the fluorescence emission, thus no special considerations about the sample design and accessibility have to be taken into account.

2.2.4 Fluorescence anisotropy microscopy

So far we described methods to measure light intensity with high spatial resolution. As described in section 2.1.2 fluorescence anisotropy is a measure of the polarization of light emitted by an ensemble of fluorescent molecules, which can also be observed with a microscope. For the measurement of fluorescence anisotropy the sample is excited by polarized light and the light

intensities polarized parallel and perpendicular to the excitation light are measured. Fluorescence anisotropy is defined as:

$$r = \frac{I_{\parallel} - I_{\perp}}{I_{\text{total}}}, \tag{2.21}$$

where $I_{\parallel}$ is the intensity measured parallel to the excitation light and $I_{\perp}$ the light intensity perpendicular to the excitation light. The total intensity I_{total} is given by:

$$I_{\text{total}} = I_{\parallel} + 2I_{\perp}. \tag{2.22}$$

The normalization of equation (2.21) by the total intensity leads to a dimensionless value for the anisotropy r, which is independent of the fluorophore concentration. The factor 2 in the total intensity results from the three intensity components I_x, I_y and I_z along the axes x, y and z (see Figure 2.2) contributing equally to the total intensity. For a rotation symmetric emission of fluorescence around the z-axis I_x equals I_y with $I_y = I_{\perp}$ this leads to

$$I_{\text{total}} = I_x + I_y + I_z = I_{\parallel} + 2I_{\perp}. \tag{2.23}$$

Figure (2.14) shows a schematic diagram of an anisotropy setup with a conventional wide field microscope. The sample is excited by a light source with a fixed linear polarization. The intensities polarized parallel and perpendicular to the excitation light are split by a polarizing beam splitter. Each channel can then be imaged separately by a camera.

High numerical aperture objectives

In fluorescence anisotropy microscopy special care has to be taken when using high numerical aperture microscope objectives. High NA-objectives can alter the polarization of the excitation as well as the polarization of the emission light due to their large angle of acceptance [20, 69] and lead to measured fluorescence anisotropies which are significantly lower than the actual fluorescence anisotropy.

The description in this thesis is based on [9, 10], which does not incorpo-

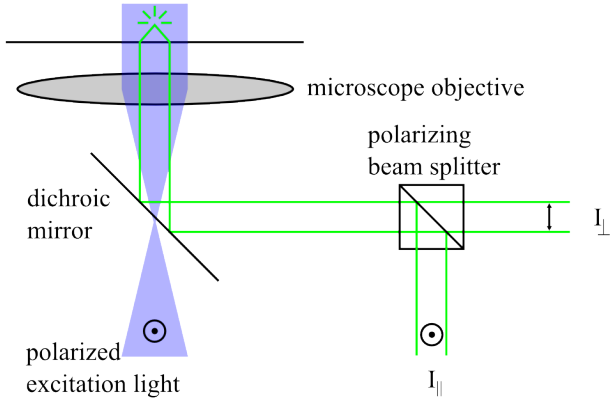

Figure 2.14: Schematic representation of a fluorescence anisotropy measurement with a wide field microscope. The sample is illuminated with linearly polarized excitation light (polarization points into the drawing plane). Fluorescence from the sample is separated from the excitation light by a dichroic mirror. The emitted light is then split by a polarizing beam splitter into light with polarization parallel ($I_{\parallel}$)and perpendicular ($I_{\perp}$) to the excitation light. An image of each channel is recorded.

rate any polarization effect on the excitation part as for widefield illumination the tipping and tilting of the polarization is negligible. In TIRF microscopy the s-polarized incident light will not be influenced by any high-NA-effect (see section 2.2.3) and thus the correction described in [9, 10] is also appropriate.

The influence of an objective with a high numerical aperture results from tipping and tilting of light by the objective. The total fluorescence collected by the objective is given by [9, 10]:

$$F_{\parallel} = k_a F_x + k_b F_y + k_c F_z, \tag{2.24}$$

$$F_{\perp} = k_a F_x + k_b F_y + k_c F_z, \tag{2.25}$$

where k_a, k_b, k_c are weighting factors accounting for the numerical aperture of the microscope objective. With Θ being the half angle of the cone of light

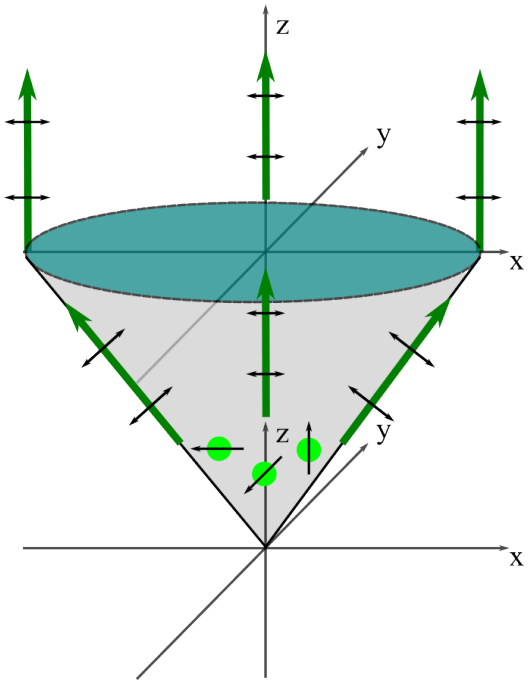

Figure 2.15: Detection of fluorescent molecules by a high-NA lens. The polarization is tilted by the lens such that light polarized along the z-axis will be detected. Molecules of all orientations will contribute to the fluorescence signal. This polarization mixing leads to a reduced anisotropy value.

accepted by the microscope objective k_a, k_b, k_c can be rewritten as:

$$k_a = \frac{1}{6} \cdot \frac{2 - 3\cos\Theta + \cos^3\Theta}{1 - \cos\Theta}, \tag{2.26}$$

$$k_b = \frac{1}{24} \cdot \frac{1 - 3\cos\Theta + 3\cos^2\Theta - \cos^3\Theta}{1 - \cos\Theta}, \tag{2.27}$$

$$k_c = \frac{1}{8} \cdot \frac{5 - 3\cos\Theta - \cos^2\Theta - \cos^3\Theta}{1 - \cos\Theta}. \tag{2.28}$$

The fluorescence anisotropy then can be calculated for a distribution of

randomly oriented molecules by using the corrected intensities:

$$F_y = \frac{k_b F_\parallel - k_c F_\perp}{k_a k_b + k_b^2 - k_a k_c - k_c^2}, \tag{2.29}$$

$$F_z = \frac{(k_a + k_b) F_\perp - (k_a + k_c) F_\parallel}{k_a k_b + k_b^2 - k_a k_c - k_c^2}. \tag{2.30}$$

2.2.5 TIRF anisotropy

The use of an evanescent wave in fluorescence anisotropy measurements reduces the signal from out-of-focus light greatly due to the reduced penetration depth of the evanescent field. In section 2.2.3, the generation of an evanescent wave has been described. To make use of an evanescent wave in fluorescence anisotropy microscopy the polarization of the evanescent field has to be taken into account. The electric field components of an evanescent wave at the interface were total internal reflection takes place ($z = 0$) are given by [13, 12]:

$$E_x = \frac{(2\cos\Theta)\left(\sin^2\Theta - n^2\right)^{\frac{1}{2}}}{\left(n^4\cos^2\Theta + \sin^2\Theta - n^2\right)} A_p e^{-\imath\left(\delta_p + \frac{\pi}{2}\right)}, \tag{2.31a}$$

$$E_y = \frac{2\cos\Theta}{\left(1 - n^2\right)^{\frac{1}{2}}} A_s e^{-\imath\delta_s}, \tag{2.31b}$$

$$E_z = \frac{2\cos\Theta\sin\Theta}{\left(n^4\cos^2\Theta + \sin^2\Theta - n^2\right)^{\frac{1}{2}}} A_p e^{-\imath\delta_p}, \tag{2.31c}$$

with

$$\delta_p \equiv \tan^{-1}\left[\frac{\left(\sin^2\Theta - n^2\right)^{\frac{1}{2}}}{n^2\cos\Theta}\right], \tag{2.32a}$$

$$\delta_s \equiv \tan^{-1}\left[\frac{\left(\sin^2\Theta - n^2\right)^{\frac{1}{2}}}{\cos\Theta}\right]. \tag{2.32b}$$

An incident beam with a polarization direction parallel to the plane of

incidence (p-polarization) and no polarization component perpendicular to the plane of incidence ($A_s = 0$) results in an evanescent wave with electric field components in x and z direction, with x being longitudinal. The phase shift of $\frac{\pi}{2}$ between the x- (equation (2.31a)) and z-component (equation (2.31c)) results in a whirling of the electric field around the z-axis (Figure 2.16). For an incidence beam with a polarization purely perpendicular to

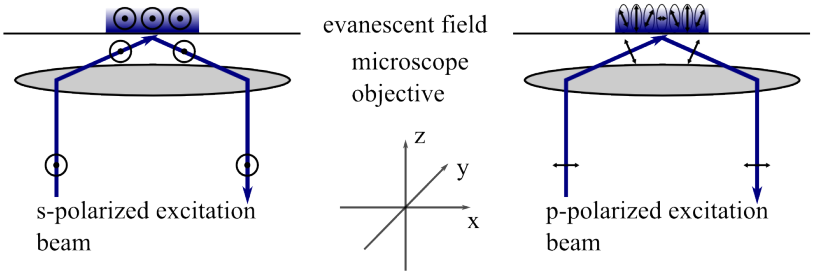

Figure 2.16: Polarization of the evanescent wave. A light beam undergoes total internal reflection. For a s-polarized incident light beam, the evanescent wave polarization is not altered and is polarized in the sample plane. A p-polarized incident beam results in an evanescent field with components in z- and x-directions. The phase difference of the x- and z-component (see Equation (2.31)) causes the evanescent field to whirl around the z-axis (adapted from [11]).

the incident plane (s-polarization) results in an evanescent electric field with a y-component and thus is polarized in this direction. It is important to note that the penetration depth d is independent of the polarization of the incident light, however, $I(0)$ does show a dependency on the polarization as well as on the angle of the incidence light [13, 11] (see Figure 2.17):

$$I_{\parallel}(0) = \left|A_{\parallel}\right|^2 \frac{(4\cos^2\Theta)\left(2\sin^2\Theta - n^2\right)}{n^4\cos^2\Theta + \sin^2\Theta - n^2}, \tag{2.33a}$$

$$I_{\perp}(0) = |A_{\perp}|^2 \frac{4\cos^2\Theta}{1-n^2}, \tag{2.33b}$$

where $\left|A_{\parallel}\right|^2$ and $|A_{\perp}|^2$ are the incident intensities and $n = \frac{n_1}{n_2}$.

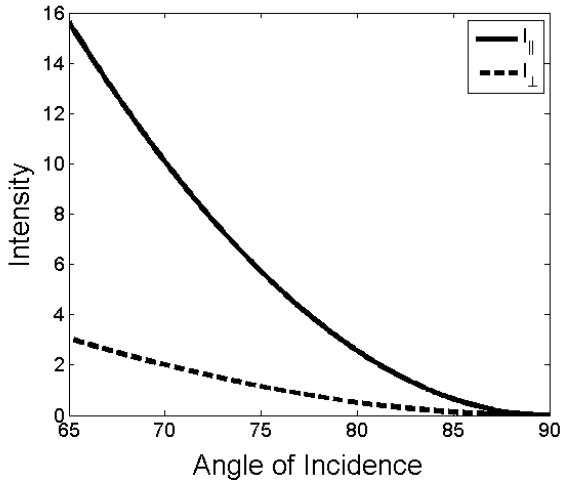

Figure 2.17: Intensities $I_{\parallel}(0)$ and $I_{\perp}(0)$ plotted for different incidence angles Θ_i beyond the critical angle $\Theta_{\text{crit}} = 61.5°$ with $n_1 = 1.33$ and $n_2 = 1.52$. $\left|A_{\parallel}\right|^2$ and $|A_{\perp}|^2$ are set to 1.

Due to its unique polarization states TIRF is well suited for anisotropy measurements. It allows for a purely transversal polarization in the sample plane as well as for a polarization state mainly along the optical axis of the microscope. Thus, probing any polarization state is possible without loosing the wide field capabilities. TIRF polarization measurements have been carried out as intensity measurements in dependence of the orientation of the polarization of the excitation light [9, 15].

2.3 Review of fluorescence anisotropy imaging literature

Despite the possibility of resolving clustering and dimerization by measuring homo-FRET [29], fluorescence anisotropy in combination with imaging has not been widely exploited yet. In particular fluorescence anisotropy measurements with TIRF microscopy have been seldomly used. Only recently fluorescence anisotropy in TIRF was used to investigate the homodimerization of Amyloid Precursor Protein [36]. Prior polarization measurements in TIRF

were mostly carried out as intensity measurements, probing the molecules of interest with the different polarization states of the exciting evanescent field [9, 15]. Further polarization measurements in TIRF were carried out to determine the organization of F-Actin [42] and the tilting and wobbling of Myosin V [22], however these measurements used a complex prism-type setup.

On a single molecule level orientation measurements are well known. Ha et al. presented orientation measurements by probing the absorption dipole moment of a single TexasRed molecule [52], polarization measurements were used to measure 2d molecule orientations [54] and in combination with spatial sampling of the Fourier components to measure 3d orientations [62, 45]. The defocused image of single molecules can also be used to determine 3d molecule orientations [25].

However, TIRF excitation was rarely used in single molecule orientation measurements. Orientation measurements in super resolution microscopy were mostly carried out by conventional wide field excitation measuring the polarization of the excitation light [46, 108].

Recently the polarization modulation in TIRF by rotating the excitation beam in the backfocal plane of the microscope objective was used to measure molecule orientations by probing the absorption dipole of single organic dye molecules [80].

3

Experimental realization of TIRF-anisotropy

This chapter describes the requirements for a TIRF anisotropy microscope, which is used for ensemble measurements as well as for single molecule measurements. The basic components of the microscope are discussed in detail. The central part, the microscope frame itself, is a commercially available inverted microscope. To implement polarized TIRF, the excitation and emission paths of the microscope are modified. In the next sections these modifications are discussed separately.

3.1 Excitation path

Figure 3.1 shows the experimental setup. As described in section 2.2.3, the evanescent electromagnetic wave in total internal reflection microscopy vanishes exponentially along the optical axis of the microscope, thereby allowing selective excitation of fluorescence close to the interface where total internal reflection takes place. Light undergoes total internal reflection if it is incident under an angle which is greater than the critical angle. The image quality in TIRF microscopy is thus greatly dependent on the angular distribution of partial rays exiting the objective: the beam has to be collimated by the objective to eliminate stray beams, which will not undergo total internal reflection [88]. This makes the use of lasers as a light source indispensable. Due to their high spatial coherence, light emitted by a laser can be focused to tiny spots as well as being collimated far better than light emitted by any other light source [99]. The setup described here uses an argon-ion laser (Innova Sabre DBW 20, Coherent, Santa Clara, USA) emitting at 476 nm, a krypton-ion laser (Innova Sabre DBW, Coherent, Santa Clara, USA) emitting at 568 nm and a diode-laser (iBeam-smart-405-s, Toptica Photonics, Gräfeling) at 406 nm, each coupled to a single mode fiber. Single mode fibers act as spatial filters, ensuring a perfect Gaussian beam profile by blocking high frequency components. The fiber transmitting the laser beam at 476 nm is equipped with a fiber polarization controller. The polarization controller makes use of the stress induced birefringence of glass and allows the generation of arbitrary polarization states of light. This is used to generate the desired polarization of the excitation light. The polarization state of this laser was aligned prior to any other laser and therefore full control over the polarization of this laser was needed for setting up the microscope. Both the fiber transmitting the laser line at 406 nm and the fiber transmitting the laser line at 568 nm are polarization maintaining fibers. They utilize rods included within their cladding, which are made from a different material than the cladding itself. These rods thereby induce stress within the fiber, which almost completely eliminates cross coupling between the two polarization modes of light in the fiber [99]. If the polarization of the light launched into the fiber is

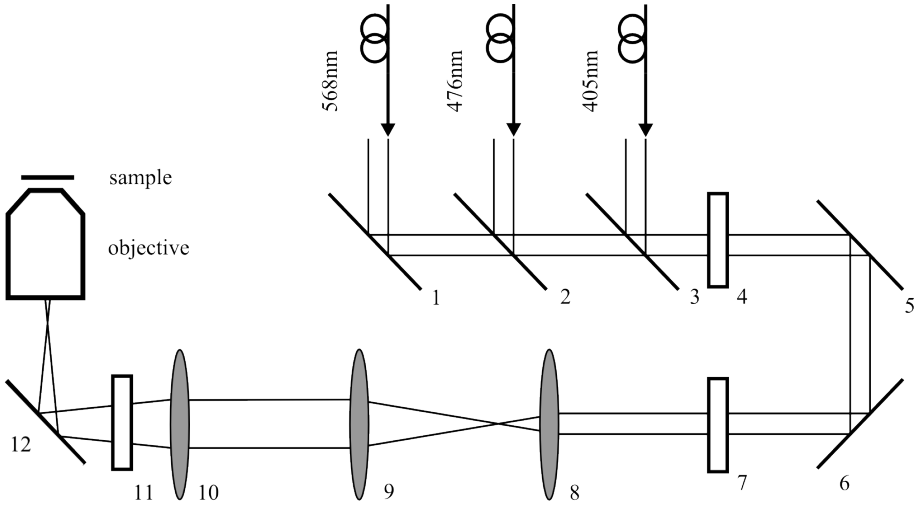

Figure 3.1: Setup used for polarized TIRF microscopy experiments, numbers are explained in Table 3.1

Table 3.1: Specifications of the optical elements used in the polarized TIRF setup in the excitation path.

	optical element	purpose
1, 5, 6	broadband dielectric mirrors	beam steering
2, 3	dichroic mirror	combining laser beams
4	polarizer	generates linear polarized light
7	achromatic half-wave plate	rotates linearly polarized light
8, 9	Keplerian type telescope	expands beam x10
10	lens mounted on a x,y,z translating mount	focuses light to the back focal plane of the microscope
11	polarizer	generates linearly polarized light
12	dichroic mirror	reflects laser light, transmits fluorescence light

aligned with the birefringence axis of the optical fiber, the polarization of the light will be maintained. The polarization of these lasers is aligned with polarization state of the laser emitting at 476 nm.

After exiting the fiber, each laser line is collimated to a beam diameter of approximately 2 mm. The three beams are then combined by two longpass dichroic mirrors (LaserMUX 375-405R, LaserMUX 473-491R, AHF, Tübingen, Germany) and pass a polarizer (DP-100-VIS, Meadowlark Optics,

Frederick, USA). This ensures that the three beams have the same polarization direction. A half-wave plate is then used to rotate the polarization. The beams are expanded by two achromatic lenses ($f_1 = 30$ mm, $f_2 = 250$ mm, Thorlabs, Newton, USA) to a beam with a waist of 20 mm. The beam is finally focused to the back focal plane of the microscope objective by another achromatic lens pair ($f = 250$ mm, Thorlabs, Newton, USA), mounted on a xyz-translation stage (PT3, Thorlabs, Newton, USA). By moving this lens in x and y the focal spot is translated in the back focal plane of the objective and TIR illumination is achieved. Moving the lens along the z-axis varies the focus position along the optical axis of the microscope. Another polarizer (DP-100-VIS, Meadowlark Optics, Frederick, USA) is placed next to the microscope body to generate purely linear polarized light and block any unwanted polarization component introduced by optical elements before this polarizer.

The light enters the microscope body via the fluorescence turret from the right side. A dichroic mirror (Z 405/473/561, AHF, Tübingen) rotated by 90° reflects the light to the objective, a 1.45 NA, 60×, oil immersion objective (PLAPON 60XOTIRFM, Olympus, Tokyo, Japan). This objective has been used for all the measurements presented in this thesis. The use of an objective based TIRF illumination is preferred over a prism based illumination as the sample is more easily accessible with the high-NA objective. A high-NA objective is needed for single molecule measurements to increase the signal-to-noise ratios compared to low-NA objectives [34].

3.2 Emission path

The emission path is shown in Figure 3.2. The objective used for the excitation of the sample also collects the fluorescence light. The emission and excitation light are separated by a dichroic mirror (Z 405/473/561, AHF, Tübingen), which reflects the excitation light and transmits the fluorescence light. An additional notch filter (Z 405/473/561, AHF, Tübingen) is placed in the emission path to block laser light that leaks through the dichroic mirror. After passing this notch filter, a tube lens forms the actual microscope

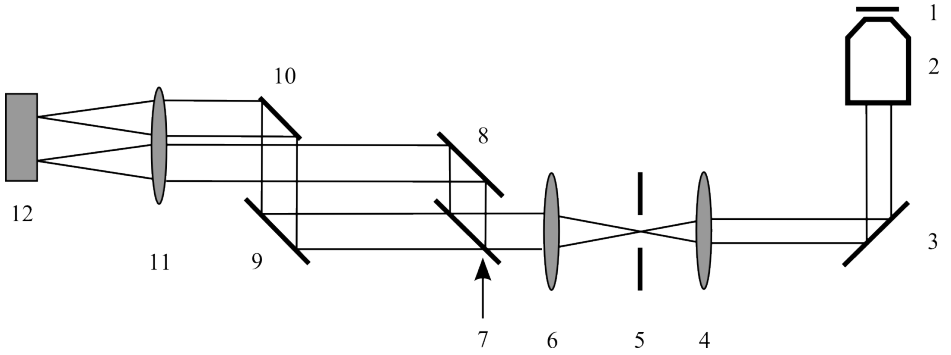

Figure 3.2: Emission path of setup used for polarized TIRF microscopy experiments, numbers are explained in Table 3.2.

Table 3.2: Specifications of the optical elements used in the polarized TIRF in the emission path setup.

	optical element	purpose
1	sample plane	sample is placed here
2	microscope objective	objective used for imaging and excitation
3, 8, 9	mirror	beam steering
4	microscope tube lens	generates real image in the aperture plane
5	adjustable aperture	reduces the image size to half the camera size
7	polarizing beam splitter	separates parallel and perpendicular polarization components
10	square mirror	reflects beam transmitted by the polarizing beam splitter
6, 11	Keplerian type telescope	magnifies the image by a factor of 2
12	EM-CCD camera	camera used for imaging

image. An adjustable slit (VA100/M, Thorlabs, Newton, USA), positioned in this image plane, reduces the image size so that the image, after a further magnification, occupies half the size of the CCD-camera. Two achromatic lens pairs (Thorlabs, Newton, USA) are introduced into the beam path to magnify the image by a factor of 2. The distance between the first lens (f = 200 mm) and the microscope image plane is 200 mm, such that the

image lies in the focal plane of the lens. Thus, the lens forms a conjugate plane of the microscopes aperture plane in its focus. The focal plane of the second lens ($f = 400$ mm) coincides with the focal plane of the first lens, so that the microscope image is formed again in its back focal plane. The magnification of the image is given by the ratio of the focal lengths of the two lenses. To split the light emitted by the sample in a parallel and perpendicular channel for anisotropy measurements, a polarizing beam splitter is placed in the conjugate plane of the aperture plane of the microscope, transmitting the parallel polarized light while reflecting the perpendicular polarized light. The light is then guided to the tube lens by additional mirrors. To reduce spherical aberrations by the last lens, it is important to hit the lens close to the center at an angle close to 0 degrees with both channels being symmetric around the lens center. Therefore, the spatial separation of the two channels should be minimized, which is achieved by a square mirror. This mirror is used as a pick-off mirror, the reflected beam hitting the mirror close to the edge and thereby enabling a very small separation between the transmitted and reflected beam.

3.2.1 Modifications to the setup in super-resolution microscopy

In photo-activated localization microscopy fluorescent proteins are used which are photo-activatable or photo-switchable. These fluorescent proteins have an *off-state* in which they do not emit fluorescence upon excitation. They can be switched to a fluorescent *on-state* by irradiating them with light of a certain wavelength. Upon excitation with light of a different wavelength they will fluoresce. Thus the microscope has to be optimized for the use of at least two different wavelength of light. Activation respectively switching is done by using a diode laser at 405 nm. Fluorophores are excited at 568 nm. Therefore, the polarization state of both lasers has to be controlled, making some modifications to the setup necessary. The zero order half-wave plate at 476 nm (4 in Figure 3.1) is replaced by an achromatic half-wave plate (AHWP05M-600, Thorlabs, USA) which shows a spectrally flat retardance

compared to zero order waveplates (Figure 3.3). However, due to variations

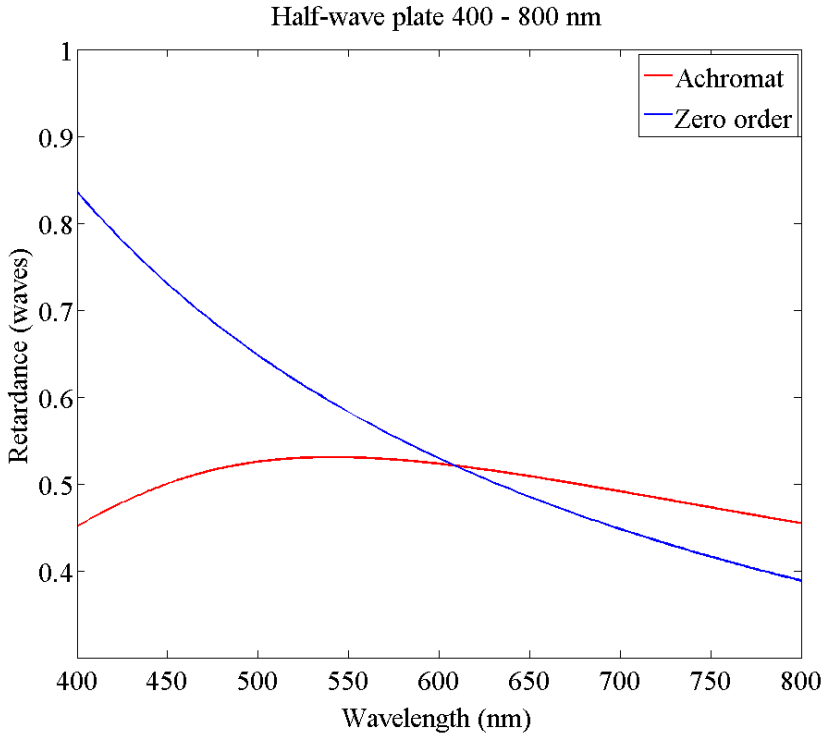

Figure 3.3: Retardance of the achromatic half-wave plate (AHWP05M-600, Thorlabs) compared to a zero order half-wave plate.

in the retardance over the spectral region of interest a polarizer is placed to the setup just next to the lens focusing the light to the back focal plane of the microscope. This polarizer ensures a purely linear polarization of the excitation beam. By rotation of the half wave plate and the polarizer s- or p-polarized light can be generated.

3.3 Measurement of the G-factor

Almost all components of the microscope show a dependency on the polarization of light. This results from antireflective or highly reflective dielectric coatings on optical elements. These coatings use the constructive and destructive interference of light reflected by multiple thin layers of dielectrics

with varying index of refraction. Optical elements with such an anti- or high-reflective coating usually show only small effects on the polarization of light when hit by a ray of light at normal incidence. However, any component hit by light rays incident other than normal to the surface of the optical components will show a polarization dependency. This polarization dependency is usually seen as a dependency of reflection and transmission on the polarization of the incidence light, resulting in different sensitivities in the detection of light for the parallel and perpendicular channels of the microscope. Thus, in any anisotropy measurement these differences have to be corrected for. Correction is done by introducing the *G-factor* into the measurement of fluorescence anisotropy. The G-factor is a multiplicative factor which normalizes the sensitivities of the parallel and perpendicular channel. The G-factor can be determined by measuring a polarized sample and rotating the excitation polarization by 90°. The parallel channel becomes the perpendicular channel by rotation of the excitation polarization. In an ideal case the intensities measured in both channels are the same. Since there are differences in the transmission and reflection of the optical components due to the different polarization states of light, the intensities in the two channels will differ. The G-factor is therefore the ratio of the intensities of the two channels. However, in microscopy systems one has to account for differences in the illumination pathway and bleedthrough between the two channels. This can be corrected for by modifying the calculation of the G-factor [86].

Another possibility to measure the G-factor is to measure the intensities of a sample which emits unpolarized light. Intensities in the parallel and perpendicular channel are then the same and measured intensities differ only due to different detection sensitivities of the channels. The G-factor is given by the ratio of the measured intensities in the two channels.

Whereas the first method depends on changes in the excitation path, the latter is only dependent on the differences in the emission path. In this thesis, the measurement of the G-factor is carried out by measuring fluorescein in an aqueous solution which has an anisotropy value close to zero [78, 18]. This method is preferred over the rotation of the excitation light polarization as the illumination is not altered and errors introduced by

non optimal alignment of the excitation polarization or the TIRF-angle are avoided.

Figure 3.4 shows a drop of fluorescein dissolved in water imaged in conventional widefield (3.4(a)) and in TIRF microscopy (3.4(b)). The G-factor G can be calculated by subtracting the camera background and dividing the signal from the parallel channel $G_{||}$ by the signal from the perpendicular channel $G_{\perp}$. The fluorescence anisotropy is then given by:

$$r = \frac{I_{||} - GI_{\perp}}{I_{||} + 2GI_{\perp}} \tag{3.1}$$

Measured G-factor values for different objectives are shown in table 3.3.

Figure 3.4 shows clearly visible interference fringes in TIRF illumination that are not visible in conventional wide filed illumination. The interference fringes result from scattered and diffracted light beams and are commonly known to deteriorate images in TIRF microscopy [76, 87, 41]. To reduce the influence of varying intensities throughout the field of view due to inhomogeneous illumination, the anisotropy image is divided by the G-factor image. This corresponds to a pixelwise calculation of the G-factor and results in a normalization of the intensity, eliminating inhomogeneities in the sample illumination and is therefore preferred over the calculation of an average G-factor value. With $G = \frac{G_{||}}{G_{\perp}}$ equation (3.1) then becomes:

$$r = \frac{\frac{I_{||}}{G_{||}} - \frac{I_{\perp}}{G_{\perp}}}{\frac{I_{||}}{G_{||}} + 2\frac{I_{\perp}}{G_{\perp}}} \tag{3.2}$$

3.4 EM-CCD

The key to single molecule imaging is the sensitivity of the detector. A photo-activatable fluorescent protein emits a few hundred photons [107, 111], an organic dye emits approximately 5000 photons on average before photobleaching [21, 111]. In section 2.2.2 it was shown that the localization precision depends on the signal to noise ratio and thus on the number of photons

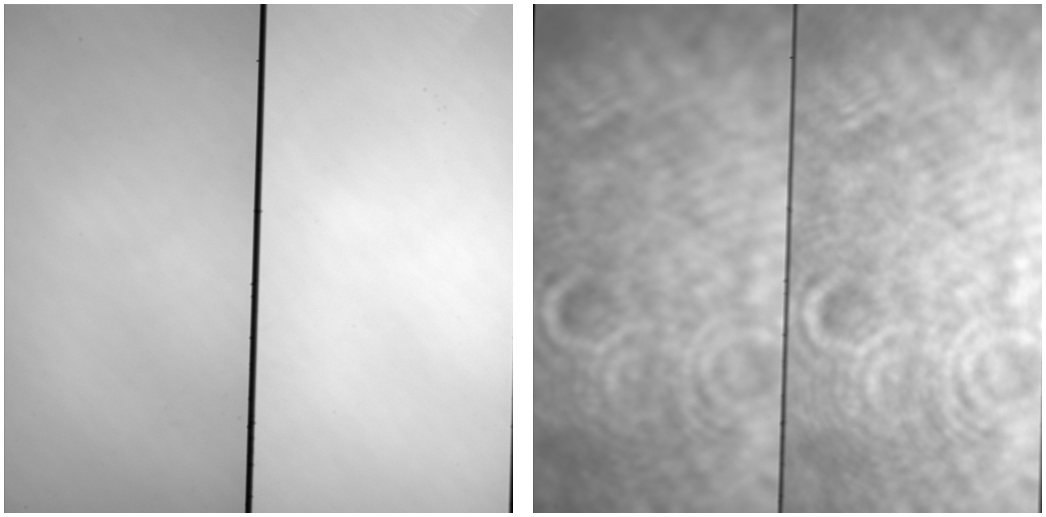

(a) G-factor image recorded in wide field (b) G-factor image recorded in TIRF

Figure 3.4: Measurement of the G-factor with a 60x objective. A drop of fluorescein is dissolved in water and excited with 476 nm. The emitted fluorescence is imaged with (a) conventional widefield and in (b) TIRF excitation. The left image half shows the perpendicular channel the right image half shows the parallel channel.

detected by the camera. As the number of emitted photons is rather low, the sensitivity of the detector is crucial.

Localization microscopy approaches are essentially wide field microscopy methods, where the full field of view is recorded during one exposure. Therefore, highly sensitive point detectors like avalanche photodiodes or photomultiplier are not suited for these techniques.

Electron-multiplying charge-coupled device (EM-CCD) cameras are commonly used in low light applications and are the most widely used cameras in wide-field single molecule imaging [89]. Only recently the development of scientific CMOS chips provided an alternative to EM-CCD chips in terms of sensitivity and signal-to-noise ratio [95, 68, 83, 100] allowing a comparable precision in single molecule localization approaches [67].

For the experiments in this thesis an EM-CCD camera (Andor DU-888E-C00-#BV-500) is used. EM-CCD cameras are based on conventional CCD chips with a shift register extended by a gain register. This register, which

Table 3.3: Measured g-factor values for different objectives measured in wide field and TIRF microscopy.

Objective (NA)	G-factor ($I_{\|\|}/I_{\perp}$)	std
4x (0.16)	1.24	0.04
10x (0.40)	1.23	0.02
20x (0.75)	1.21	0.02
40x (0.90)	1.20	0.02
60x (1.45)	1.20	0.02
60x (1.45, TIRF)	1.16	0.02

is consisting of pixels, shifts the charges of the acquired signal from pixel to pixel and in each shifting step the signal is multiplied by impact ionization [39] overcoming the readout noise of the camera. For a detailed description of EM-CCDs the reader is referred to [97].

3.4.1 Background correction

The microscope setup used in these experiments was the same for both ensemble measurements and single molecule measurements. To image single molecules, a highly sensitive camera with low readout noise is needed. Therefore an EM-CCD-camera is used in our setup, however this camera turned out to be not optimally suited for ensemble measurements as it shows smearing when operated with EM-gain at relatively high intensities.

To investigate the influence of smearing on the background level in anisotropy measurements and the consequences this has for the resulting anisotropy values, three different background images are taken:

1. The camera background is recorded while the sample is not illuminated.

2. An image is taken of a sample with imaging medium only. Laser power is set to the same constant value that is also used during anisotropy measurements.

3. An image of a drop of fluorescein diluted in water is taken. One channel is blocked by a black anodized beam block. The background is measured in the blocked channel.

Figure 3.5 shows the resulting intensity distributions. The sample not illuminated by the laser obviously shows the lowest background (black line). Background fluorescence from the imaging medium and backreflections from the laser cause the background intensity to slightly increase (blue line). However, the signal from the blocked channel in the fluorescein measurement shows the highest values. This indicates that charges from the illuminated side of the camera are transported to the non-illuminated side. The background in the non-illuminated channel is therefore considerably increased. To verify the appearance of smearing in anisotropy measurements the exper-

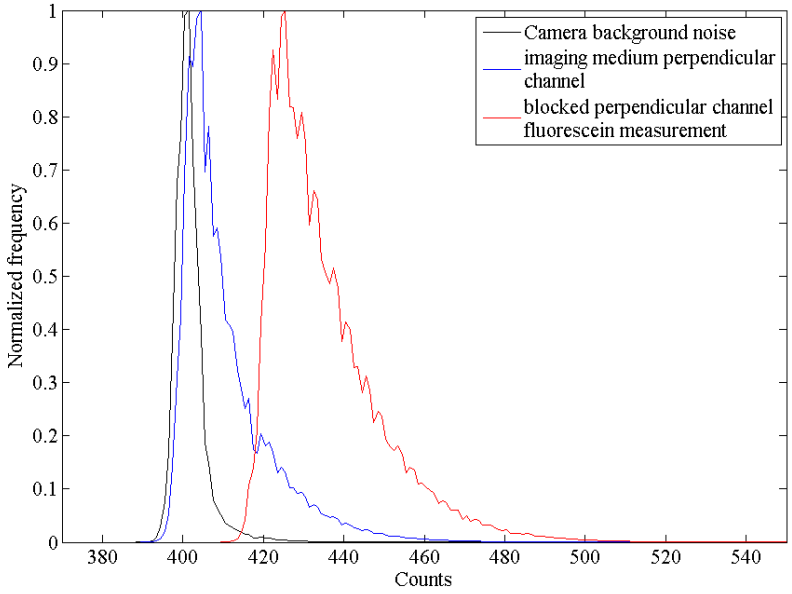

Figure 3.5: Effect of smearing on the background. Black line: Camera background noise when the sample is not illuminated. Blue line: A dish with imaging medium is illuminated with laser light at 476 nm and 0.75 mW in TIRF illumination. The background increases due to autofluorescence from the imaging medium and backreflections from the laser light. Red line: The perpendicular channel is blocked by placing a black anodized beam block just behind the polarizing beam splitter. An image of a drop of fluorescein in water is recorded. The measurement is carried out in TIRF. The concentration of fluorescein in water was chosen such that light intensities from the fluorescein in the parallel channel are comparable to typical anisotropy measurements. The background is measured in the blocked channel.

iment is repeated with cells transfected with monomeric Citrine (see chapter 4.1), while the perpendicular channel is blocked. Figure 3.6 shows an example of such a measurement. The smearing of the fluorescence signal is clearly visible. Smearing is strongly dependent on the intensity of the smeared signal as well as on the area covered on the CCD chip. For measurements of the G-factor this can be corrected by blocking each channel separately and measuring the background. However, correcting the background by blocking first the parallel then the perpendicular channel becomes impracticable for live cell measurements of multiple cells as the beam block has to be placed in the beam path manually, thereby slowing down the measurements substantially. To investigate the influence of the increased background on the anisotropy

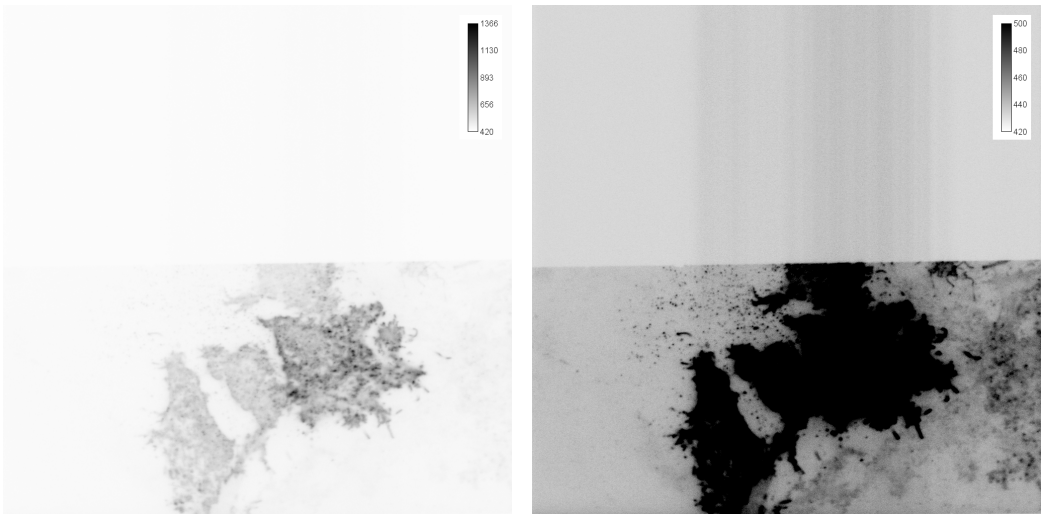

(a) (b)

Figure 3.6: Effect of smearing on the image background. The perpendicular channel (upper image half) is blocked, no light reaches the EM-CCD. The signal is only visible in the parallel channel (lower image half). (a) Image intensity scale is set to maximum range. (b) When the intensity range is lowered the smearing of the EM-CCD becomes visible. Note that for better visibility an inverted gray scale look up table is used.

values, the anisotropy for cells transfected with cytosolic monomeric Citrine (see chapter 4.1) is calculated for different background levels. Figure 3.7 shows the distribution of the measured anisotropy values for (a) the back-

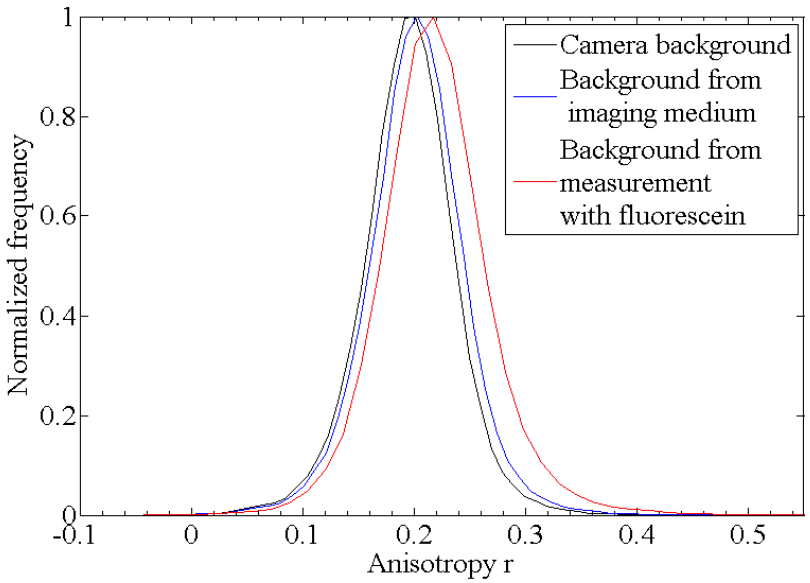

Figure 3.7: Effect of the background level on measured anisotropy values. Anisotropy distribution for a cell transfected with monomeric Citrine is shown for the background values shown in Figure 3.5. Black line: Camera background noise without sample illumination. Blue line: Background resulting from a dish with imaging medium. Red line: Background taken from a measurement of fluorescein diluted in water, where one channel is blocked and the background is measured in the blocked channel.

ground assumed to be only background noise from the camera, (b) the background resulting from imaging medium and (c) the background taken from the fluorescein measurement (note that the average intensity in fluorescein measurement is chosen to be comparable to the average fluorescence signal from a transfected cell). Obviously the underestimation of the background leads to a shift of the anisotropy to lower values.

To eliminate the crosstalk between the parallel and perpendicular channel due to smearing the camera is rotated by 90°. Although, rotation of the camera by 90° reduces the crosstalk of the smearing between the two channels it will not reduce the background itself. It might even lead to an overestimation of anisotropy values as the intensity in the parallel channel is usually higher and therefore might increase the background level more than the signal in the perpendicular channel. Moreover, an optimization of readout speeds and

light intensities might reduce the smearing of the camera; especially avoiding high EM-gain levels should reduce the effect of smearing.

3.5 Image registration of polarization data

Image registration of the two polarization channels is done by imaging of fluorescently labeled beads (Tetraspeck, Invitrogen, USA) and recording the position of a single bead in both channels. Fluorescently labeled beads are visible in both the parallel and perpendicular channel as the fluorescent molecules used to label these beads are distributed randomly over the bead and are thus contributing to the signals in both channels. Choosing a small bead size allows image registration with subpixel accuracy [33].

A sparse sample of fluorescent beads is used for image registration. A sparse sample allows direct identification of a single particle in both channels and is therefore preferred over dense samples. Image registration requires the mapping of different positions in both channels. Therefore multiple images are recorded, the sample is moved to different positions so that multiple positions in both channels are imaged. The bead positions are then localized. The positions for each bead determined in the localization step are then used to calculate a transformation matrix [33, 85].

4

Ensemble measurements by TIRF-anisotropy

This chapter presents ensemble measurements in fluorescence anisotropy microscopy. To verify the microscope setup, validation measurements are carried out in conventional wide field and in TIRF microscopy.

For ensemble measurements with far field excitation, fluorescein in glycerol is measured as an anisotropy standard. In TIRF, cells transfected with the fluorescence protein Citrine are measured, wide field results are then compared to results measured in TIRF. As an application to biology the spatial organization of the small GTPase Ras is investigated.

4.1 Materials and methods

4.1.1 Acquisition of microscopy data

Laser power was kept constant for all measurements, including background measurements, at $P_{\mathrm{TIRF}} = 0.75$ mW in TIRF and $P_{\mathrm{wf}} = 0.27$ mW in wide field measurements. To reduce imaging artifacts introduced by camera noise a sequence of 50 frames was acquired in each measurement and the average intensity over these 50 frames was calculated. For each cell a TIRF image and a wide field image were acquired. The TIRF angle was determined within the first measurement and kept constant for all subsequent measurements. Switching between TIRF illumination and conventional wide field illumination was achieved by translating the illumination lens vertically until the microscope objective was hit at the center (for wide field illumination) or at an off center position were total internal reflection takes place.

The instrument G-factor was measured by imaging a drop of fluorescein dissolved in water. Background noise was measured by recording a series of images of the imaging medium at the same laser power as used during measurements. Both G-factor measurements and measurements of the background noise were carried out in wide field and in TIRF microscopy.

4.1.2 Sample preparation

COS-7 cells were grown on glass bottomed tissue culture dishes (MatTek, Ashland, MA, USA) in DMEM + 10% FCS + 1% L-Glutamin. The cells were transfected with mCitrine-HRas and mCitrine-HRas-G12V at 80% confluency. The transfection of cells was performed with plasmid DNA and Effectene reagent (Qiagen, Germany). Cells were incubated for at least 20 hours at 37°C and 5% CO_2 before imaging. Cells transfected with mCitrine-HRas-wt were starved for 8 hours prior to the measurement. Growth medium was replaced by imaging medium containing Hepes buffer, pH 7.4 and DMEM without phenol red to reduce unspecific fluorescence. Measurements were performed at 37°C.

4.1.3 Data analysis

First, the average over each recorded time series was calculated. The average background image was then subtracted from the measurements and the average G-factor image. The background subtracted images were then divided by the G-factor image. Parallel and perpendicular channels were then registered. For this a sparse sample of Tetraspeck fluorescence beads (Invitrogen) was imaged. Beads visible in both channels were registered as described in chapter 3.5. After image registration anisotropy images were calculated. These images were masked by an image mask determined in the parallel image channel by thresholding. Anisotropy distributions were calculated including all measurements. Unless noted otherwise, errors shown are the standard error of the mean, meaning the standard deviation, given by:

$$\mathrm{std} = \left(\frac{1}{n-1} \sum_{i=1}^{n} (x_i - \bar{x})^2 \right)^{\frac{1}{2}} \tag{4.1}$$

of anisotropy values divided by the square root of the number of independent measurements. x_i is the measured data, $\bar{x}$ is the mean of x_i and n is the number of measurements of x_i.

4.2 Validation measurements

The functionality of the TIRF anisotropy microscope was tested by measuring control samples. As control samples cells transfected with monomeric and dimeric Citrine were used. The measured anisotropies were compared to wide field measurements.

4.2.1 Measurement of anisotropy in wide field microscopy

To validate the functionality of the microscope in conventional wide field mode, fluorescein in glycerol with a concentration of 5 µmol/L was measured. Due to the high viscosity of glycerol the rotational diffusion of fluorescein is

slowed down and the fluorescence anisotropy is increased. Reported values for a fluorescein glycerol mixture range from $r = 0.34$ to $r = 0.38$ [113, 106, 32, 31]. The rather large spread of values found in literature is based on the use of different setups and measurements at different temperatures. For a recent overview of available fluorescence anisotropy standards the reader is referred to [6].

A drop of the glycerol fluorescein solution was placed on a coverglass and imaged with a laser power of $P = 0.3$ mW and an exposure time of $t = 100$ ms. The measured fluorescence anisotropy for different objectives and the corrected values for high numerical aperture objectives are shown in Table 4.1. The measured values are in good agreement with the reported fluorescence anisotropy of fluorescein in glycerol.

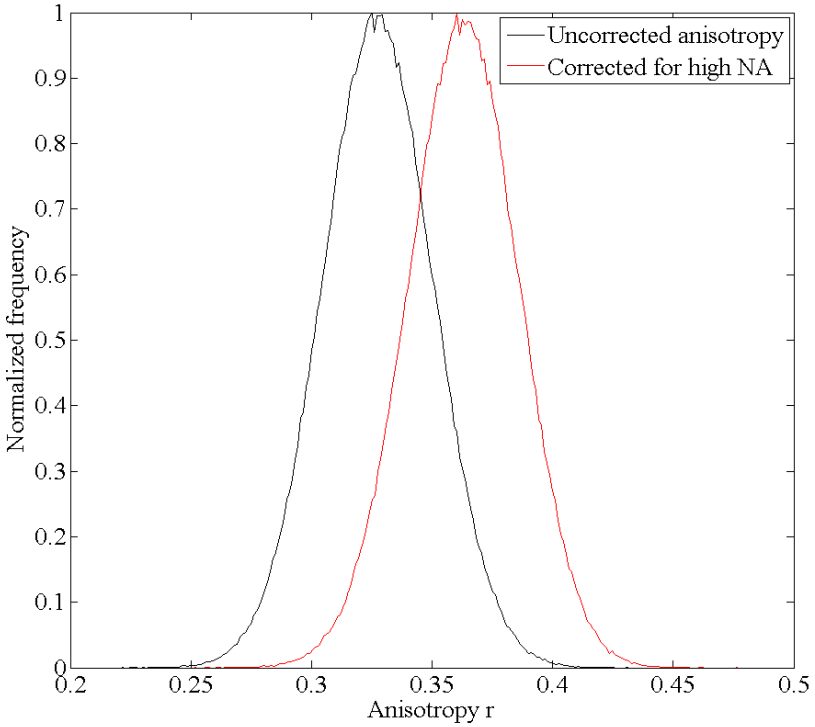

Figure 4.1: Measurement of a fluorescein glycerol standard in wide field fluorescence anisotropy with a 60x (1.45 NA) objective.

However, due to the refractive index of glycerol, this test sample is not

Table 4.1: Measured fluorescence anisotropy values of fluorescein in glycerol (5 µmol/L) for different objectives.

Objective (NA)	Anisotropy	std	Corrected anisotropy	std
4x (0.16)	0.36	0.03	0.36	0.03
10x (0.40)	0.36	0.02	0.37	0.02
20x (0.75)	0.36	0.02	0.38	0.02
40x (0.90)	0.35	0.03	0.38	0.03
60x (1.45)	0.32	0.03	0.36	0.03

suited for total internal reflection fluorescence microscopy as no total internal reflection can be achieved with a microscope objective with a numerical aperture of $NA = 1.45$ and the index of refraction of glycerol of $n = 1.474$ [63].

4.2.2 Measurement of cytosolic Citrine

To evaluate the performance of the system in TIRF microscopy the anisotropy of freely diffusing Citrine in the cytosol of cells was measured. Cells were transfected with monomeric Citrine and a test construct consisting of two Citrine molecules connected by a short linker (dimeric Citrine). This double Citrine construct shows energy transfer between the two molecules due to the short distance between the two Citrine molecules. Thus, fluorescence anisotropy decreases due to homo-FRET between the molecules. The experiments are carried out both in wide-field and in TIRF microscopy. Figure 4.2 shows a cell transfected with dimeric Citrine imaged in conventional wide-field and in TIRF illumination. The cytosolic Citrine is visible with TIRF illumination as well as with conventional wide field illumination and is therefore well suited for test measurements.

As the orientation distribution of molecules in cells is not known, no correction for high numerical aperture effects was made. As described earlier, the correction is derived for randomly oriented molecules and differs for non random orientation distributions. Furthermore, no correction for camera smearing was applied, background correction was applied by subtracting the background measured in a dish with imaging medium. No absolute anisot-

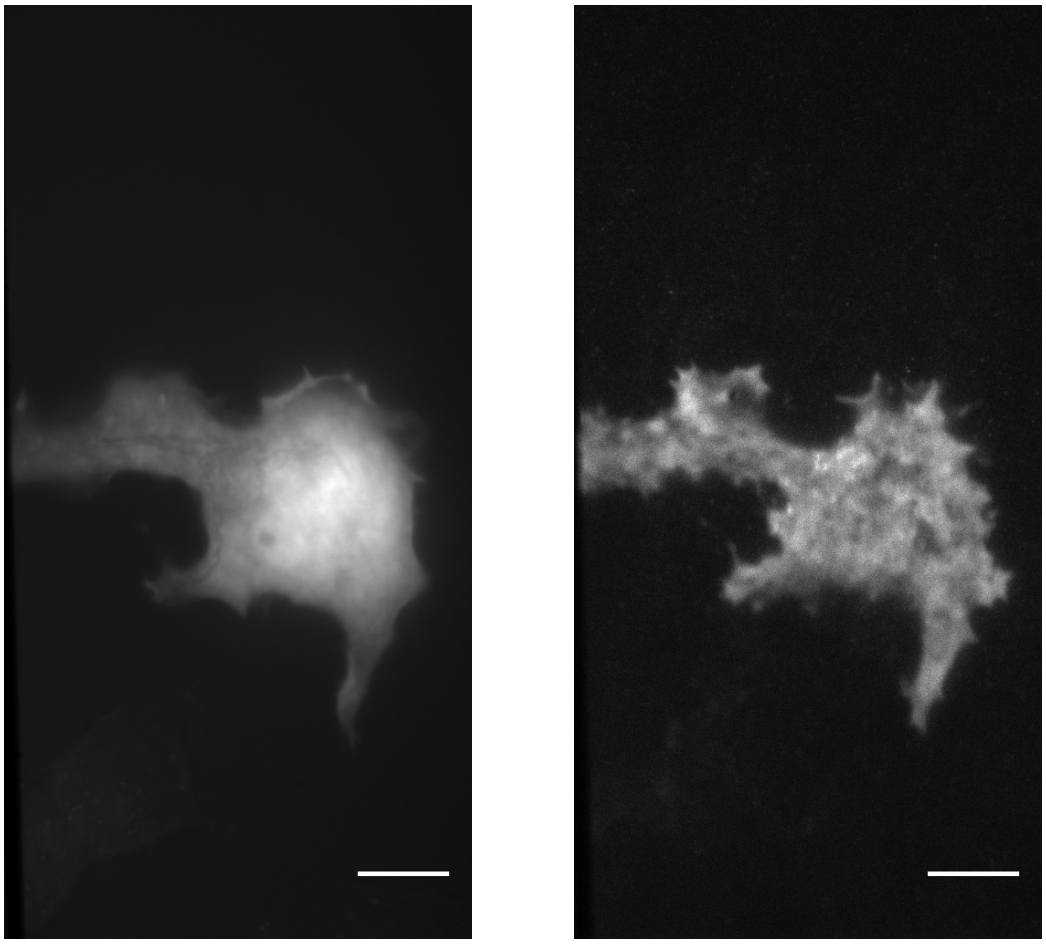

(a) (b)

Figure 4.2: A COS-7 cell transfected with cytosolic double Citrine imaged in (a) conventional wide field and in (b) TIRF microscopy. The scale bars are 10 µm.

ropy values are needed as the relative drop in anisotropy from the monomeric constructs to the dimeric constructs and the comparison with wide field measurements validate the experimental approach.

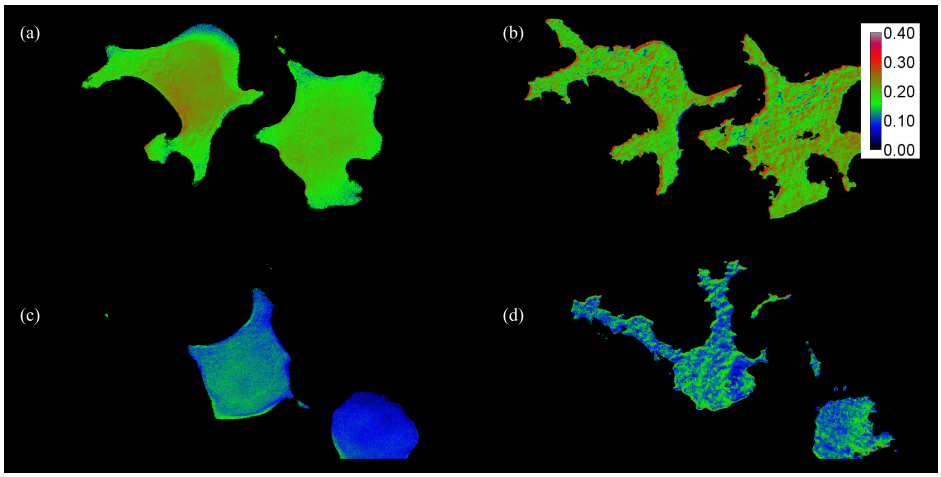

Figure 4.3: Homo-FRET detected by fluorescence anisotropy in TIRF and widefield microscopy. Fluorescence anisotropy images of MCF7 cells transfected with monomeric Citrine in (a) conventional wide field microscopy and (b) TIRF microscopy and MCF7 cells transfected with dimeric Citrine in (c) wide field and (d) TIRF microscopy.

Figure 4.3 shows a typical measurement. A clear drop in both conventional wide field and TIRF illumination in anisotropy for the double Citrine is visible. Table 4.2 shows average values and standard deviations for the steady state anisotropy for monomeric and dimeric Citrine in TIRF and widefield microscopy. The wide field measurements show a smaller drop in anisotropy than TIRF measurements. This might be caused by an increased background in wide field measurements, due to out of focus fluorescence.

Table 4.2: Measured anisotropy values for monomeric and dimeric Citrine in TIRF and wide field microscopy.

	mean anisotropy (TIRF)	std (TIRF)	mean anisotropy (wf)	std (wf)
monomeric Citrine	0.25	0.05	0.25	0.03
dimeric Citrine	0.18	0.05	0.21	0.03

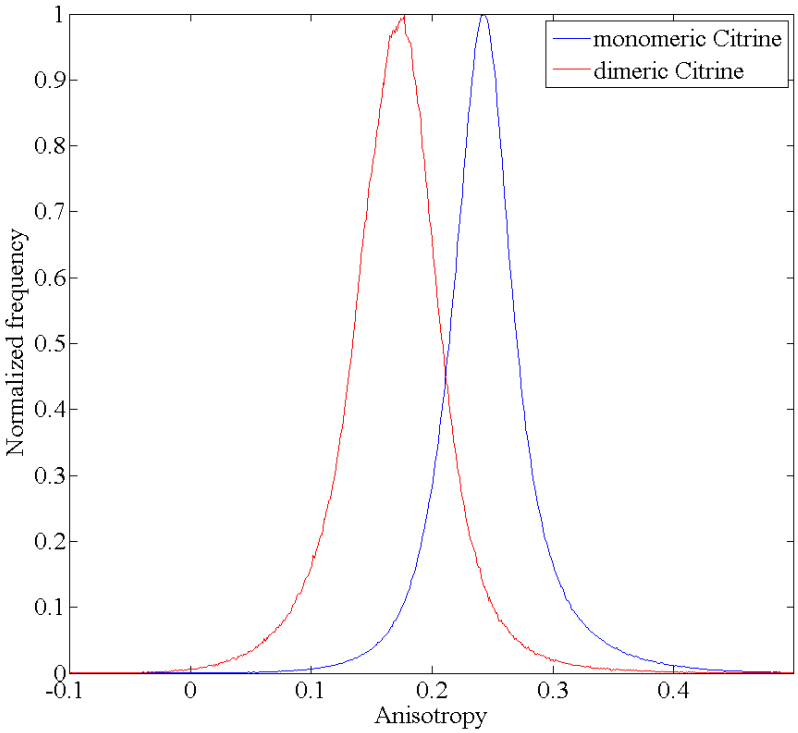

Figure 4.4: Distribution of fluorescence anisotropy for monomeric and dimeric Citrine measured in TIRF microscopy.

4.3 Application to biology

The membrane protein family of Ras proteins are small GTPases which regulate cell proliferation, differentiation, migration and apoptosis [3]. Ras proteins are reported to form small domains on the nanometer scale, which are not resolvable with conventional light microscopy due to the diffraction limit of light. Thus, the clustering of Ras is well suited for investigation with TIRF anisotropy microscopy by measuring homo-FRET. The biochemical properties of the Ras protein family are well known, however so far only electron microscopy [58] has been used to visualize these nano domains and no direct observation of the clustering has been done in living cells.

There are three closely related Ras proteins H- K- and NRas in humans. Here we will investigate HRas and KRas. HRas and KRas are membrane

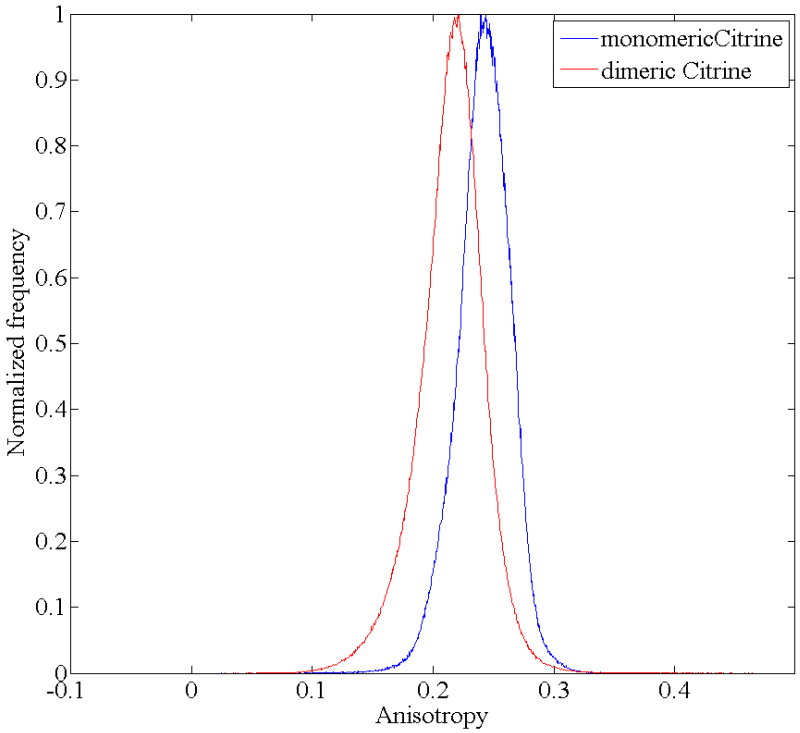

Figure 4.5: Distribution of fluorescence anisotropy for monomeric and dimeric Citrine measured in wide field microscopy.

bound proteins which are cycling between an active and an inactive state. In the active state GTP is bound whereas in the inactive state GDP is bound. The spatial organization of HRas and KRas and their constitutively active forms HRas-G12V and KRas-G12V are investigated by TIRF anisotropy. Both HRas and KRas are reported to organize in nanodomains in their active and their inactive forms [53].

Furthermore mCitrine-tH and mCitrine-tK are investigated. mCitrine-tH and mCitrine-tK contain all the Ras membrane-targeting signals of HRas and KRas, respectively. tK is reported to be distributed randomly over the plasma membrane whereas tH is reported to show a non-random distribution [94].

4.3.1 Spatial organization of HRas and KRas

The nanoscale spatial organization of HRas and its mutant HRas-G12V was investigated by TIRF anisotropy microscopy. In these experiments the anisotropy of monomeric Citrine in the cytosol of cells, wild type form of mCitrine-HRas and its constitutively active form mCitrine-HRas-G12V was measured. Cells were imaged in conventional wide field and in TIRF microscopy. Figure 4.6 shows a typical measurement of mCitrine-HRas-wt imaged with TIR excitation. The anisotropy distributions for wide field and TIRF measurements are shown in Figure 4.7 and Figure 4.8. Table 4.3 shows the mean values and the corresponding standard deviations. The anisotropy dis-

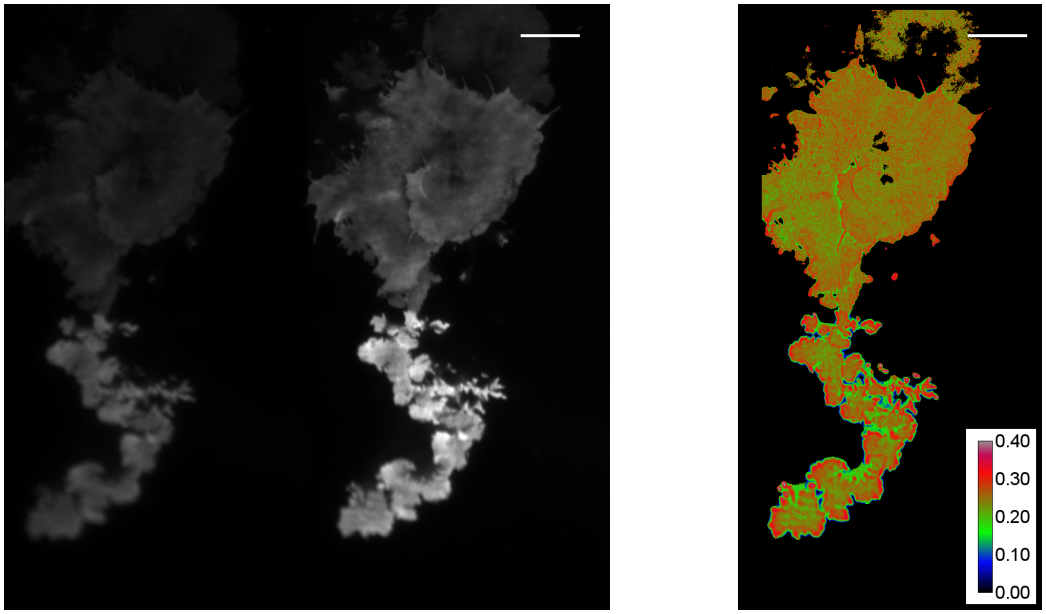

(a) (b)

Figure 4.6: A COS-7 cell transfected with mCitrine-HRas-wt imaged in (a) TIRF and the corresponding anisotropy image (b). The scale bar is 10 µm.

tribution indicates small differences in the anisotropy of monomeric Citrine in the cytosol of cells, mCitrine-HRas wild type and mCitrine-HRas-G12V evident in the shape of the distributions. These differences seem to be smaller in TIRF. The mean anisotropy values both in conventional wide field and TIRF microscopy are slightly smaller than those of freely diffusing mCitrine in the

cytosol of cells, however due to the high standard deviations no conclusion can be made.

Table 4.3: Measured anisotropy values for monomeric Citrine, HRas wild type and HRas-G12V in TIRF and wide field microscopy.

	mean anisotropy (TIRF)	std (TIRF)	mean anisotropy (wf)	std (wf)
monomeric Citrine	0.25	0.05	0.25	0.03
HRas-wt	0.23	0.05	0.24	0.04
HRas-G12V	0.23	0.05	0.24	0.05

Figure 4.9 and 4.10 show the anisotropy distributions measured for mCitrine-KRas-wt and mCitrine-KRas-G12V compared to the cytosolic mCitrine control. The mean values are given in Table 4.4. Both the KRas-wt anisotropy distribution and the KRas-G12V anisotropy distribution measured in conventional wide field microscopy seem to be shifted to higher anisotropy values, this is not visible in TIRF measurements. However, the mean anisotropy values show no significant deviation from monomeric Citrine.

Table 4.4: Measured anisotropy values for monomeric Citrine, KRas wild type and KRas-G12V in TIRF and wide field microscopy.

	mean anisotropy (TIRF)	std (TIRF)	mean anisotropy (wf)	std (wf)
monomeric Citrine	0.25	0.05	0.25	0.03
KRas-wt	0.23	0.04	0.26	0.04
KRas-G12V	0.24	0.05	0.25	0.06

Figure 4.11 and 4.12 show the fluorescence anisotropy distribution of the membrane anchors tH and tK measured with conventional wide field and TIR illumination. The anisotropy distribution measured with conventional wide field illumination suggests a slightly higher anisotropy for tK than for tH. The distribution is shifted to higher anisotropy values compared to cytosolic mCitrine. No clear differences are visible in TIRF measurements. However, mean values listed in Table 4.5 show no significant differences.

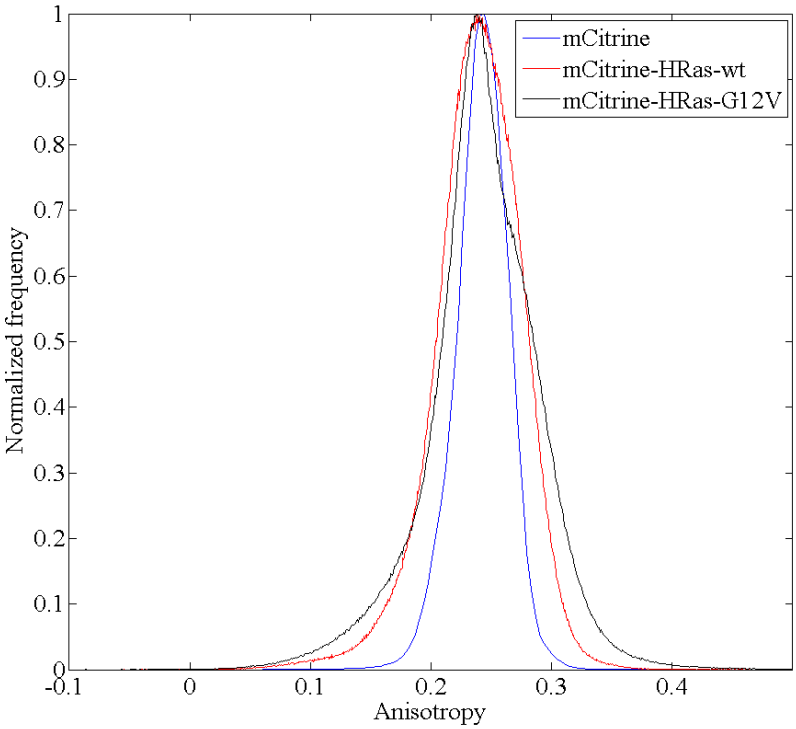

Figure 4.7: Distribution of fluorescence anisotropy for monomeric Citrine, mCitrine-HRas and mCitrine-HRas-G12V measured in wide field microscopy.

4.4 Conclusion

In this chapter the proper functionality of the TIRF anisotropy microscope was validated. First wide field measurements on a fluorescein glycerol standard were carried out for different objectives. The measured values agree with values reported for the measured standard [106]. A decrease in anisotropy was seen for high NA objectives. For a randomly distributed sample this can be corrected for [9, 10]. Further controls were carried out in live cell measurements. Cells were transfected with a monomeric and a dimeric Citrine construct and measured in conventional wide field and TIRF microscopy. It is worth noting, that the measurements presented here were carried out with a high numerical aperture objective which leads to a mixing of polarization components and thereby reducing the fluorescence anisotropy.

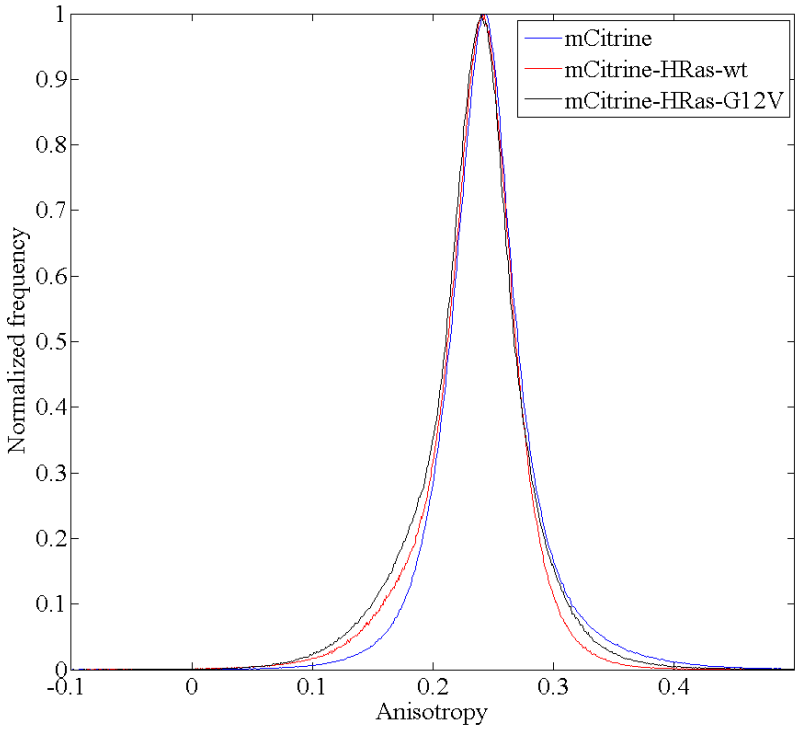

Figure 4.8: Distribution of fluorescence anisotropy for monomeric Citrine, mCitrine-HRas and mCitrine-HRas-G12V measured in TIRF microscopy.

Measurements in cells were not corrected for high numerical aperture effects as the underlying orientation distribution of the fluorophores is not known.

Measurements showed similar anisotropy values for wide field and TIRF measurements. However, both anisotropy distributions determined in conventional wide field and in TIRF show a rather high standard deviation of 0.03 (wide field) and 0.05 (TIRF). The higher intensities in wide field measurements of cytosolic Citrine lead to a smaller standard deviation than in TIRF measurements. However, measurements of membrane bound proteins like Ras show anisotropy distributions with comparable widths. The large spread of the anisotropy distribution might even lead to occurrences of negative anisotropy values or anisotropy values exceeding the fundamental anisotropy of randomly distributed molecules of $r_0 = 0.4$. Anisotropy distributions measured in TIRF microscopy are less prone to skewing than

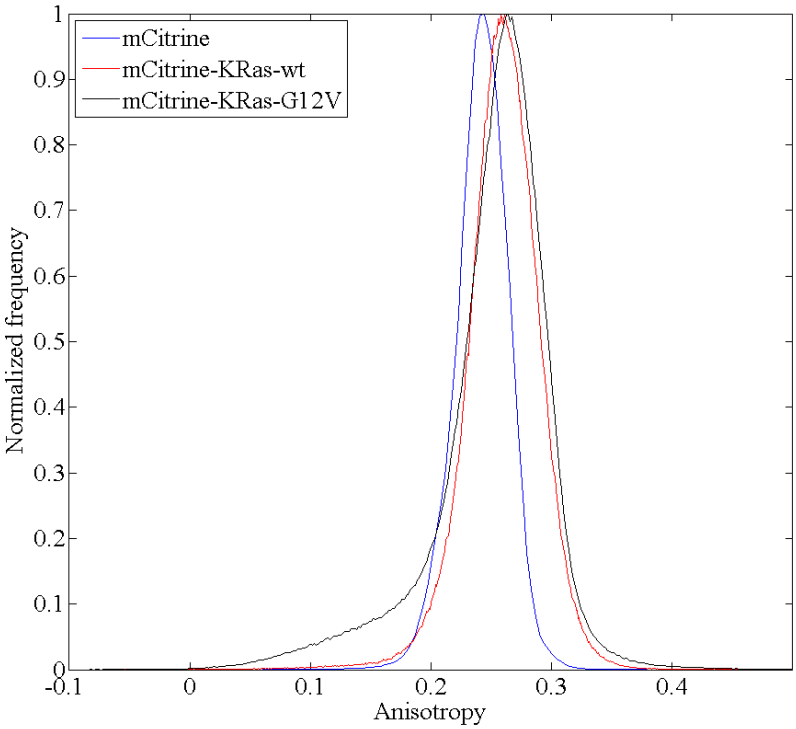

Figure 4.9: Distribution of fluorescence anisotropy for monomeric Citrine, mCitrine-KRas and mCitrine-KRas-G12V measured in wide field microscopy.

distributions measured in conventional wide field microscopy. This can be explained by the different background levels in wide field and TIRF microscopy. Background is greatly reduced in TIRF compared to conventional wide field measurements. The higher background levels in far field excitation might also explain the smaller drop in anisotropy measured for dimeric Citrine.

However, the drop in anisotropy from monomeric to dimeric Citrine was clearly visible in wide field and TIRF microscopy. The microscope thus is capable of resolving relative changes in anisotropy.

As a biological application the spatial organization of the small GTPase Ras was investigated. Anisotropy measurements were carried out and compared to monomeric cytosolic Citrine which does not show any clustering or dimerization at low concentrations. Table 4.6 shows a summary of all measurements carried out and lists the determined mean anisotropy values and

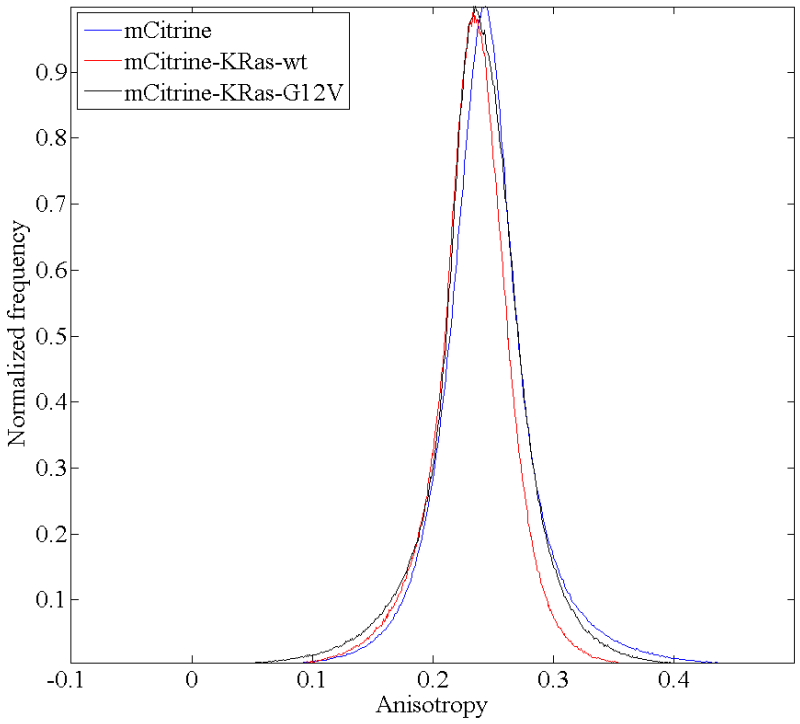

Figure 4.10: Distribution of fluorescence anisotropy for monomeric Citrine, mCitrine-KRas and mCitrine-KRas-G12V measured in TIRF microscopy.

their standard deviations.

The data shows no differences in the mean anisotropy values of HRas-wt, HRas-G12V and cytosolic mCitrine within the standard deviations. However, the general shape of the anisotropy distribution measured in conventional wide field illumination differs. This might be caused by the increased background. Generally wide field measurements suffer from higher background levels due to out of focus fluorescence. This effect is increased through the thresholding step during data analysis as background fluorescence reduces the signal-to-noise ratio.

In a next step KRas-wt and KRas-G12V were compared to cytosolic mCitrine. The anisotropy distribution measured in conventional wide field microscopy of both KRas-wt and KRas-G12V are shifted to higher anisotropy values exceeding the anisotropy of freely diffusing mCitrine. However,

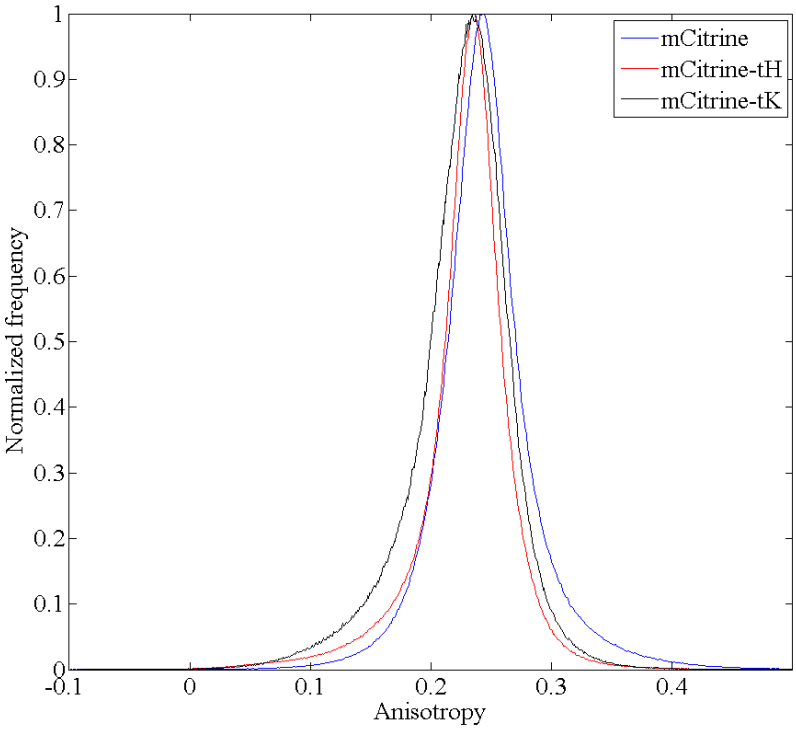

Figure 4.11: Distribution of fluorescence anisotropy for monomeric Citrine, mCitrine-tH and mCitrine-tK measured in TIRF microscopy.

again the mean values do not significantly differ from the mean anisotropy of cytosolic mCitrine. This shift to higher values is not visible in TIRF measurements. Generally, higher values exceeding the mCitrine control could be explained by orientational effects caused by non freely diffusing proteins, however these are more likely to appear in the plasma membrane than in the cytosol and therefore TIRF measurements should be shifted to higher values.

Furthermore, mCitrine-tH and mCitrine-tK were investigated. tK is reported to be distributed randomly over the plasma membrane whereas tH is reported to show a non-random distribution [94]. The mean anisotropy values show no significant difference. The anisotropy distribution of tK measured in conventional wide field is slightly shifted to higher anisotropy values. However, this shift is not visible in the anisotropy distributions measured in TIRF microscopy.

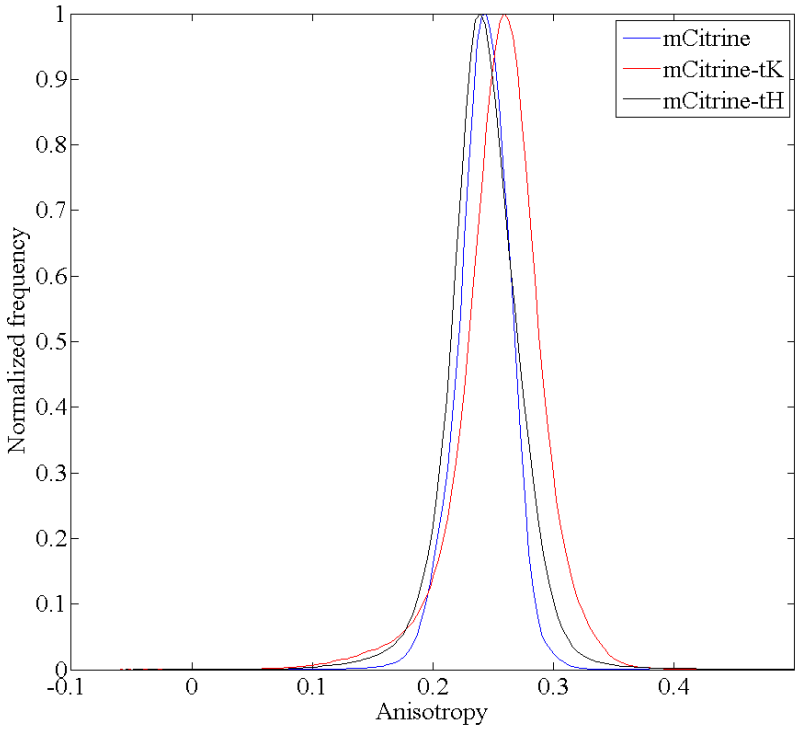

Figure 4.12: Distribution of fluorescence anisotropy for monomeric Citrine, mCitrine-tH and mCitrine-tK measured in wide field microscopy.

A comparison of wide field and TIRF measurements shows similar anisotropy values. No significant differences are visible in both methods. However, as mentioned earlier wide field measurements are more prone to skewing of the anisotropy distribution.

The clustering of HRas is reported to mainly occur on the membrane therefore cytosolic signal should lead to an increase in anisotropy. As no absolute anisotropy values are recorded, the values measured in wide field and TIRF cannot be directly compared.

Generally the anisotropy measurements are hampered by high noise levels, making it difficult to interpret measurements. The standard error of the measurements can be reduced by increasing the number of measurements, however, high noise levels will limit this "high throughput" approach.

Although the measurement of absolute values is difficult, relative changes

Table 4.5: Measured anisotropy values for monomeric Citrine, tH and tK in TIRF and wide field microscopy.

	mean anisotropy (TIRF)	std (TIRF)	mean anisotropy (wf)	std (wf)
monomeric Citrine	0.25	0.05	0.25	0.03
KRas-wt	0.23	0.05	0.24	0.04
KRas-G12V	0.23	0.05	0.26	0.04

can be observed with anisotropy microscopy. Therefore, relative changes on a single cell level, for example changes of the spatial organization of HRas upon stimulation with EGF, could possibly be observed.

Furthermore, orientation effects caused by non-random orientation of proteins anchored in the plasma membrane have to be considered [28]. Non-random orientation of proteins can bias measurements as the fluorophores have to be aligned with the polarization of the excitation light to be excited optimally. Photoselection of the fluorophores in anisotropy measurements therefore has to be taken into account. To overcome the high noise levels in ensemble measurements and to reduce orientation effects, measurements can be carried out on a single molecule level. Anisotropy then reduces to a measure of orientation of the molecules.

Table 4.6: Measured anisotropy values in TIRF and conventional wide field microscopy.

	mean anisotropy (TIRF)	std (TIRF)	mean anisotropy (wf)	std (wf)
mCitrine	0.25	0.05	0.25	0.03
dCitrine	0.18	0.05	0.21	0.03
HRas-wt	0.23	0.05	0.24	0.04
HRas-G12V	0.23	0.05	0.24	0.05
KRas-wt	0.23	0.04	0.26	0.04
KRas-G12V	0.24	0.05	0.25	0.06
tH	0.23	0.05	0.24	0.04
tK	0.23	0.05	0.26	0.04

5

Single molecule measurements by polarized TIRF

Anisotropy is a measure of the depolarization of an ensemble of molecules caused by rotational diffusion or by FRET resulting from the dipole-dipole interaction of single molecules in close proximity. The measurement of anisotropy reduces to a measure of orientation of the emission dipole moment when carried out on a single molecule level, making it more appropriate to talk about polarization or orientation measurements rather than anisotropy measurements. In this chapter the possibilities for measuring molecule orientations will be discussed.

5.1 Materials and Methods

5.1.1 Acquisition of microscopy data

Orientation measurements of Pt-complex fibers

Platinum-complex was imaged with three different excitation polarizations. For every polarization direction a single image was acquired with an exposure time of 200 ms and an EM-Gain set to 200. Laser power was set to 3 mW (measured before the microscope objective) and kept constant over all measurements. The Pt-complex was excited at 476 nm and a triple band dichroic beam splitter (Z 405/473/561, AHF, Tübingen) and laser rejection filter (405/473/561, AHF, Tübingen) were used for imaging.

Orientation measurement of single molecules

Data was acquired as a sequence of images under constant illumination. The sample was excited at 568 nm and laser power was set to 10 mW (measured at the back focal plane of the microscope objective). A triple band dichroic beam splitter (Z 405/473/561, AHF, Tübingen) and laser rejection filter (405/473/561, AHF, Tübingen) were used for imaging. An additional emission filter (HC 609/54, AHF, Tübingen) was placed in the emission path.

5.1.2 Sample preparation

For the validation measurements a drop of the Pt-complex in solution was dried on a cover glass, and imaged at an excitation wavelength of 476 nm. The Pt-complex was provided by Dr. Christian Strassert (University of Münster).

For single molecule measurements glass bottomed tissue culture dishes (MatTek, Ashland, MA, USA) were incubated for 5 minutes with Poly-L-Lysine (PLL, 0.01% in PBS, Sigma, Schnelldorf, Germany), then washed once with PBS and twice with ddH_2O and dryed over night at room temperature. To add Biotin on the surface, PLL coated slides were incubated for 30 minutes with EZ-Link Sulfo-NHS-Biotin (Thermo Scientific, Ulm, Germany), washed 3 times with PBS. A 5 µL drop of labeled streptavidin was

placed in the middle of a well and incubated for 5 minutes at room temperature. Streptavidin and Atto 550 Biotin (both Sigma-Aldrich, Schnelldorf, Germany) were mixed in a 1:3 ratio with a streptavidin concentration of 10 or 20 fmol per 5 µL drop. Atto 565 labeled streptavidin (about 3-4 dye molecules per streptavidin) was provided by Michael Sonntag (TU Eindhoven, Netherlands). Dishes were washed twice with PBS + 0.5% BSA and once with PBS.

5.1.3 Data analysis

Parallel and perpendicular channels are registered and overlaid. Single molecule data is analyzed by selecting a region of interest around each fluorescent spot and plotting the total intensity within this region of interest against the frame number. Bleaching of molecules is evident in these curves as a step-wise decrease of the fluorescent signal. The intensity measured in the parallel and perpendicular channels shows a cosine squared dependency on the orientation of the molecule relative to the measured directions. The angle Θ in a two dimensional plane with base vectors oriented along $I_{\parallel}$ and $I_{\perp}$ is then given by

$$\Theta = \arctan\left(\sqrt{\frac{I_{\perp}}{I_{\parallel}}}\right) \tag{5.1}$$

5.2 Validation measurements

To show the capability to resolve orientation by polarization measurements, a suitable test sample is needed. A Platinum complex [105] was chosen for validation measurements as its signal exceeds that from single fluorescent molecules by far and at the same time shows a strongly polarized emission. Therefore, the Pt-complex is ideally suited for validation measurements. It forms fibers of 8 nm in diameter that show a strongly polarized emission.

The Platinum(II)-complex belongs to the group of phosphorescent heavy metal complexes. The electronic charge shifts from a molecular orbit with a metal like character to a molecular orbit with a ligand like character and is thus called a metal-to-ligand-charge-transfer-complex (MLCT-complex).

In the case of the Pt(II)-complex used in this thesis the electronic charge shifts from a Pt-Pt bond in its triplet state to a molecular orbit with a ligand like character and is therefore called ^{3}MMLCT. For an in-depth review of the underlying processes of luminiscent Platinum complexes and their synthesis the reader is referred to [30, 37, 2, 115]. The Platinum-complex used in the present work was excited at 476 nm with an emission maximum of 580 nm. Figure 5.1 shows an electron microscopy image of such fibers and their emission spectra.

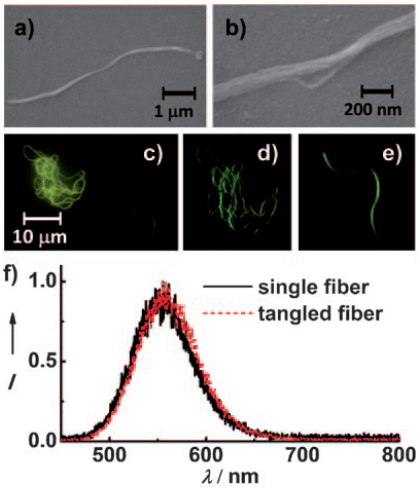

Figure 5.1: (a,b) Electron microscopy images of a single fiber. (c, d, e) Fluorescence microscopy images of fibers. (f) Emission spectra of single and tangled fibers. Reprinted with permission from reference [105]. Copyright (2011) Wiley-VCH Verlag GmbH & Co. KGaA.

5.2.1 Measurement of orientation of Pt-Complex fibers

To validate the possibility to resolve molecular orientations with the microscope presented in this thesis, a platinum complex was imaged. This complex forms thin fibers of 8 nm in diameter and shows a polarized emission as well as a strong dependency on the excitation light polarization due to photo selection. Therefore, these samples can be used to probe the possibility to resolve orientations on the emission side as well as to probe the polarization of the TIRF field.

The Platinum complex is imaged with three different excitation polarizations in TIRF:

1. In-plane linearly polarized light, subsequently referred to as x-polarization.
2. In-plane linearly polarized light rotated by 90°, subsequently referred to as y-polarization.
3. z-polarized light, with a main component along the optical axis. This polarization state has a small y-component but no x-component.

Figure 5.2(a) shows a Pt-fiber excited with linearly polarized light imaged in TIRF. The left channel shows the emission polarization parallel to the excitation light and the right channel shows the emission polarization perpendicular to the excitation light.

An overlay of the two channels (see Figure 5.2(b)) shows the differences in both channels. If the fiber is oriented along the y-axis (perpendicular to the excitation light polarization) the signal vanishes almost completely in the channel parallel to the excitation polarization and is maximal in the perpendicular channel. If the fiber is oriented in x-direction the emission polarization changes from mainly y-polarized light to mainly x-polarized light.

By rotating the polarization of the incident light and moving the beam in the back focal plane of the microscope, the polarization of the TIRF field was rotated by 90° in the sample plane resulting in purely y-polarized light. Figure 5.3(b) shows the resulting image for the fiber imaged before. Note that by rotating the excitation light, the parallel and perpendicular channels are switched. The fiber oriented along the y-axis results in parallel polarized light and x-orientations of the fiber result in light being polarized perpendicular to the incident light polarization. Thus, measuring the emission polarization becomes a measure of orientation of the Pt-complex.

The excitation beam is then adjusted to generate a TIRF field with a main polarization component along the optical axis and a minor y-component. This is done by moving the beam to its original position in the back focal plane and rotating the polarization by 90°. The resulting image is shown in Figure 5.4(a). The left channel corresponds to a purely perpendicular

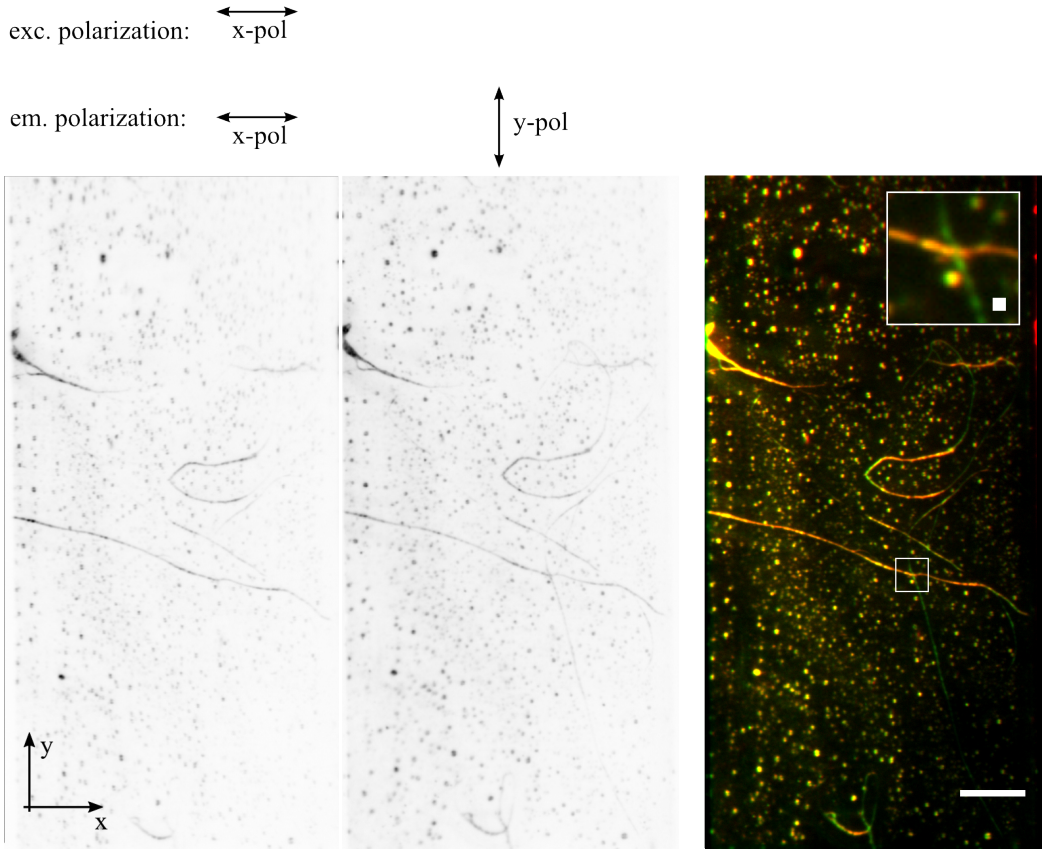

Figure 5.2: Orientation imaging of a Platinum complex. (a) A platinum fiber is imaged. The left channel shows the emission polarization parallel to the excitation light. The right channel shows the emission polarization perpendicular to the excitation light polarization. (b) An overlay of the parallel (red) and perpendicular (green) channels. The inset shows a high magnification view of the boxed region. Scale bars are 10 µm and 500 nm in the inset.

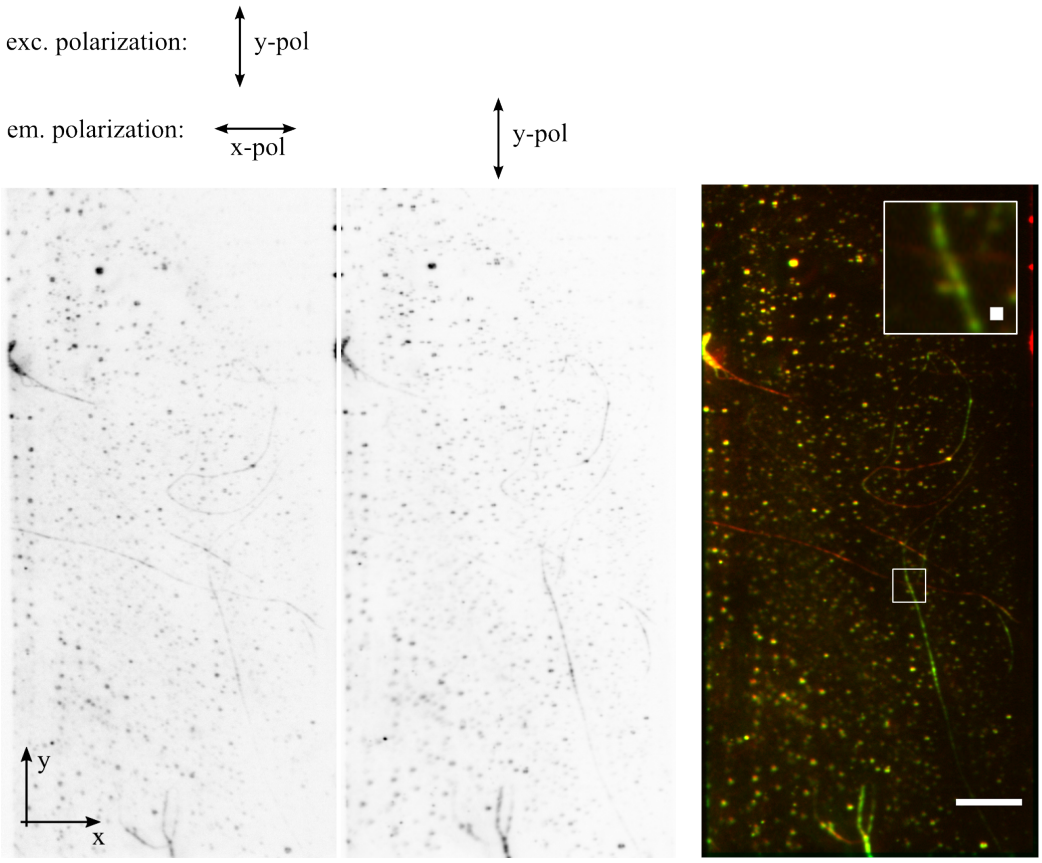

(a) (b)

Figure 5.3: Orientation imaging of a Platinum complex, with the excitation light polarization rotated by 90°. (a) The left channel shows the emission polarization perpendicular to the excitation light. The right channel shows the emission polarization parallel to the excitation light polarization. (b) An overlay of the parallel (green) and perpendicular (red) channels. The inset shows a high magnification view of the boxed region. Scale bars are 10 µm and 500 nm in the inset.

channel, it images the x-component of the polarization. The right channel shows the y-component of the polarization and is thus parallel to the minor y-component of the excitation light. Both channels show the fiber and all possible fiber orientations are visible. However, the overlay shows that y-components of the fiber dominate in the y-polarized channel. This is in agreement with the measurement where the excitation light was linearly polarized in y-direction. Thus, the preferred excitation of horizontal fiber components is caused by the y-component of the excitation light. It has to be noted that molecules oriented along the optical axis (z-orientation) will contribute to both channels x and y due to the high numerical aperture of the objective [45, 110].

5.3 Orientation measurement of single molecules

On a single molecule level orientation polarization imaging is simplified as the polarization of the emission light of a single molecule does not depend on the excitation light polarization. The excitation light polarization determines the excitation probability and is measured on the emission side by the number of photons emitted per time [77]. However, the orientation of the molecule results in different relative contributions to the parallel and perpendicular channel. The method presented here is based on a method published earlier for dpi-fluorescence [54] and is capable of measuring a projection of the 3d orientation on to a 2d-plane, where $I_{\perp}$ and $I_{\parallel}$, the intensities measured in the perpendicular and parallel channel, are the base vectors. Due to the rotation symmetry only angles between 0°and 90°can be determined, however the relative orientation of two molecules can be inferred with this method.

Figure 5.5(a) shows the intensity of the fluorescence signal measured in the parallel and perpendicular channels for a typical 1000 frame acquisition. The bleaching steps of the dye molecules are visible in both channels and result in a drop of the total intensity. Figure 5.5(a) shows bleaching steps in frame 44, 132 and 256. At frame 310 another molecule appears and bleaches

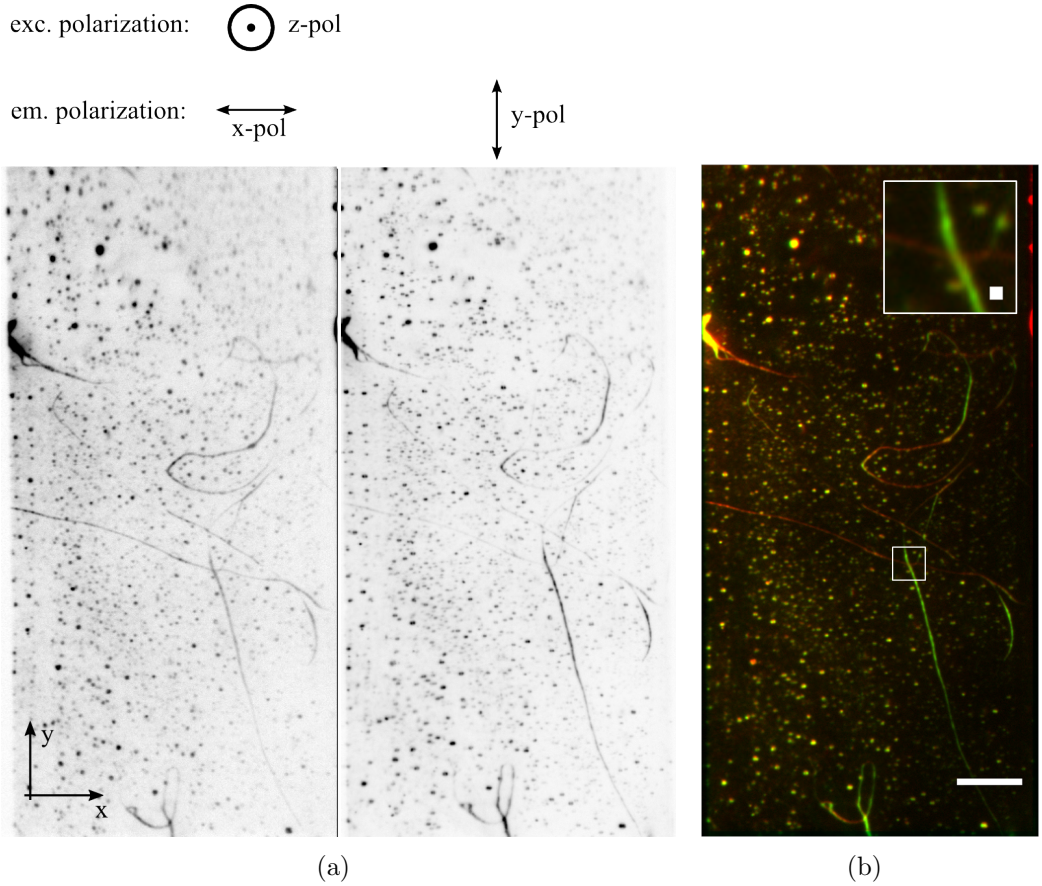

Figure 5.4: Orientation imaging of a Platinum complex. (a) A platinum fiber is imaged with out-of-plane polarization. The left channel shows the emission polarization purely perpendicular to the excitation light. The lower channel shows the emission polarization which is parallel to the excitation light minor polarization component. (b) An overlay of the y- (red) and x-channel (green). The inset shows a high magnification view of the boxed region. Scale bars are 10 µm and 500 nm in the inset.

in frame 345.

The average orientation can be calculated according to equation (5.1) and is plotted Figure 5.5(b). Assuming that each bleaching step corresponds to the bleaching of a single molecule and neglecting reorientation and energy transfer between the fluorophores, the number of fluorophores as well as the relative orientation in a 2d plane can be calculated. For a measurement with two bleaching steps, assuming that each bleaching step corresponds to a single molecule, the intensities measured in the parallel and perpendicular channels are given by:

$$I_{\parallel} = I_{01} \cos^2(\Theta_1) + I_{02} \cos^2(\Theta_2), \tag{5.2a}$$

$$I_{\perp} = I_{01} \sin^2(\Theta_1) + I_{02} \sin^2(\Theta_2), \tag{5.2b}$$

with I_{01} and I_{02} being the excitation probability of each molecule and Θ_1 and Θ_2 being the angle between the emission dipole of a molecule and axis defined by the parallel polarization channel. The excitation probability shows a cosine squared dependency on the angle between the excitation light polarization and the absorption dipole moment of the molecule [52]. Assuming that the emission and absorption dipole moments are parallel, this leads to:

$$I_{\parallel} \propto \cos^4(\Theta_1) + \cos^4(\Theta_2), \tag{5.3a}$$

$$I_{\perp} \propto \cos^2(\Theta_1) \sin^2(\Theta_1) + \cos^2(\Theta_2) \sin^2(\Theta_2). \tag{5.3b}$$

Note that any effects on the excitation probability other than the angle between absorption dipole moment and the excitation light polarization are neglected here.

The orientation of one of the two molecules can be calculated in a straightforward manner after photobleaching the other molecule by equation (5.1). To calculate the orientation of the second molecule, the intensity after a bleaching step has to be subtracted from the intensity measured before the bleaching step in each channel. The resulting intensity is then the intensity emitted by a single molecule and thus its orientation can be calculated. How-

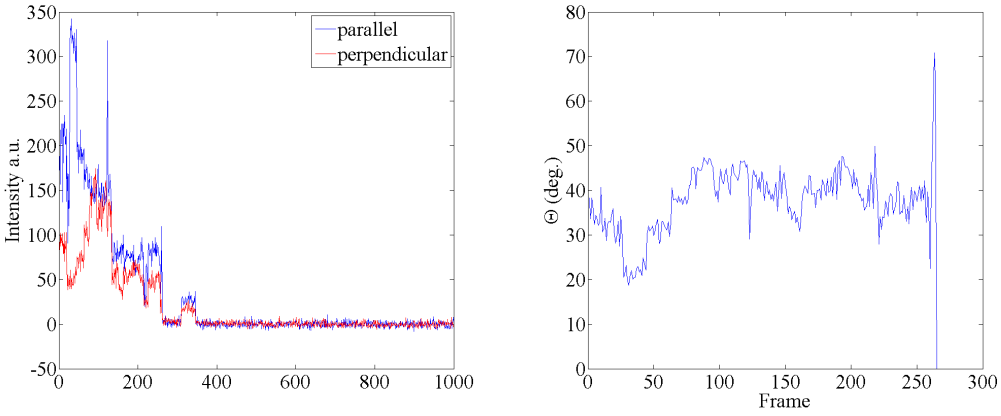

(a) (b)

Figure 5.5: (a) A typical stepwise bleaching experiment. Streptavidin labeled with Atto 565 was imaged for 1000 frames. The plot shows the fluorescence intensity measured in the parallel (blue) and perpendicular (red) channel for a single streptavidin molecule plotted against the frame number. Bleaching steps of single Atto 565 molecules are visible at frames 44, 132 and 256. A molecule appears on frame 310 and vanishes in frame 345. (b) The calculated orientation plotted for the first 250 frames.

ever, this method assumes that no energy transfer occurs between molecules.

Figure 5.6(a) shows the bleaching steps found for a different set of molecules. Initially the molecules show strong blinking, before stabilizing to a constant signal. The parallel channel shows a clear drop in intensity, however the intensity in the perpendicular channel increases when the total intensity decreases. Reorientation of molecules at the exact moment of bleaching is unlikely, and the only possible source for an increase in one polarization channel is energy transfer between molecules. As the total intensity should not be affected by the reorientation of the molecule, it is very likely that the loss of energy transfer upon bleaching of one fluorophore leads to an increase in the perpendicular channel. The efficiency of FRET between two molecules is given by equation (2.9) and is the same for both molecules. The excitation probability of a single molecule depends on its position but also on its orientation relative to the excitation polarization. The excitation probability of two molecules undergoing FRET can thus be different and, although the

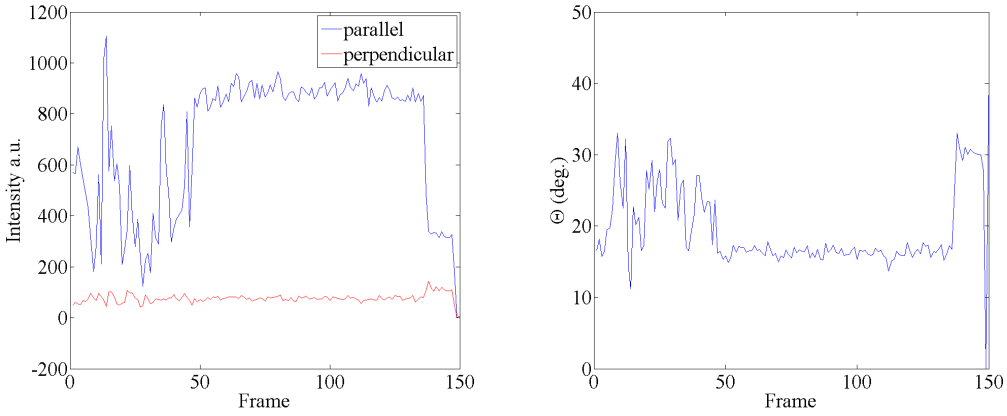

(a) (b)

Figure 5.6: homo-FRET in single molecule orientation imaging. (a) Example of FRET in a stepwise bleaching experiment of single molecules. Streptavidin labeled with Atto 565 is imaged for 1000 frames (Frames from 1 to 150 shown here). A bleaching step is visible at frame number 140 in the parallel signal. (b) Orientation calculated for the shown curve.

FRET efficiency is the same for the two molecules, the absolute energy transfer from one molecule to another can be different resulting in a net energy transfer different from zero.

The net energy transfer leads to a change in the relative contributions in the parallel and perpendicular channels from the two molecules and equations (5.3a) and (5.3b) have to be modified. Each term has to be extended by an additive term resulting from the energy transfer to the molecule and a subtractive term resulting from the energy transfer from the molecule:

$$I_{\parallel} \propto (1-E)\left(\cos^4\Theta_1 + \cos^4\Theta_2\right) + 2E\cos^2\Theta_1\cos^2\Theta_2, \tag{5.4a}$$

$$\begin{aligned} I_{\perp} \propto{}& (1-E)\left(\sin^2\Theta_1\cos^2\Theta_1 + \sin^2\Theta_2\cos^2\Theta_2\right) \\ &+ E\left(\sin^2\Theta_1\cos^2\Theta_2 + \sin^2\Theta_2\cos^2\Theta_1\right). \end{aligned} \tag{5.4b}$$

The orientation of one of these molecules can still be calculated after photo-bleaching of the other molecule, since the FRET vanishes. However

to calculate the orientation of the other molecule, the FRET efficiency E, which in fact depends on the relative angle between the two molecules, has to be known.

Therefore, in the presence of FRET, the relative angle between the molecules cannot be calculated easily. Furthermore, the effect of FRET is dependent on the absolute orientation of the pair of molecules, making it difficult to even derive qualitative conclusions about the relative orientation of the molecules from the measurement of a single pair. Neglecting the influence of FRET on the orientation, the angle Θ can be calculated for each bleaching step for this data, resulting in a relative orientation of the two molecules of $\Theta_1 - \Theta_2 = 13°$.

5.4 Conclusion

This chapter discusses the possibilities for deducing molecule orientations in a 2d plane from polarization measurements. To validate the proper functioning of the microscope, a Pt-complex which forms fibers of 8 nm thickness was imaged. The Pt-fibers show a strongly polarized emission, and it could be shown that the emission polarization depends on the orientation of the fiber within the sample. Rotation of the excitation light polarization resulted in the excitation of a different subset of molecules. However, the dependency of emission polarization on the orientation of the Pt-fiber was still visible.

Orientation measurements were then carried out on a single molecule level. In single molecule measurements the emission polarization is not influenced by the polarization of the excitation light as only a single molecule with a fixed dipole moment contributes to the signal. To measure relative orientations of multiple fluorophores, bleaching experiments were carried out. The fluorescence intensity of streptavidin labeled with up to four Atto 565 molecules was recorded upon constant illumination over an extended time. Fluorescent molecules were then subsequently bleached and the orientation of single molecules calculated. However, we show that the orientation measurements are hampered by FRET between multiple fluorophores and relative orientations can only be calculated if the FRET efficiency is known.

To circumvent the influence of FRET on the measurements, we propose fluorescence excitation on the red edge of the excitation spectrum of the fluorophores. Red edge excitation eliminates FRET [104] allowing for the calculation of the proper relative orientations. Using an alternating excitation scheme with an excitation wavelength close to the maximum absorption of the fluorophore and an excitation wavelength at the red-edge of the absorption spectrum the presence of homo-FRET on a single molecule level could possibly be detected and eliminated.

6

Application to super-resolution by localization microscopy

Super-resolution localization microscopy methods, such as PALM and STORM, use the sparse fluorescence of single molecules in an active state to determine their positions with an accuracy exceeding the diffraction limit of light. Repeated switching of different molecules to the on-state and localization of each molecule is then used to construct a super-resolved image. Single fluorescent molecules are optimally excited when their absorption dipole moment is aligned with the polarization direction of the excitation light. This can bias anisotropy and orientation measurements of non-randomly distributed molecules.

This chapter will discuss the influence of photo-selection on standard PALM measurements and possible excitation schemes to reduce any bias by non-randomly oriented molecules.

6.1 Materials and Methods

6.1.1 Acquisition of microscopy data

Photobleaching of one polarization component

The sample was excited and activated first in TIRF with the evanescent field of the activation and excitation light polarized in-plane using an s-polarized incident beam. For this, the polarization of the activation was aligned to the polarization of the excitation light. Differences in the polarization state of the two lasers are reduced by a linear polarizer (11 in Figure 3.1). A non optimal alignment of the polarization direction of the two lasers leads therefore to a reduction of the laser power, but does not change the polarization direction of the laser light.

The sample was activated and excited continuously. The excitation at 568 nm was kept constant at 30 mW (measured at the backfocal plane of the microscope). The activation at 405 nm was set to 20 µW to activate only a sparse subset of molecules. The activation power was increased during measurements to keep the activation rate of molecules constant. Imaging was carried on until no further molecules appeared upon activation at high activation powers of 10 mW. Then the activation and excitation of molecules was paused for ten minutes, to allow molecules in a long lived dark state to return to the ground state. Imaging was then carried out for another 4000 frames. If no significant increase in activation of molecules was visible after resuming the imaging, the polarization of the incidence light was rotated by 90°. The rotation of the polarization from s- to p-polarized light results in a change of the evanescent field polarization from in-plane polarization to a mainly z-polarized activation and excitation field. Imaging was carried on until no further fluorophores appeared.

Standard PALM measurements

The initial polarization of the evanescent field was set to a mainly z-polarized field. A set of 32000 images was acquired which resulted in approximately 700000 localizations. After imaging the 32000 frames the polarization was

rotated by 90° to purely in-plane linear polarization. Another 32000 frames were recorded which again resulted in approximately 700000 localizations. The sample was excited with laser light at 568 nm and the intensity was kept constant at 30 mW (measured at the backfocal plane of the microscope). The activation at 405 nm was set to 20 µW and kept constant throughout the measurement.

Anisotropy/orientation measurements

Experiments were carried out on the setup described before, no further changes are necessary. Essentially, the data acquired for investigating the influence of photo-selection on super-resolution by localization measurements can be used to calculate anisotropy and orientation values for single molecules.

The sample was excited and activated first in TIRF with the evanescent field of the activation and excitation light polarized out-of-plane using p-polarized incident beams. During the measurements the sample was activated continuously and read out with 568 nm excitation in parallel.

6.1.2 Sample preparation

REF52 cells were seeded in two well LabTek chambers (Nunc, Germany) and incubated at 37°C and 5% CO_2 for 48h. The cells were transiently transfected with mEos2-actin using Lipofectamine 2000 (Invitrogen, USA) at 95% confluency. After overnight expression cells were fixed with 3% PFA (EMS) for 30 minutes. The medium was then replaced with PBS.

Neuro2a cells were seeded in MatTek dishes (Nunc, Germany) and incubated over night at at 37°C and 5% CO_2. The cells were then transfected with mEos-β-actin and RacQ61L using X-treme-Gene 9 transfection reagent (PAN Biotech GmbH, Germany) and incubated for further 24 hours. Cells were then fixed with PFA and washed.

6.1.3 Data analysis

Data analysis was performed with rapidSTORM [117]. The rapidSTORM algorithm starts by finding maxima in a noise reduced image [116]. Fluorophore positions are then determined by nonlinear least squares fitting. Only fluorophores emitting at least 200 photons were fitted. The lower limit was set to 200 photons as a single photoswitchable fluorescent protein is reported to emit around 500 photons on average [92]. Split equally into two channels this results in 250 photons per channel. Positions determined by rapidSTORM were saved and then analyzed further using custom written MATLAB scripts.

To determine the anisotropies and orientations of single molecules the intensity values at the positions of single molecules were read out of the image data. This was done by addressing each localization and selecting a region of interest around each molecule in the spatially matched channels. The region of interest was chosen to be a box of 3 pixels in each direction corresponding to a square with an edge length of 300 nm in the sample space. Each region of interest was then background corrected and in case of the perpendicular channel multiplied by a previously determined G-factor. Background correction was done by selecting four squares of 4-by-4 pixels next to the region of interest of the molecule. The standard deviation of each of the four squares was calculated. The region of interest with the smallest standard deviation is most likely not hampered by the fluorescence signal. The mean value of this region of interest was then calculated and subtracted from each pixel of the fluorescence signal. The sum intensity of the fluorescence signal was than determined in each region of interest. Anisotropy values were then calculated according to equation (2.21).

Anisotropy on a single molecule level becomes a measure of orientation and the measured intensities in the parallel and perpendicular channel can be used to calculate molecular orientations in a 2d-plane as described in the previous chapter.

6.2 Photoactivated localization microscopy

Conventional light microscopy is limited due to the diffraction of light to a resolution of approximately half the wavelength of the light used for imaging [56]. In fluorescence microscopy this limit is given by the emission wavelength of the fluorophores. To bypass this limit PALM microscopy makes use of photoactivatable or photoswitchable fluorescent proteins. By switching a small subset of fluorophores to an on-state only a few molecules will fluoresce during an imaging cycle and the mean distance between each fluorescent molecule will be much larger than the diffraction limit of light. The position of a single molecule can then be determined with an accuracy much higher than the diffraction limit. By sequentially switching and imaging all molecules the position of every molecule can be determined and a super-resolved image can be generated out of the measured positions. Figure 6.1(a) shows the image of mEOS-actin generated by summing all images of a PALM-stack which is equivalent to a standard widefield image. Figure 6.1(b) shows the superresolution image where the localization of each molecule is represented as a single pixel of 10 nm in size.

The localization precision for each molecule can be calculated according to equation (2.15). The distribution of the localization precision is shown in Figure 6.3. It has to be noted, that equation 2.15 only gives a theoretical lower limit for the localization precision of a single fluorophore taking into account only the camera dark noise. Generally, measurements in cells are hampered by higher noise levels due to autofluorescence of the cells[119, 118]. The measured localization precision of $x = 20$ nm $\pm$ 7 nm exceeds the resolution limit given by equation (2.13) of 250 nm ($\lambda = 595$ nm, NA = 1.45) by a factor of 12.5. However, as described in chapter 2.2.2 the localization precision cannot be directly compared to the resolution limit in conventional light microscopy. The labeling density and the spatial distribution of the fluorescent molecules has to be taken into account, making the localization precision not suitable as a resolution measure in localization microscopy [90].

Standard PALM measurements do not take into account the molecule orientation. Activation and excitation of molecules depend on their axial po-

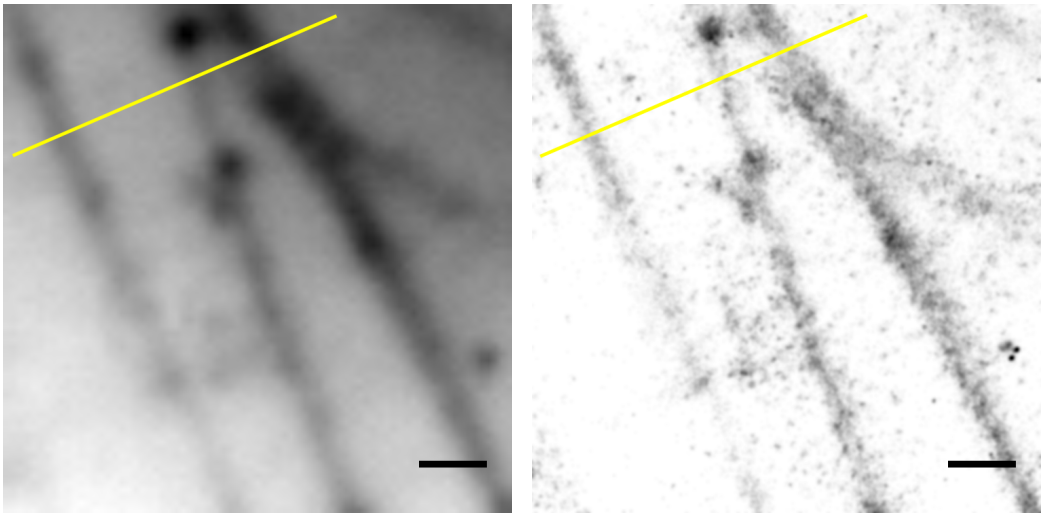

(a) (b)

Figure 6.1: Actin filaments labeled with mEos2. (a) Diffraction limited wide field image generated by summing a series of 24000 images of a PALM-stack. (b) Corresponding PALM image. Note that for better visibility an inverted look up table is used. Scale bar is 1 µm. Profiles along the marked yellow lines are shown in Figure 6.2.

sitions and on their orientations relative to the polarization of the excitation light and thus the imaging probability of molecules varies from molecule to molecule, hampering localization based measurements in TIRF. So far, polarization in photoactivated localization microscopy was only investigated in conventional wide field excitation [47]. The unique properties of the polarization state of the evanescent field in total internal reflection microscopy allow the generation of an excitation field with an arbitrary polarization state, including polarization components along the optical axis. At the same time the low penetration depth of the evanescent field in TIRF microscopy is ideally suited for investigating plasma membrane proteins.

6.3 Polarized excitation

In the previous chapter we have seen that the Pt-complex emits polarized light and that the polarization of the emission light depends on the polariza-

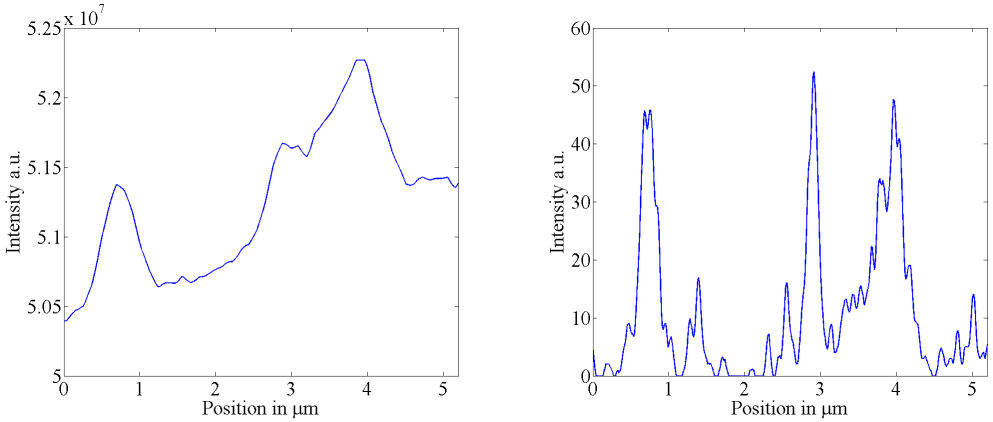

(a) (b)

Figure 6.2: Intensity profile of Actin filaments of Figure 6.1 . (a) Intensity profile of wide field image generated by summing a series PALM-stacks. (b) Intensity profile of the corresponding PALM image.

tion of the excitation light, suggesting that different molecules contribute to the emission signal depending on their orientation relative to the polarization of the excitation light.

Photoactivated localization microscopy is a single molecule technique where molecules are activated and excited by the irradiation with light of two different wavelengths. In each step, activation and excitation, light is absorbed and each molecule undergoes photo-selection. Therefore, the alignment of the transition dipole moments of the molecules with the polarization of the activation and excitation light has to be considered.

To investigate the effect of photo-selection on standard PALM measurements two different experiments are carried out:

1. The sample is imaged with y-polarized light for a fixed number of images. Before the sample is bleached the polarization is rotated to z polarization.

2. The sample is bleached with y-polarized light. The sample is imaged with z-polarized light afterwards.

To measure the effect of the excitation polarization on a standard PALM measurement a sample which is typically used for super-resolution imaging

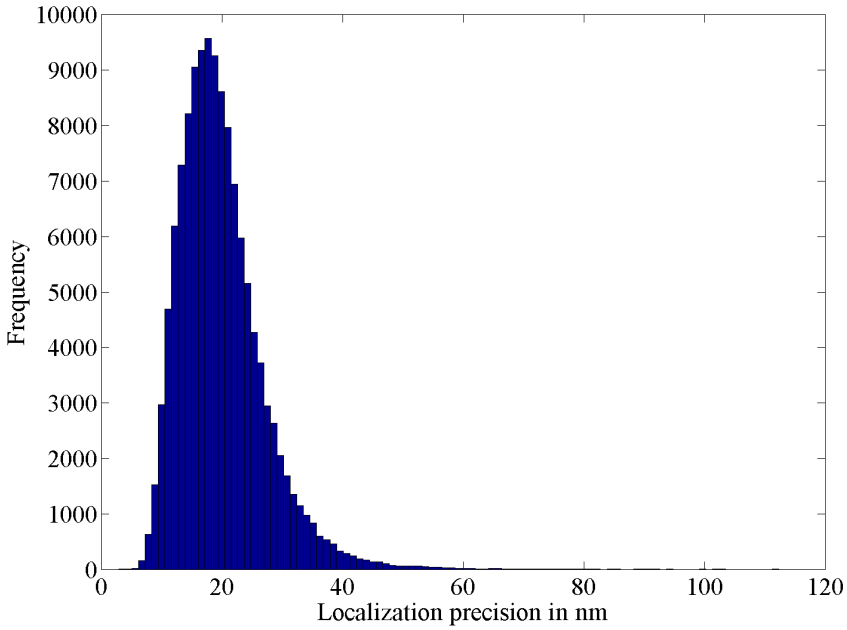

Figure 6.3: Distribution of the localization precision found for each localization of Figure 6.1(b).

has been chosen. Actin is often used as a sample for super-resolution imaging as it shows a clear structure where the increased resolution offers the possibility to separate nearby filaments [23, 64]. At the same time actin filaments labeled with organic dyes have been shown to exert strong fluorescence anisotropy [75].

6.3.1 Standard PALM measurements

PALM and STORM images are usually taken without completely bleaching the sample. Measurements are carried out until the structures of interest are visible and resolved. To test standard PALM measurements for the dependency on the excitation light polarization, a PALM image is taken with one polarization direction. The excitation polarization is rotated by 90° after the acquisition of a sufficient number of frames to reconstruct a super-resolution image.

Figure 6.4(a) shows the reconstructed image of mEos2-actin after imaging

for 32000 frames with mainly z-polarized excitation light. Figure 6.4(b) shows the same sample excited with purely in plane (y) polarized excitation light.

No clear differences are visible, suggesting that the excitation with different polarization components will not qualitatively affect the measurement. However, PALM measurements can also be carried out until all fluorescent molecules are bleached. Using polarized excitation light then might lead to bleaching of one sub-population of molecules.

6.3.2 Photobleaching of one polarization component

Figure 6.5(a) shows the reconstructed PALM image of a mEos2-actin sample recorded with in-plane polarized excitation light. The reconstruction is made out of a short image sequence of 2000 frames. The sample was imaged for further 104000 frames until no fluorophores appeared upon activation and excitation. The polarization was then rotated to light polarized along the optical axis of the microscope. Figure 6.5(b) shows the same cell excited with out of plane polarization. Even though the sample was bleached completely with in plane polarized excitation light, there are still fluorescence molecules left which could be activated and imaged using z-polarized excitation light.

This suggests that polarized excitation and activation in PALM measurements lead to an activation and excitation of only a subset of molecules. However, this effect can hardly be detected in conventional PALM imaging. To further investigate the effect of photo-selection on PALM measurements it is necessary to measure the emission polarization of single molecules.

6.4 Polarized emission

The measurement of the fluorescence signal in the parallel and perpendicular channels allows us to calculate anisotropy values for single molecules [46] and also to investigate the influence of photo-selection on these measurements.

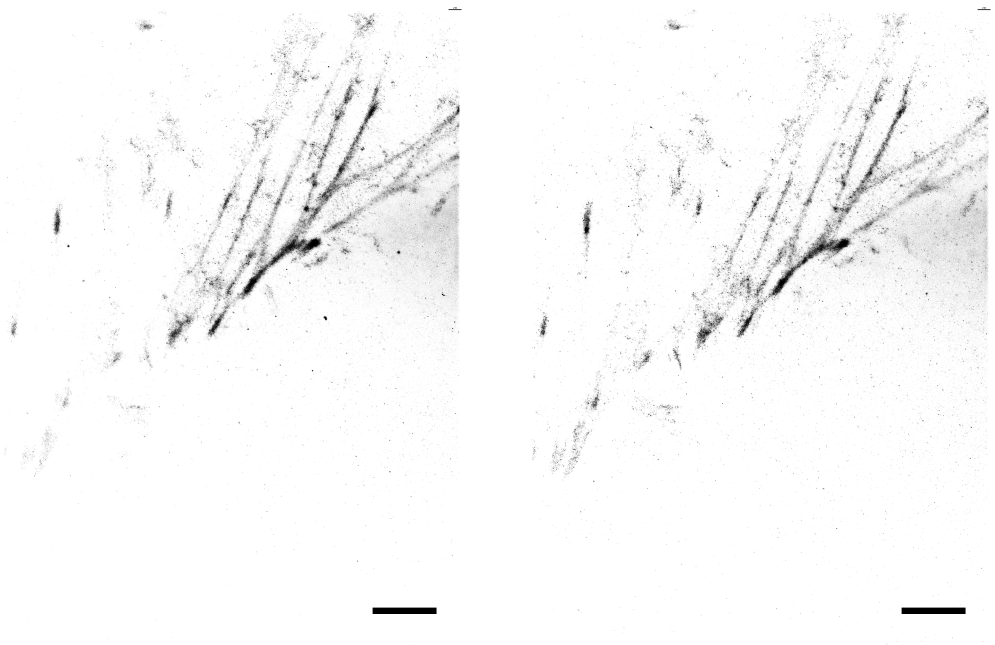

(a) z-polarization with small x-component

(b) In-plane polarization of excitation light along y-direction.

Figure 6.4: A mEos2-actin sample imaged with excitation light polarization oriented along the optical axis (z) of the microscope and in-plane polarized excitation light. The sum of the perpendicular and parallel channel are shown here. Scale bars are 5 µm. Note that for better visibility an inverted gray scale look up table is used.

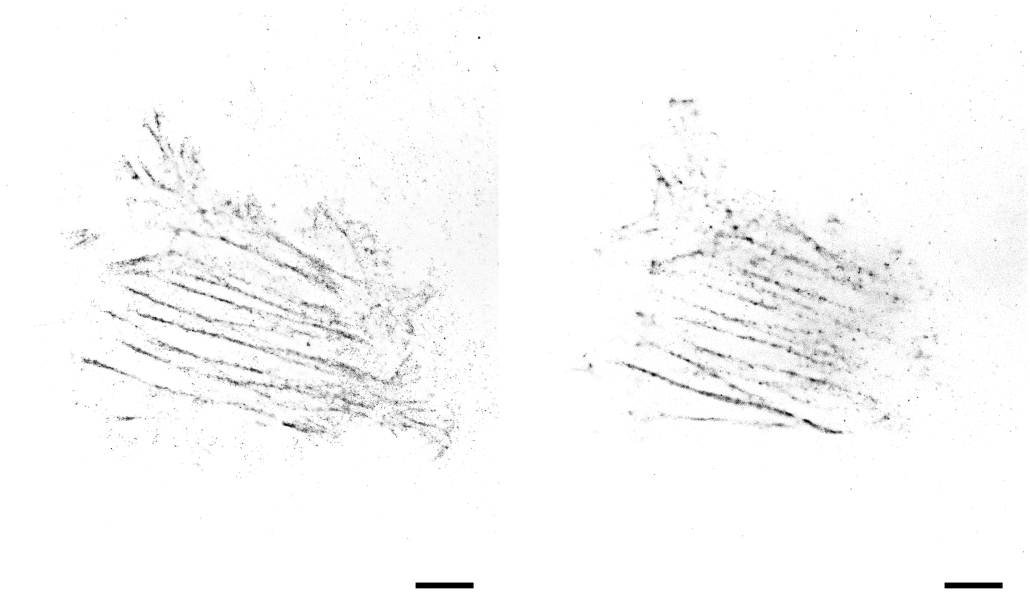

(a) In-plane polarization of excitation light along y-direction.

(b) z-polarization with small x-component

Figure 6.5: A mEos2-actin sample imaged with in-plane polarized excitation light and excitation light oriented along the optical axis (z) of the microscope. The sum of the perpendicular and parallel channels were analyzed. Scale bars are 5 µm.

6.4.1 Orientation measurements in photoactivated localization microscopy

Figure 6.6 shows the anisotropy image of a PALM measurement of mEos2-actin measured for 2000 frames. The image was recorded with the polarization of the TIRF being linearly polarized in the sample plane (y-direction). The inset shows the distribution of measured anisotropies. The anisotropy histogram is skewed with a maximum at $r_{max} = 0.6$ and is in agreement with measured anisotropy distributions known from literature [46]. Maxima at the very edges of the distribution might result from the overlay of the parallel and perpendicular channels during the calculation the fluorescence anisotropy and the translation of one channel to match the other one.

To further investigate the effect of photo-selection on polarized PALM

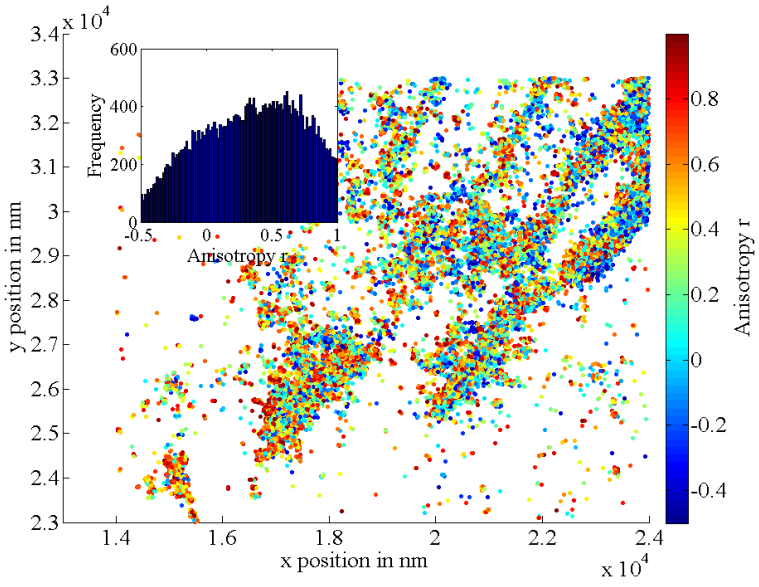

Figure 6.6: Anisotropy measurements in PALM of mEOS2-actin. The inset shows the anisotropy distribution for mEos2-actin

measurements the polarization of the TIRF field is rotated to z-polarized light. However, for the measurement with z-polarized incident light anisotropy is not well suited, as it makes the alignment of the detection polarizers with the excitation polarization necessary. For obvious reasons this is not possible, for a TIRF field which is polarized along the optical axis. Therefore, the 2d-orientation of single molecules is preferred over anisotropy measurements.

Figure 6.7 shows the distribution of 2d molecular orientations for y-polarized excitation light. The distribution is skewed with a maximum at $\Theta = 30°$. The skewed distribution is a strong hint for a non-random distribution of excited molecules.

In any distribution of molecules, photo-selection leads to preferred excitation of molecules with a dipole moment aligned parallel with the excitation light. For a random distribution the measured orientations are equally distributed around the preferred excitation axis resulting in a symmetric distribution. However, for a non-random distribution the measured histogram will be skewed as the number of orientations is not equally distributed around

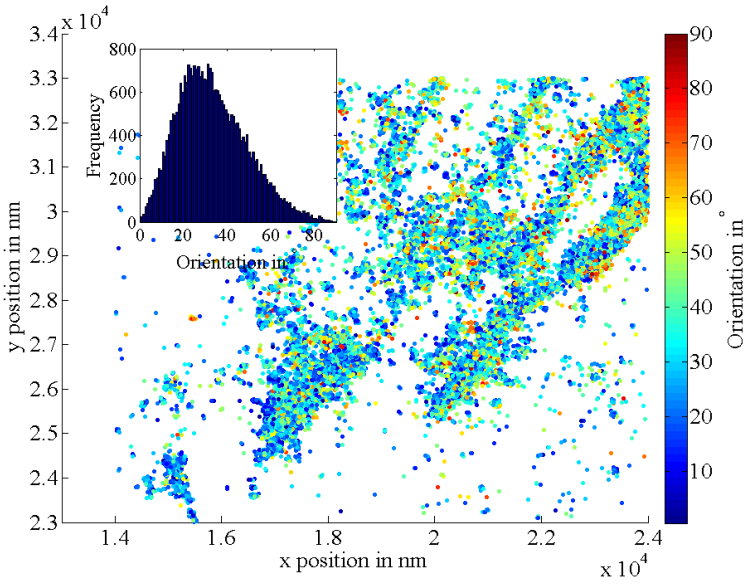

Figure 6.7: Orientation measurements in PALM with an in-plane polarized (y-direction) TIRF-field. The figure shows the 2d orientation of the molecules. The inset shows the distribution of molecule orientations.

the preferred excitation axis.

Figure 6.8 shows the orientation PALM image for the TIRF-field being polarized along the optical axis. The distribution of molecular orientations is skewed, however the maximum of the distribution can now be found around $\Theta = 55°$.

The skewing of the orientation distribution suggests again a non-random distribution of excited molecules. However, the shift of the maxima in the distributions from in-plane to out-of-plane polarized excitation suggests that a different subset of molecules is excited by this polarization state.

In a further experiment Neuro2a cells stimulated with RacQ61L were used. These cells contain clearly separated actin structures of defined orientations. Figure 6.9(a) shows a wide field image of such a cell. This cell contains filopodia at the cell periphery that are perpendicularly oriented to the leading edge of the cell. Internal arcs are visible that are parallel to the leading edge. In the lamellipodium a mixture of orientations is visible.

Figure 6.9(b) shows the corresponding PALM image with the molecule

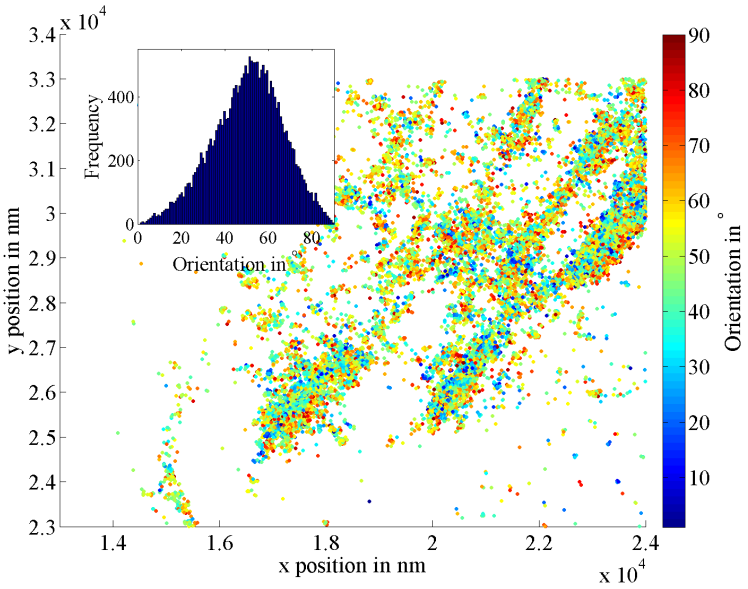

Figure 6.8: Orientation measurements in PALM with an out-of-plane polarized (z-direction) TIRF-field. The figure shows the 2d orientation of the molecules. The inset shows the distribution of molecule orientations.

orientations being color encoded. The excitation light was chosen to be polarized along the optical axis, so that no preferential excitation in the imaged xy-plane would occur. The differently oriented actin filaments show no clear difference in the molecule orientations. A histogram of the molecule orientations (Figure 6.10) shows a distribution centered at 45°. The peak at 45° could result from the averaging over all molecules. However, the PALM image shows no differences in the orientations of single molecules from differently oriented actin filaments making the determined histogram unlikely to suffer from averaging effects over the whole field of view. More likely is an averaging effect for each single molecule, assuming that the fluorescent protein is not fused rigidly to actin this might result in a wobbling of the fluorescent molecule. Such a flexible link between the fluorescent molecule and the molecule of interest will prevent a measure of orientation which can be directly related to the orientation of actin molecules within actin filaments.

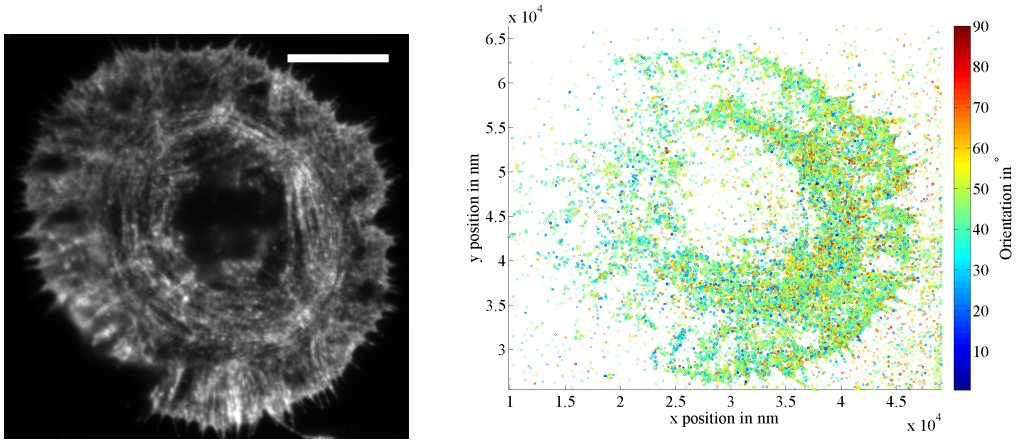

(a) Conventional TIRF image. (b) Orientation measurement in PALM

Figure 6.9: Neuro2a-cell with mEos2-β-actin imaged in conventional (a) TIRF and (b) super resolution microscopy. (b) shows the molecule orientations encoded by color. Please note that the left side of the cell is slightly out of focus. This leads to less localizations found in this area. The scale bar in (a) is 5 µm.

6.5 Conclusion

This chapter discusses the capability of deducing molecule orientations in super-resolution by localization microscopy and discusses the influence of the excitation light polarization on such measurements.

PALM images were taken with different polarization states of the TIRF field. It could be shown that even after bleaching with one polarization state a small fraction of fluorophores could still be activated and excited with the excitation polarization rotated by 90°. Then, a typical PALM image was acquired with two different polarization states. Minor differences were visible for the two different excitation polarization states, therefore showing the influence of photo-selection on PALM imaging.

Photo-selection of fluorophores in super-resolution by localization microscopy is of special interest, as these microscopy techniques are essentially single molecule imaging techniques which aim for quantitative microscopy. In its simplest form this would be counting of single fluorescent molecules, which can be hampered by photo-selection.

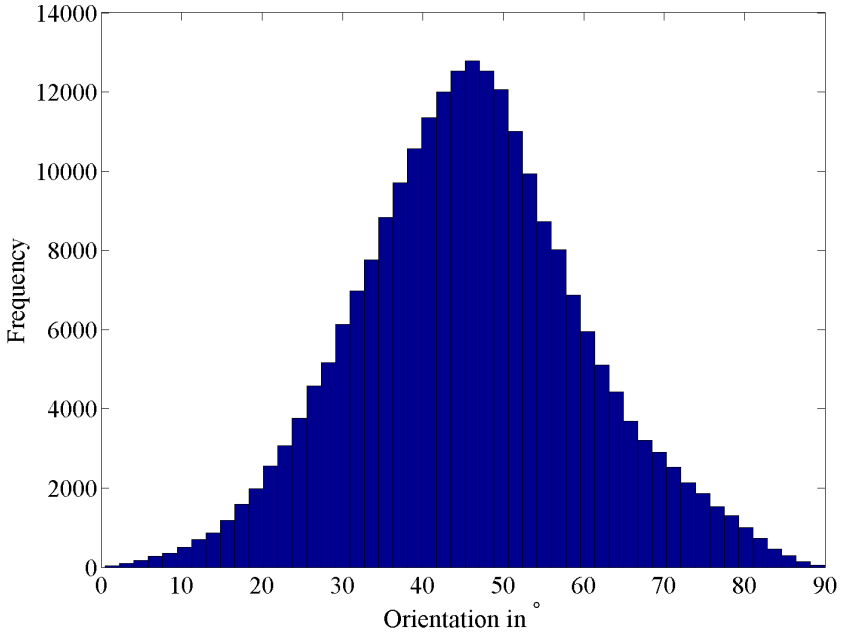

Figure 6.10: Histogram of molecule orientations in Figure 6.9(b).

To further investigate the influence of the excitation light polarization on the imaged molecules, the polarized emission of single fluorophores was used to determine anisotropy values and molecule orientations. First, molecular anisotropies were measured. However, to infer the excitation polarization the measure of anisotropy is not suited well. In anisotropy measurements the emission polarization has to be aligned with the excitation polarization, which is not possible for a polarization state along the optical axis of a microscope. Anisotropy is well suited as a measure of depolarization of the fluorescence emission of an ensemble of molecules. Therefore, orientation measurements were used to infer the influence of photo-selection on single molecules. It could be shown, that a non-random distribution of fluorophores can result in a biased distribution of orientations. If one would like to circumvent this bias, the z-polarization of a TIRF field can be used.

To eliminate any biased excitation in TIRF it is necessary to generate a TIRF field with polarization components in x-,y- and z direction. A TIRF field with at least two major excitation components can be generated by

using circularly polarized excitation light or linear excitation light polarized at 45° thus using a composition of s- and p-polarized incident light. To introduce a third polarization component two circularly polarized excitation beams can be used. These beams could be moved to different positions in the backfocal plane of the microscope and generate all three polarization components. Also, a movement of the excitation beam along a circle in the backfocal plane with circularly polarized light, a temporal sampling of all polarization states, is possible.

7

Conclusion and outlook

7.1 Conclusion

We have developed a microscopy system that is capable of measuring fluorescence anisotropy in ensemble measurements as well as on a single molecule level in total internal reflection fluorescence (TIRF) microscopy. TIRF allows a high selectivity in the axial direction due to its low penetration depth and greatly reduces background fluorescence from out of focus signals [13]. Therefore TIRF microscopy is optimally suited for investigating the basal plasma membrane of cells.

To control the polarization of the evanescent field a commercially available microscope body was extended by coupling three lasers equipped with a half wave plate to the microscope. The polarization of each laser was aligned with respect to each other and the polarization axis of the three lasers was rotated to achieve a purely in-plane linear polarization or an out-of-plane polarization of the evanescent field within the sample space.

On the emission side the microscope was extended by a home built image splitter, splitting the emission light into parallel and perpendicular polarized light with respect to the excitation beam. The system was equipped with an EM-CCD camera sensitive enough to image single fluorescent molecules. However, it was shown that the used EM-CCD camera is not optimally suited for ensemble measurements as it shows smearing. Anisotropy measurements

are sensitive to small changes of the background and are therefore hampered by the smearing of the EM-CCD camera.

Measurements of a fluorescence anisotropy standard in conventional wide field illumination validated the proper functionality of the microscope. Measurements of cells transfected with a fluorescent protein in the cytosol in TIRF gave identical results as in conventional wide field illumination, validating the performance of the system in TIRF.

However, the measurements of the fluorescence anisotropy standard highlighted a known drawback of anisotropy measurements using high numerical aperture objectives: High NA objectives lead to a reduction of measured anisotropy values due to mixing of polarization components [96]. This leads to a reduction of the dynamical range in fluorescence anisotropy measurements with high NA-objectives.

As a biological application for ensemble measurements, the small GTPase Ras was investigated. Both conventional far field illumination and TIRF measurements were performed on HRas, KRas and their constitutively active mutants HRas-G12V and KRas-G12V as well as their membrane anchors tK and tH. The high standard deviations of the measurements prevent a clear conclusion about the spatial organization of the observed Ras variants. However, the anisotropy distributions measured in TIRF show less skewing than measurements in conventional wide field microscopy. Standard deviations are comparable in both microscopy techniques for membrane proteins, the anisotropy of cytosolic Citrine shows lower standard deviations for conventional wide field illumination. This is expected as the intensity of cytosolic fluorophores is much smaller on the plasma membrane as in the cytosol leading to higher signal to noise levels in far field excitation than in TIRF microscopy.

On a single molecule level anisotropy becomes a measure of orientation [54]. The capability of imaging orientations by polarization measurements was shown by imaging a Platinum(II)-complex [105]. Imaging of single Atto565 molecules bound to streptavidin was shown. It was shown that with the present setup it is possible to visualize homoFRET on a single molecule level. To our knowledge single molecule homoFRET has not been shown before.

Then localization microscopy measurements on actin were carried out. It was shown that the microscope localization precision exceeds the diffraction limit of light. Polarization measurements in PALM were carried out for the first time in TIRF microscopy. The results are in good agreement with [47]. The excitation polarization was then changed from purely linear in-plane polarization to out-of-plane polarization resulting in an evanescent field which is polarized mainly along the optical axis. It could be shown that photobleaching with one polarization component does not photobleach all molecules. After rotation of the excitation polarization molecules were still activatable and fluorescent. The emission polarization was measured for different polarization states of the excitation field. The emission polarization of a single molecule is a measure of molecule orientations. It was shown that a different subset of molecules is excited after rotating the polarization of the evanescent field.

Super-resolution by localization microscopy measurements are essentially wide field measurements that use conventional far field excitation or the evanescent field in total internal reflection fluorescence microscopy. Usually, the polarization of the excitation is not taken into account in these measurements. However, usually lasers are used as light sources that are linearly polarized resulting in a polarized excitation field. The polarization of the excitation light can bias fluorescence measurements. This is of special interest as single molecule measurements aim for the quantitative analysis of the spatial organization and distribution of molecules [49, 16, 8, 81]. Biasing these measurements by the use of polarized excitation light might lead to false conclusions.

7.2 Outlook

Ensemble measurements

No clear differences were visible in ensemble measurements for the chosen biological applications. This was caused by the large spread of anisotropy distributions. One reason for this might be the use of an EM-CCD camera

that is not optimally suited for anisotropy measurements. The smearing of the EM-CCD camera leads to an increased background, however, ensemble measurements do not require the use of highly sensitive EM-CCD cameras and can be carried out with a camera less prone to inducing background noise.

The setup is also used for single molecule localization experiments that need an effective pixel size of 100 nm therefore the image will be oversampled. Oversampling increases the noise per pixel in ensemble measurements. This is not necessary for ensemble measurements, larger pixel sizes could be used.

Furthermore, the use of a high NA objective lowers the dynamic range of fluorescence anisotropy measurements. An objective type TIRF setup was chosen due to accessibility of the sample and ease of use, however this setup makes use of a high NA objective. In principle a prism type TIRF setup could be used with a low NA objective. In an objective type TIRF setup the NA could also be artificially reduced on the emission side by placing a pinhole in the Fourier plane of the image. The pinhole would act as a low pass and block high spatial frequency components, thus reducing the NA of the objective.

Single molecule measurements

It was shown that the polarization can be used to determine molecular orientations. However, when two molecules are in close vicinity FRET can occur. In the presence of FRET the FRET efficiency has to be known to calculate the relative orientation of two molecules. To suppress FRET, fluorescence could be excited at the red-edge of the absorption spectrum of a fluorophore, thereby reducing the spectral overlap of donor and acceptor molecule. We propose an alternating excitation at the absorption maximum and at the red-edge of the absorption spectrum of the fluorophores in use. While excitation at the absorption maximum will be hampered by homoFRET the excitation at the red-edge will not show any FRET [104]. Two time traces can then be recorded, differences in these time traces are then caused by the presence of FRET. The measurement will then allow the direct observation of ho-

moFRET, calculation of the homoFRET efficiency on a single molecule level and calculation of the relative orientation of multiple fluorophores. However, excitation at the red edge of the absorption spectrum is only possible with increased laser powers. It remains to be investigated if this is applicable to single molecule measurements in live cells.

Polarized PALM measurements

A biasing effect of polarized excitation in PALM measurements was shown. To circumvent this bias circularly polarized light should be used. However, generation of circular polarized light in TIRF measurements is not straight forward [101]. A possible excitation scheme would involve two laser beams positioned at two points in the backfocal plane of the microscope objective. The z-component of the evanescent field would then have to be adjusted to match the x- and y-components. To efficiently excite at least two polarization components, it is sufficient to use either one circularly polarized excitation beam or one linearly polarized excitation beam at 45° incident angle.

On the detection side the use of a high NA-objective leads to a mixing of polarization components. This could be reduced by using a pinhole in the Fourier plane of the microscope. A setup presented by Hohlbein et al. [61] can be used to determine 3d orientations of single molecules. This scheme adds another channel to the setup, where the rim beams are imaged. However, this type of setup was so far only used in point measurements. Wide field measurement have not been carried out yet.

References

[1] Abbe, E. Beiträge zur Theorie des Mikroskops und der Mikroskopischen Wahrnehmung. *Archiv für mikroskopische Anatomie. 9* (1873).

[2] Accorsi, G., Listorti, A., Yoosaf, K., and Armaroli, N. 1,10-Phenanthrolines: Versatile Building Blocks for Luminescent Molecules, Materials and Metal Complexes. *Chemical Society Reviews 38*, 6 (June 2009), 1690–700.

[3] Alberts, B., Johnson, A., Lewis, J., Raff, M., Roberts, K., and Walter, P. *Molecular Biology of the Cell, Fourth Edition*. Garland Science, 2002.

[4] Albrecht, A. C. Polarizations and assignments of transitions: The method of photoselection. *Journal of Molecular Spectroscopy 6* (Jan. 1961), 84–108.

[5] Ambrose, E. A surface contact microscope for the study of cell movements. *Nature* (1956).

[6] Ameloot, M., VandeVen, M., Acuña, A. U., and Valeur, B. Fluorescence anisotropy measurements in solution: Methods and reference materials (IUPAC Technical Report). *Pure and Applied Chemistry 85*, 3 (2013), 589–608.

[7] Annibale, P., Vanni, S., Scarselli, M., Rothlisberger, U., and Radenovic, A. Identification of clustering artifacts in photoactivated localization microscopy. *Nature Methods 8*, 7 (July 2011), 527–8.

[8] Annibale, P., Vanni, S., Scarselli, M., Rothlisberger, U., and Radenovic, A. Quantitative photo activated localization microscopy: unraveling the effects of photoblinking. *PloS One 6*, 7 (Jan. 2011), e22678.

[9] Axelrod, D. Carbocyanine dye orientation in red cell membrane studied by microscopic fluorescence polarization. *Biophysical Journal 26*, 3 (June 1979), 557–73.

[10] Axelrod, D. Fluorescence polarization microscopy. *Methods in Cell Biology Vol. 30 30* (1989), 333–352.

[11] Axelrod, D. Total Internal Reflection Fluorescence Microscopy in Cell Biology. *Traffic 2*, 11 (Nov. 2001), 764–774.

[12] Axelrod, D. Total internal reflection fluorescence microscopy in cell biology. *Methods in Enzymology 361*, 1996 (Jan. 2003), 1–33.

[13] Axelrod, D., and Burghardt, T. P. Total internal reflection fluorescence. *Annual Review of Biophysics and Bioengineering*, 13 (1984), 247–268.

[14] Axelrod, D., Hellen, E., and Fulbright, R. Total internal reflection fluorescence. In *Topics in Fluorescence Spectroscopy Vol. 3*, J. R. Lakowicz, Ed. Plenum Press, New York, 1992, ch. Total inte, p. 408.

[15] Axelrod, D., and Omann, G. M. Combinatorial microscopy. *Nature Reviews Molecular Cell Biology 7*, 12 (Dec. 2006), 944–52.

[16] Baddeley, D., Jayasinghe, I. D., Lam, L., Rossberger, S., Cannell, M. B., and Soeller, C. Optical single-channel resolution imaging of the ryanodine receptor distribution in rat cardiac myocytes. *Proceedings of the National Academy of Sciences of the United States of America 106*, 52 (Dec. 2009), 22275–80.

[17] Bader, A. N., Hoetzl, S., Hofman, E. G., Voortman, J., van Bergen en Henegouwen, P. M. P., van Meer, G., and Gerritsen, H. C. Homo-FRET imaging as a tool to quantify protein and lipid clustering. *Chemphyschem : A European Journal of Chemical Physics and Physical Chemistry 12*, 3 (Feb. 2011), 475–83.

[18] Bader, A. N., Hofman, E. G., van Bergen En Henegouwen, P. M. P., and Gerritsen, H. C. Imaging of protein cluster sizes by means of confocal time-gated fluorescence anisotropy microscopy. *Optics Express 15*, 11 (May 2007), 6934–45.

[19] Bader, A. N., Hofman, E. G., Voortman, J., en Henegouwen, P. M. P. V. B., and Gerritsen, H. C. Homo-FRET imaging enables quantification of protein cluster sizes with subcellular resolution. *Biophysical Journal 97*, 9 (Nov. 2009), 2613–22.

[20] Bahlmann, K., and Hell, S. W. Depolarization by high aperture focusing. *Applied Physics Letters 77*, 5 (2000), 612.

[21] Bates, M., Huang, B., Dempsey, G. T., and Zhuang, X. Multicolor super-resolution imaging with photo-switchable fluorescent probes. *Science (New York, N.Y.) 317*, 5845 (Sept. 2007), 1749–53.

[22] Beausang, J. F., Shroder, D. Y., Nelson, P. C., and Goldman, Y. E. Tilting and wobble of myosin V by high-speed single-molecule polarized fluorescence microscopy. *Biophysical Journal 104*, 6 (Mar. 2013), 1263–73.

[23] Betzig, E., Patterson, G. H., Sougrat, R., Lindwasser, O. W., Olenych, S., Bonifacino, J. S., Davidson, M. W., Lippincott-Schwartz, J., and Hess, H. F. Imaging intracellular fluorescent proteins at nanometer resolution. *Science 313*, 5793 (Sept. 2006), 1642–5.

[24] Blum, C., and Subramaniam, V. Single-molecule spectroscopy of fluorescent proteins. *Analytical and Bioanalytical Chemistry 393*, 2 (Jan. 2009), 527–41.

[25] Böhmer, M., and Enderlein, J. Orientation imaging of single molecules by wide-field epifluorescence microscopy. *JOSA B 20*, 3 (2003), 554–559.

[26] Born, M., and Wolf, E. *Principles of Optics*, 7 ed. Cambridge University Press, Cambridge, 1999.

[27] Bourgeois, D., and Adam, V. Reversible photoswitching in fluorescent proteins: a mechanistic view. *IUBMB Life 64*, 6 (June 2012), 482–91.

[28] Brasselet, S., Ferrand, P., and Kress, A. Imaging Molecular Order in Cell Membranes by Polarization-Resolved Fluorescence Microscopy. In *Fluorescent Methods to Study Biological Membranes*, Y. Mély and G. Duportail, Eds., no. August 2012. 2013, pp. 311–337.

[29] Chan, F. T. S., Kaminski, C. F., and Kaminski Schierle, G. S. HomoFRET fluorescence anisotropy imaging as a tool to study molecular self-assembly in live cells. *ChemPhysChem : A European Journal of Chemical Physics and Physical Chemistry 12*, 3 (Feb. 2011), 500–9.

[30] Chang, S.-Y., Chen, J.-L., Chi, Y., Cheng, Y.-M., Lee, G.-H., Jiang, C.-M., and Chou, P.-T. Blue-emitting platinum(II) complexes bearing both pyridylpyrazolate chelate and bridging pyrazolate ligands: synthesis, structures, and photophysical properties. *Inorganic chemistry 46*, 26 (Dec. 2007), 11202–12.

[31] Chen, R. Measurements of absolute values in biochemical fluorescence spectroscope. *Nat. Bur. Stand.(Special Pub.) 76*, 6 (1973), 593–606.

[32] Chen, R., and Bowman, R. Fluorescence polarization: measurement with ultraviolet-polarizing filters in a spectrophotofluorometer. *Science* (1965), 729–732.

[33] Churchman, L. S., Okten, Z., Rock, R. S., Dawson, J. F., and Spudich, J. a. Single molecule high-resolution colocalization of Cy3 and Cy5 attached to macromolecules measures intramolecular distances

through time. *Proceedings of the National Academy of Sciences of the United States of America 102*, 5 (Feb. 2005), 1419–23.

[34] Conibear, P. B., and Bagshaw, C. R. A comparison of optical geometries for combined flash photolysis and total internal reflection fluorescence microscopy. *Journal of Microscopy 200*, Pt 3 (Dec. 2000), 218–29.

[35] Dertinger, T., Colyer, R., Iyer, G., Weiss, S., and Enderlein, J. Fast, background-free, 3D super-resolution optical fluctuation imaging (SOFI). *Proceedings of the National Academy of Sciences 106*, 52 (2009), 22287–22292.

[36] Devauges, V., Marquer, C., Lécart, S., Cossec, J.-C., Potier, M.-C., Fort, E., Suhling, K., and Lévêque-Fort, S. Homodimerization of Amyloid Precursor Protein at the Plasma Membrane: A homoFRET Study by Time-Resolved Fluorescence Anisotropy Imaging. *PLoS ONE 7*, 9 (Sept. 2012), e44434.

[37] Develay, S., and Williams, J. a. G. Intramolecular excimers based on rigidly-linked platinum(ii) complexes: intense deep-red triplet luminescence in solution. *Dalton Transactions*, 34 (2008), 4562.

[38] Dickson, R. M., Cubitt, a. B., Tsien, R. Y., and Moerner, W. E. On/off blinking and switching behaviour of single molecules of green fluorescent protein. *Nature 388*, 6640 (July 1997), 355–8.

[39] Dussault, D., and Hoess, P. Noise performance comparison of ICCD with CCD and EMCCD cameras. In *Infrared Systems and Photoelectronic Technology* (Oct. 2004), E. L. Dereniak, R. E. Sampson, and C. B. Johnson, Eds., vol. 5563, pp. 195–204.

[40] Finan, K., Flottmann, B., and Heilemann, M. *Nanoimaging*, vol. 950. Humana Press, Totowa, NJ, 2013.

[41] Fiolka, R., Belyaev, Y., Ewers, H., and Stemmer, A. Even Illumination in Total Internal Reflection Fluorescence Microscopy Using

Laser Light. *Microscopy Research and Technique 000*, March (2007), 1–6.

[42] Forkey, J. N., Quinlan, M. E., and Goldman, Y. E. Measurement of single macromolecule orientation by total internal reflection fluorescence polarization microscopy. *Biophysical Journal 89*, 2 (Aug. 2005), 1261–71.

[43] Förster, T. Energiewanderung und Fluoreszenz. *Naturwissenschaften* (1946), 166–175.

[44] Förster, T. Zwischenmolekulare Energiewanderung und Fluoreszenz. *Annalen der Physik 248*, 1938 (1948).

[45] Fourkas, J. T. Rapid determination of the three-dimensional orientation of single molecules. *Optics Letters 26*, 4 (Feb. 2001), 211–3.

[46] Gould, T. J., Gunewardene, M. S., Gudheti, M. V., Verkhusha, V. V., Yin, S.-R., Gosse, J. A., and Hess, S. T. Nanoscale imaging of molecular positions and anisotropies. *Nature Methods 5*, 12 (2008), 1027–1030.

[47] Gould, T. J., Gunewardene, M. S., Gudheti, M. V., Verkhusha, V. V., Yin, S.-R., Gosse, J. a., and Hess, S. T. Nanoscale imaging of molecular positions and anisotropies. *Nature Methods 5*, 12 (Dec. 2008), 1027–30.

[48] Grecco, H. E., and Verveer, P. J. FRET in cell biology: still shining in the age of super-resolution? *Chemphyschem : A European Journal of Chemical Physics and Physical Chemistry 12*, 3 (Feb. 2011), 484–90.

[49] Greenfield, D., McEvoy, A. L., Shroff, H., Crooks, G. E., Wingreen, N. S., Betzig, E., and Liphardt, J. Self-organization of the Escherichia coli chemotaxis network imaged with super-resolution light microscopy. *PLoS Biology 7*, 6 (June 2009), e1000137.

[50] Gustafsson, M. G. Surpassing the lateral resolution limit by a factor of two using structured illumination microscopy. *Journal of Microscopy 198*, Pt 2 (May 2000), 82–7.

[51] Gustafsson, M. G. L. Nonlinear structured-illumination microscopy: wide-field fluorescence imaging with theoretically unlimited resolution. *Proceedings of the National Academy of Sciences of the United States of America 102*, 37 (Sept. 2005), 13081–6.

[52] Ha, T., Enderle, T., Chemla, S., Selvin, R., and Weiss, S. Single Molecule Dynamics Studied by Polarization Modulation. *Physical Review Letters 77*, 19 (Nov. 1996), 3979–3982.

[53] Hancock, J. F., and Parton, R. G. Ras plasma membrane signalling platforms. *The Biochemical Journal 389*, Pt 1 (July 2005), 1–11.

[54] Harms, G., Sonnleitner, M., Schütz, G., Gruber, H., and Schmidt, T. Single-Molecule Anisotropy Imaging. *Biophysical Journal 77*, 5 (Nov. 1999), 2864–2870.

[55] Heilemann, M., van de Linde, S., Schüttpelz, M., Kasper, R., Seefeldt, B., Mukherjee, A., Tinnefeld, P., and Sauer, M. Subdiffraction-resolution fluorescence imaging with conventional fluorescent probes. *Angewandte Chemie (International ed. in English) 47*, 33 (Jan. 2008), 6172–6.

[56] Hell, S. W. Far-field optical nanoscopy. *Science (New York, N.Y.) 316*, 5828 (May 2007), 1153–8.

[57] Hell, S. W. Microscopy and its focal switch. *Nature Methods 6*, 1 (Jan. 2009), 24–32.

[58] Henis, Y. I., Hancock, J. F., and Prior, I. a. Ras acylation, compartmentalization and signaling nanoclusters (Review). *Molecular Membrane Biology 26*, 1 (Jan. 2009), 80–92.

[59] Herschel, J. 'Αμορφωτα No. I. On a Case of Superficial Colour Presented by a Homogeneous Liquid Internally Colourless. *Philosophical Transactions of the Royal Society 135* (Jan. 1845), 143–145.

[60] Hess, S. T., Girirajan, T. P. K., and Mason, M. D. Ultra-high resolution imaging by fluorescence photoactivation localization microscopy. *Biophysical Journal 91*, 11 (Dec. 2006), 4258–72.

[61] Hohlbein, J., and Hubner, C. G. Simple scheme for rapid three-dimensional orientation determination of the emission dipole of single molecules. *Applied Physics Letters 86*, 12 (2005), 121104.

[62] Hohlbein, J., and Hubner, C. G. Three-dimensional orientation determination of the emission dipoles of single molecules: The shot-noise limit. *The Journal of Chemical Physics 129*, 9 (2008), 094703.

[63] Hoyt, L. F. New Table of the Refractive Index of Pure Glycerol at 20C. *Industrial & Engineering Chemistry 26*, 3 (Mar. 1934), 329–332.

[64] Huang, B., Bates, M., and Zhuang, X. Super-resolution fluorescence microscopy. *Annual Review of Biochemistry 78* (Jan. 2009), 993–1016.

[65] Huang, B., Jones, S. A., Brandenburg, B., and Zhuang, X. Whole-cell 3D STORM reveals interactions between cellular structures with nanometer-scale resolution. *Nature Methods 5*, 12 (Dec. 2008), 1047–52.

[66] Huang, B., Wang, W., Bates, M., and Zhuang, X. Three-dimensional super-resolution imaging by stochastic optical reconstruction microscopy. *Science (New York, N.Y.) 319*, 5864 (Feb. 2008), 810–3.

[67] Huang, F., Hartwich, T. M. P., Rivera-Molina, F. E., Lin, Y., Duim, W. C., Long, J. J., Uchil, P. D., Myers, J. R., Baird, M. a., Mothes, W., Davidson, M. W., Toomre, D.,

and Bewersdorf, J. Video-rate nanoscopy using sCMOS camera-specific single-molecule localization algorithms. *Nature Methods*, April (May 2013), 1–9.

[68] Huang, Z.-L., Zhu, H., Long, F., Ma, H., Qin, L., Liu, Y., Ding, J., Zhang, Z., Luo, Q., and Zeng, S. Localization-based super-resolution microscopy with an sCMOS camera. *Optics Express 19*, 20 (Sept. 2011), 19156–68.

[69] Huse, N., Schönle, A., and Hell, S. W. Z-polarized confocal microscopy. *Journal of Biomedical Optics 6*, 3 (July 2001), 273–6.

[70] Jares-Erijman, E. A., and Jovin, T. M. FRET imaging. *Nature Biotechnology 21*, 11 (2003), 1387–1395.

[71] Jost, A., and Heintzmann, R. Superresolution Multidimensional Imaging with Structured Illumination Microscopy. *Annual Review of Materials Research 43*, 1 (July 2013), 261–282.

[72] Juette, M. F., Gould, T. J., Lessard, M. D., Mlodzianoski, M. J., Nagpure, B. S., Bennett, B. T., Hess, S. T., and Bewersdorf, J. Three-dimensional sub-100 nm resolution fluorescence microscopy of thick samples. *Nature Methods 5*, 6 (June 2008), 527–9.

[73] Kanchanawong, P., Shtengel, G., Pasapera, A. M., Ramko, E. B., Davidson, M. W., Hess, H. F., and Waterman, C. M. Nanoscale architecture of integrin-based cell adhesions. *Nature 468*, 7323 (Nov. 2010), 580–4.

[74] Kawski, A. Fluorescence Anisotropy: Theory and Applications of Rotational Depolarization. *Critical Reviews in Analytical Chemistry 23*, 6 (Jan. 1993), 459–529.

[75] Kinosita Jr., K., Itoh, H., Ishiwata, S., Hirano, K., Nishizaka, T., and Hayakawa, T. Dual-view microscopy with a single camera: real-time imaging of molecular orientations and calcium. *The Journal of Cell Biology 115*, 1 (Oct. 1991), 67–73.

[76] Kuhn, J. R., and Pollard, T. D. Real-time measurements of actin filament polymerization by total internal reflection fluorescence microscopy. *Biophysical Journal 88*, 2 (Mar. 2005), 1387–402.

[77] Lakowicz, J. R., Ed. *Principles of Fluorescence Spectroscopy*. Springer US, Boston, MA, 2006.

[78] Lakowicz, J. R., Gryczynski, I., Gryczynski, Z., and Dattelbaum, J. D. Anisotropy-based sensing with reference fluorophores. *Analytical Biochemistry 267*, 2 (Feb. 1999), 397–405.

[79] Lakowicz, J. R., Prendergast, F. G., and Hogen, D. Differential polarized phase fluorometric investigations of diphenylhexatriene in lipid bilayers. Quantitation of hindered depolarizing rotations. *Biochemistry 18*, 3 (Feb. 1979), 508–19.

[80] Lee, S., Oh, J., Kim, D., Kim, S., Lee, J.-B., and Nam, H. G. Polarization-Controlled Photoswitching Resolves Dipole Directions with Subwavelength Resolution. *Physical Review Letters 109*, 24 (Dec. 2012), 248101.

[81] Lee, S.-H., Shin, J. Y., Lee, A., and Bustamante, C. Counting single photoactivatable fluorescent molecules by photoactivated localization microscopy (PALM). *Proceedings of the National Academy of Sciences of the United States of America 109*, 43 (Oct. 2012), 17436–41.

[82] Lidke, K., Rieger, B., Jovin, T., and Heintzmann, R. Superresolution by localization of quantum dots using blinking statistics. *Optics Express 13*, 18 (2005), 1599–1609.

[83] Long, F., Zeng, S., and Huang, Z.-L. Localization-based superresolution microscopy with an sCMOS camera Part II: Experimental methodology for comparing sCMOS with EMCCD cameras. *Optics Express 20*, 16 (July 2012), 17741.

[84] Lord Rayleigh F.R.S. XXXI. Investigations in optics, with special reference to the spectroscope. *Philosophical Magazine Series 5 8*, 49 (1879), 261–274.

[85] Malkusch, S., Endesfelder, U., Mondry, J., Gelléri, M., Verveer, P. J., and Heilemann, M. Coordinate-based colocalization analysis of single-molecule localization microscopy data. *Histochemistry and Cell Biology* (Nov. 2011), 1–10.

[86] Matthews, D. R., Carlin, L. M., Ofo, E., Barber, P. R., Vojnovic, B., Irving, M., Ng, T., and Ameer-Beg, S. M. Time-lapse FRET microscopy using fluorescence anisotropy. *Journal of Microscopy 237*, 1 (Jan. 2010), 51–62.

[87] Mattheyses, A. L., Shaw, K., and Axelrod, D. Effective Elimination of Laser Interference Fringing in Fluorescence Microscopy by Spinning Azimuthal Incidence Angle. *Microscopy Research and Technique 69*, December 2005 (2006), 642–647.

[88] Mattheyses, A. L., Simon, S. M., and Rappoport, J. Z. Imaging with total internal reflection fluorescence microscopy for the cell biologist. *Journal of Cell Science 123*, Pt 21 (Nov. 2010), 3621–8.

[89] Michalet, X., Siegmund, O. H. W., Vallerga, J. V., Jelinsky, P., Millaud, J. E., and Weiss, S. Detectors for single-molecule fluorescence imaging and spectroscopy. *Journal of Modern Optics 54*, 2-3 (Jan. 2007), 239.

[90] Nieuwenhuizen, R. P. J., Lidke, K. a., Bates, M., Puig, D. L., Grünwald, D., Stallinga, S., and Rieger, B. Measuring image resolution in optical nanoscopy. *Nature Methods*, April (Apr. 2013).

[91] Novotny, L., and Hecht, B. *Principles of Nano-Optics*, vol. 60. Cambridge University Press, 2006.

[92] Patterson, G., Davidson, M., Manley, S., and Lippincott-Schwartz, J. Superresolution imaging using single-molecule localization. *Annual Review of Physical Chemistry 61* (Jan. 2010), 345–67.

[93] Pavani, S. R. P., Thompson, M. A., Biteen, J. S., Lord, S. J., Liu, N., Twieg, R. J., Pistun, R., and Moerner, W. E. Three-dimensional, single-molecule fluorescence imaging beyond the diffraction limit by using a double-helix point spread function. *Proceedings of the National Academy of Sciences 106*, 9 (2009), 2995–9.

[94] Prior, I. a., Harding, A., Yan, J., Sluimer, J., Parton, R. G., and Hancock, J. F. GTP-dependent segregation of H-ras from lipid rafts is required for biological activity. *Nature Cell Biology 3*, 4 (Apr. 2001), 368–75.

[95] Quan, T., Zeng, S., and Huang, Z.-L. Localization capability and limitation of electron-multiplying charge-coupled, scientific complementary metal-oxide semiconductor, and charge-coupled devices for superresolution imaging. *Journal of Biomedical Optics 15*, 6 (2010), 066005.

[96] Richards, B., and Wolf, E. Electromagnetic Diffraction in Optical Systems. II. Structure of the Image Field in an Aplanatic System. *Proceedings of the Royal Society A: Mathematical, Physical and Engineering Sciences 253*, 1274 (Dec. 1959), 358–379.

[97] Robbins, M., and Hadwen, B. The noise performance of electron multiplying charge-coupled devices. *IEEE Transactions on Electron Devices 50*, 5 (May 2003), 1227–1232.

[98] Rust, M. J., Bates, M., and Zhuang, X. Sub-diffraction-limit imaging by stochastic optical reconstruction microscopy (STORM). *Nature Methods 3*, 10 (Oct. 2006), 793–5.

[99] Saleh, B. E. A., and Teich, M. C. *Fundamentals of Photonics*, 2 ed., vol. 13. Wiley-Interscience, 2007.

[100] Saurabh, S., Maji, S., and Bruchez, M. P. Evaluation of sCMOS cameras for detection and localization of single Cy5 molecules. *Optics Express 20*, 7 (Mar. 2012), 7338–49.

[101] Schneckenburger, H. Total internal reflection fluorescence microscopy: technical innovations and novel applications. *Current Opinion in Biotechnology 16*, 1 (Feb. 2005), 13–8.

[102] Shannon, C. E. Communication In The Presence Of Noise (Reprint), 1998.

[103] Shtengel, G., Galbraith, J. A., Galbraith, C. G., Lippincott-Schwartz, J., Gillette, J. M., Manley, S., Sougrat, R., Waterman, C. M., Kanchanawong, P., Davidson, M. W., Fetter, R. D., and Hess, H. F. Interferometric fluorescent super-resolution microscopy resolves 3D cellular ultrastructure. *Proceedings of the National Academy of Sciences of the United States of America 106*, 9 (Mar. 2009), 3125–30.

[104] Squire, A., Verveer, P. J., Rocks, O., and Bastiaens, P. I. H. Red-edge anisotropy microscopy enables dynamic imaging of homo-FRET between green fluorescent proteins in cells. *Journal of Structural Biology 147*, 1 (July 2004), 62–9.

[105] Strassert, C. a., Chien, C.-H., Galvez Lopez, M. D., Kourkoulos, D., Hertel, D., Meerholz, K., and De Cola, L. Switching on luminescence by the self-assembly of a platinum(II) complex into gelating nanofibers and electroluminescent films. *Angewandte Chemie (International ed. in English) 50*, 4 (Jan. 2011), 946–50.

[106] Szalay, L., Gáti, L., and Sárkány, B. On the fundamental polarization of the fluorescence of viscous solutions. *Acta Physica Academiae Scientiarum Hungaricae 14*, 2-3 (1962), 217–224.

[107] Tang, J., Akerboom, J., Vaziri, A., Looger, L. L., and Shank, C. V. Near-isotropic 3D optical nanoscopy with photon-

limited chromophores. *Proceedings of the National Academy of Sciences of the United States of America 107*, 22 (June 2010), 10068–73.

[108] Testa, I., Schönle, A., von Middendorff, C., Geisler, C., Medda, R., Wurm, C. a., Stiel, A. C., Jakobs, S., Bossi, M., Eggeling, C., Hell, S. W., and Egner, A. Nanoscale separation of molecular species based on their rotational mobility. *Optics Express 16*, 25 (Dec. 2008), 21093–104.

[109] Thompson, R. E., Larson, D. R., and Webb, W. W. Precise nanometer localization analysis for individual fluorescent probes. *Biophysical Journal 82*, 5 (May 2002), 2775–83.

[110] Turgeman, L., and Fixler, D. Short time behavior of fluorescence intensity fluctuations in single molecule polarization sensitive experiments. *Optics Express 20*, 8 (Apr. 2012), 9276–83.

[111] van de Linde, S., Löschberger, A., Klein, T., Heidbreder, M., Wolter, S., Heilemann, M., and Sauer, M. Direct stochastic optical reconstruction microscopy with standard fluorescent probes. *Nature Protocols 6*, 7 (June 2011), 991–1009.

[112] van de Linde, S., Wolter, S., Heilemann, M., and Sauer, M. The effect of photoswitching kinetics and labeling densities on super-resolution fluorescence imaging. *Journal of Biotechnology 149*, 4 (Sept. 2010), 260–6.

[113] Weber, G. Photoelectric method for the measurement of the polarization of the fluorescence of solutions. *JOSA 46*, 11 (1956), 962–970.

[114] Westphal, V., and Hell, S. Nanoscale Resolution in the Focal Plane of an Optical Microscope. *Physical Review Letters 94*, 14 (Apr. 2005), 1–4.

[115] Williams, J. Photochemistry and photophysics of coordination compounds: platinum. In *Photochemistry and Photophysics of Coordi-*

nation Compounds II, V. Balzani and C. Sebastiano, Eds., no. July. Springer Berlin Heidelberg, 2007, ch. 5, pp. 205–268.

[116] Wolter, S., and Sauer, M. Follow-up to paper by S. Wolter, M. Schüttpelz, M. Tscherepanow, S. van de Linde, M. Heilemann and M. Sauer, entitled Real-time computation of subdiffraction-resolution fluorescence images. *Journal of Microscopy 245*, 1 (Jan. 2012), 109.

[117] Wolter, S., Schüttpelz, M., Tscherepanow, M., van de Linde, S., Heilemann, M., and Sauer, M. Real-time computation of subdiffraction-resolution fluorescence images. *Journal of Microscopy 237*, 1 (Jan. 2010), 12–22.

[118] Xia, T., Li, N., and Fang, X. Single-molecule fluorescence imaging in living cells. *Annual Review of Physical Chemistry 64* (Jan. 2013), 459–80.

[119] Xiao, J. Single-Molecule Imaging in Live Cells. In *Handbook of Single-Molecule Biophysics*, P. Hinterdorfer and A. Oijen, Eds. Springer US, New York, NY, 2009, pp. 43–93.

[120] Yeow, E. K. L., and Clayton, A. H. a. Enumeration of oligomerization states of membrane proteins in living cells by homo-FRET spectroscopy and microscopy: theory and application. *Biophysical Journal 92*, 9 (May 2007), 3098–104.

[121] Zhang, B., Zerubia, J., and Olivo-Marin, J. Gaussian approximations of fluorescence microscope point-spread function models. *Applied Optics 46*, 10 (2007), 1819–1829.

Acknowledgments

First of all, I would like to thank Dr. Peter Verveer for supervising my work and giving me the chance and the freedom to develop my own ideas and being always open to helpful conversations.

I would like to thank Prof. Dr. Philippe Bastiaens for the opportunity and support to work in his laboratory. I thank Prof. Dr. Roland Winter for being the second reviewer of this thesis.

For fruitfull discussions on the concept and supervision of this thesis, I would like to thank Prof. Dr. Vinod Subramaniam. Prof. Dr. Hernán Grecco I would like to thank for his constant support with this work.

I was lucky to work in the single molecule group with Franziska Tesche, Thomas Klein and Dr. Yvonne Radon. I especially want to thank Justine Mondry and Jenny Ibach not only for preparing the samples for the PALM measurements (Justine) and for the ensemble measurements (Jenny), but also for the continuous support during the past years and for helping me to carry on.

I would also like to thank Abram Calderon for preparing the Neuro2a-cells for PALM measurements and Dr. Leif Dehmelt for his support with the actin experiments. For providing the Pt-complex I thank Dr. Christian Strassert.

Although not mentioned in this work, I would like to say thank you to Prof. Dr. Mike Heileman, Dr. Ulrike Endesfelder and Sebastian Malkusch for help with the dual-color PALM/dSTORM measurements.

For helpful discussions about my work, I thank Robert Molenaar.

For constant help with keeping the lab/microscope/lasers (and in particular the water cooling!) running I would like to thank Dr. Sven Müller and

Dr. Michael Schulz. For help with the paperwork and registration at the TU Dortmund I thank Tanja Forck and Dr. Astrid Krämer.

Of course “the physicists” have to be mentioned here: Dr. Klaus Schuermann, Dr. Martín Masip and Dr. Aneta Koseska for the probably most silent, yet entertaining coffee breaks I had so far. I thank Björn Papke for help with the Ras-experiments and not playing too many pranks on me ;) and Amit Mhamane who I promised to mention in the acknowledgments.

For working together, having lunch together, playing football and foosball, talking science, or just having a laugh together I would like to thank all the present and past members of Dept. II.

I would like to thank my family, my parents and my sister, for constant support during the past five years.